The Dissertation Committee for Konstantinos Victor Belivanis Certifies that this is the approved version of the following dissertation:

Expanding the Use of Elastomeric Bearings for Higher Demand Applications

Committee:

Todd A. Helwig, Supervisor

Michael D. Engelhardt, Co-Supervisor

John Tassoulas

Eric B. Williamson

Stelios K. Kyriakides

Expanding the Use of Elastomeric Bearings for Higher Demand Applications

by

Konstantinos Victor Belivanis

Dissertation

Presented to the Faculty of the Graduate School of

The University of Texas at Austin

in Partial Fulfillment

of the Requirements

for the Degree of

Doctor of Philosophy

The University of Texas at Austin

August, 2017

Dedication

To my family…

«Ο σωστός δρόμος είναι ο ανήφορος»

Νίκος Καζαντζάκης

(The right way is the uphill)

Nikos Kazantzakis

Acknowledgements

“Of all possessions, a friend is the most precious.”

Herodotus

You were many helping me go through this endeavor. I was lucky enough to thank you personally.

Expanding the Use of Elastomeric Bearings for Higher Demand Applications

Konstantinos Victor Belivanis, PhD

The University of Texas at Austin, 2017

Supervisor: Todd A. Helwig

Co-Supervisor: Michael D. Engelhardt

Elastomeric bearings have been widely used in short-span bridge systems as they provide a reliable and cost-effective means of accommodating translations compared to the pot bearing alternatives. However, in higher demand applications pot and disk bearings are commonly used to accommodate significant forces and rotations and complex bridge movements from both thermal loads and daily truck traffic. Although elastomeric bearings have been designed for and utilized in twin steel trapezoidal box girder systems in Texas, classifying as higher demand applications, the lack of experimental and numerical research on such bearings, as well as some occasions of poor performance, dictate the need of further investigating their design requirements and performance.

The research presented in this dissertation is part of a broader research project including material-level studies, field monitoring of bridge bearings, large-scale experimental testing, and finite element simulations. This dissertation focuses on the large-scale experimental testing and investigates the effect of several parameters on the compression and shear stiffness of elastomeric bearings.

Specifically, bearing tests demonstrated the poor prediction ability current AASHTO axial stiffness prediction equations as well as a shear stiffness dependence on

the level of axial load and, in some cases, on the shearing direction of the bearing. However, it was shown that both AASHTO Method A and B produce safe elastomeric bearing designs. The finite element studies demonstrated that shim misalignment and cover friction can cause a reduction in the axial stiffness of an elastomeric bearing. In addition, an extensive finite element parametric study was performed to show variations in elastomeric bearings shear stiffness with different axial loads and shearing directions with a wide range of aspect ratios and height to width ratios.

Table of Contents

List of Tables

List of Figures

CHAPTER 1: INTRODUCTION

1.1 Problem Identification

Bridges are key components of any transportation network to provide passage over manmade and natural obstacles. While a variety of structural systems are utilized for bridges, the most common bridge-type are girder bridges in which flexural action is relied upon to resist the applied loads. The structural system of bridges is often divided into the substructure and the superstructure. The substructure generally consists of the piers, abutments and other foundation elements, while the superstructure of girder bridges primarily consists of the steel or concrete girders, the concrete deck, and the bridge rail. Bridge bearings provide the critical link between the superstructure and substructure elements. The bearings must be able to transfer the forces from the applied loading between the superstructure and substructure elements, while also accommodating the necessary rotational and translational deformations that occur at the bridge supports due to gravitational, lateral, and environmental loads. The force and deformational demand on the bearing is highly dependent on the geometry of the bridge including span lengths, girder continuity, presence and degree of horizontal curvature, and a number of other factors.

The selection of the bearing type used in each application was always a function of the loads and movements to be accommodated. There is a wide array of bearing-types that are available depending on the demand. Translational demands on the bearings can be accommodated using either a sliding bearing or by shearing of the bearing material. A

typical sliding bearing is the pot bearing that is shown in Figure 1.1a in which a Teflon surface is provided to minimize friction between the top of the bearing and bottom of the bearing. In the elastomeric bearing shown in Figure 1.1b, the translational deformations are accommodated through shearing in the elastomer. A section of the bearing in Figure 1.1b was cut away to show the steel shims that are typically included in the elastomeric bearings to help stiffen the bearing as well as fully engaging the elastomer. While elastomeric bearings are often more economical compared to pot bearings, most high-demand applications with large reactions and significant translational and rotational demands make use of pot bearings. However, past studies (Chen 2008) have shown that pot bearings in many cases do not perform as anticipated, defeating the purpose for which they have been chosen. In addition, the steel parts and frictional surfaces may degrade overtime leading to necessary regular inspections and/or replacements.

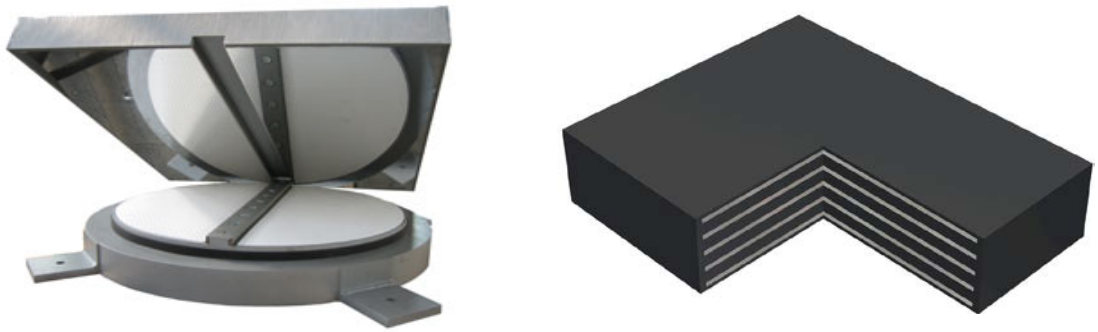

(a) (b)

Figure 1.1: Common types of bearings: (a) Pot bearing, (b) Steel laminated elastomeric bearing

Steel laminated elastomeric bearings are the most commonly used bearing for concrete girder systems. In most situations, the concrete girder bridges make use of simple spans with span lengths less than 150 ft. Elastomeric bearings have been successfully used in some higher-demand applications where the pot bearing alternative would have normally been used. The bearings have performed well, however, in isolated cases, some of the bearings have shown significant distress. A research study sponsored by the Texas Department of Transportation (TxDOT) was undertaken to investigate the use of steel laminated elastomeric bearings in higher demand applications. The study included field monitoring, elastomeric material tests, full-scale laboratory testing, and parametric finite element analysis. This dissertation primarily focuses on the full-scale experimental tests. The work from the material tests was presented in Sun (2015) while Han (2016) discussed the field monitoring and parametric finite element studies. The following section provides an overview of the scope of the work followed by an outline of the chapters of the dissertation.

1.2 Scope of work

This dissertation highlights the results of TxDOT Research Project 0-6785, which is focused on extending the use of elastomeric bearings to higher demand applications. The primary focus of this dissertation is the full-scale testing program. Although elastomeric bearings are commonly used in concrete bridge applications, the bearings that were tested as part of this research are much larger. Figure 1.2 shows a comparison of the size of conventional bearings (the smaller bearing) versus one of the bearings that was tested as

part of this research study. The much larger sizes of the bearings that are necessary in higher demand applications raise a number of questions on the variability of the material properties as a result of the vulcanization process and the manufacturing practices with the larger bearing. Sun (2015) provided an overview of the material testing program that was used to study variations in the elastomer both across the width and through the thickness of the bearings. The impact of temperature on the shear properties was also considered. The tests that Sun carried out consisted of shearing tests on the elastomer. Although these tests provide a good indication of the variations of the shear properties across the bearing, the actual demand on the bearings in service come from the girder support reactions that include girder translations and rotations. The resulting demands on the bearing therefore have shearing deformations, axial compression, and girder rotations that also impose gradients in the compression across the width and length of the bearing. In order to a carry out detailed parametric studies to investigate the behavior of the bearings, to compliment the material-based tests from Sun (2015), full scale testing was carried out and is the focus of this dissertation.

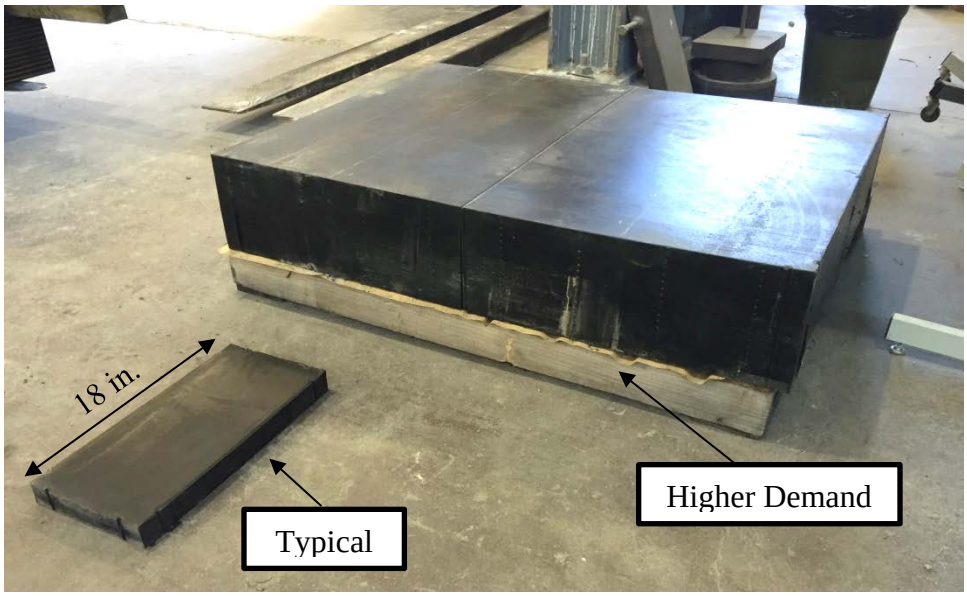

Figure 1.2: A typical elastomeric bearing and one used for higher demand application

To consider the force and deformational demands on the full-scale bearings, a test setup was developed that could investigate, 1) axial compression, 2) axial compression plus shear, and 3) axial compression, shear, and a compression gradient due to girder rotation. The results from the full-scale tests provided results that were necessary to validate the finite element model used by Han (2015) in studying the behavior of elastomeric bearings in higher demand applications. The model was then used to carry out a detailed parametric study on bearings so that a comprehensive design methodology for bearings in higher demand applications could be developed. The following section provides an overview of the chapters in this dissertation.

1.3 Organization of work

This dissertation consists of seven chapters. Following this introductory chapter, the other six chapters consist of the following:

1. Chapter 2 provides an extensive literature review on steel laminated elastomeric bearings. After the basic properties are introduced, mechanics and proposed theories for predicting the deformations are outlined. Factors that need to be taken into consideration when simulating elastomeric bearings with finite element models are also discussed. Gaps in the literature concerning full-scale testing, directional shear, temperature-dependent material coefficients for finite element studies, and the effect of imperfections are identified.
2. Chapter 3 discusses the test setup that was fabricated and assembled to carry out full-scale testing on the bearings. An overview of the methodology that was followed in each stage of the testing is provided.
3. Chapter 4 outlines the finite element modeling for the simulations conducted as part of this dissertation. Key assumptions that were imposed in the studies are discussed.
4. Chapter 5 provides a presentation of the experimental results and discusses major findings contributing to the literature.

5. Chapter 6 provides a summary of the analyses performed along with major findings concerning imperfections and directional effects of shear, backed by experimental results.
6. Chapter 7 provides a summary of the results and an overview of key conclusions from the research presented in this dissertation. A discussion of future work is also provided.

CHAPTER 2: BACKGROUND AND LITERATURE REVIEW

2.1 Introduction

This chapter provides a summary of literature relevant to steel-laminated elastomeric bearings. First, an overview of the types of bearings is presented and advantages and shortcomings of different types of bearings are discussed. Next, basic characteristics and material properties, important for the design of a steel-laminated elastomeric bearing, are introduced, along with their impact on the bearing design. Subsequently, failure modes at which a bearing design is deemed unsuccessful are presented. During this subsection, gaps in literature are identified, providing the motivation for the current research. A historical evolution of codes and standards concerning steel-laminated elastomeric bearings is then presented along with the relevant literature. Then, an overview of methods useful for the finite element modeling of such bearings is presented, and important parameters are identified. Finally, an overview of knowledge gaps identified throughout the literature review process is presented, and a brief description of how this dissertation attempts to fill some of those gaps is provided.

2.2 General description

Elastomeric bearings have been widely used in both prestressed concrete and steel bridge girder systems. However most of the systems that use elastomeric bearings have relatively short spans and small total lengths. Bridges with larger spans and longer total bridge lengths often are subjected to bearing reactions, thermal movements, and rotations that are outside of the range for which elastomeric bearings have traditionally been used. However, for economical and practical reasons there is a strong motivation to extend the use of the bearings to *higher demand applications* besides those for which they have traditionally been utilized. To extend the use of bearings to these *higher demand applications*, a clear understanding of the basic behavior of the bearings is necessary. In addition, knowledge of the typical testing methods for the bearings is very important for the development of laboratory testing plans and evaluation of design limitations. This chapter provides a summary of the fundamental behavior of elastomeric bearings, an overview of previously completed research and the evolution of design guidelines, as well as a summary of important factors to consider for the finite element studies on elastomeric bearings.

2.2.1 PURPOSE OF BEARINGS

Elastomeric bearings have been widely adopted in the bridge industry because the bearings are able to efficiently and economically achieve the vertical, rotational, and longitudinal support conditions that are idealized as the roller or pin supports that are assumed in basic structural analysis. In addition, the bearings do not have many of the

problems that traditional roller and rocker bearings have with corrosion, freezing, and fatigue. Another advantage of elastomeric bearings compared to traditional bearings is the ability to accommodate small fabrication errors either in the superstructure or the substructure (Roeder and Stanton 1983) without inducing significant forces into the system.

2.2.2 TYPES OF BEARINGS

Rubber is practically an incompressible material with a Poisson's Ratio, ν, of approximately 0.5. Although rubber has a relatively low modulus of elasticity (E≈300 psi), there is very little change in volume under applied loads. As a result, when rubber is loaded in compression, it bulges in order to maintain its volume. Although the generic term "rubber" is frequently associated with bearings, most modern bearings are made from an elastomer which is a polymer comprised of either natural or synthetic rubber. One of the most commonly used synthetic rubbers is neoprene, which exhibits many of the same properties as natural rubber but can offer better performance in many applications. Although the behavior of an elastomeric bearing depends highly on the material properties of the rubber used for its fabrication, most elastomeric bearings for structural applications are reinforced with steel plates to improve the behavior of the bearings. The performance of a bearing can be significantly affected by the type, amount, and layout of the reinforcement. The purpose of the reinforcement is to provide significant in-plane stiffness while also restraining the effects of bulging. For example, the mitigating effect of steel shims is shown in Figure 2.1**.**

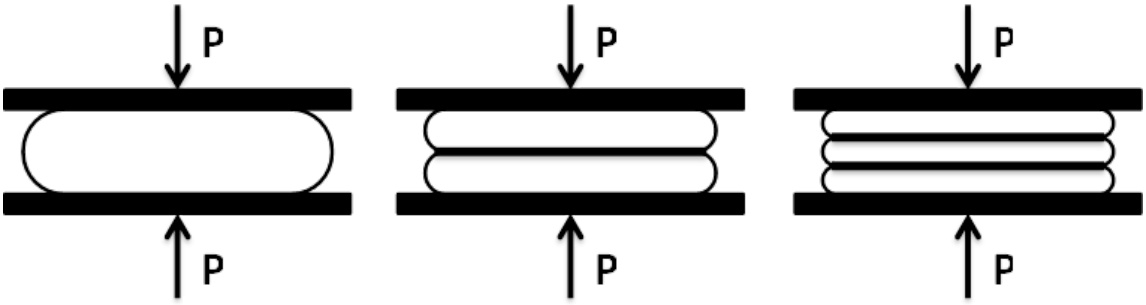

Figure 2.1: Bulging effect for different reinforcement layouts for the same axial load P

2.2.3 UNREINFORCED ELASTOMERIC BEARINGS

Unreinforced elastomeric bearings do not have internal reinforcement. As depicted in Figure 2.1a, a single large bulge is created when the bearing is subjected to axial compression. The only restraint in this case is provided by the loading surface and is dependent on the coefficient of friction between the rubber and the loading surface, which can be highly variable. If adequate shear restraint does not exist between the bearing and loading surface, slippage (Bakirzis and Lindley 1970) occurs, which affects the shear demands on the bearing. In addition, without proper restraint, slipping between the bearing and loading surface can lead to the bearing "walking" from cyclic loading, in which case the bearing translates relative to the girder or foundation element. Walking of the bearing can lead to localized overstress in the bearing itself or damage to the girder due to a lack of support.

2.2.4 FIBER REINFORCED ELASTOMERIC BEARINGS

One type of reinforcement used in elastomeric bearing applications is fibers of woven cotton or fiberglass. The end product is a macroscopically homogenous series of elastomer and fiber layers that can be molded into large pieces and cut according to the dimensions determined by the designer. The bearing is laterally stiff and may require the use of Polytetrafluoroethylene (PTFE - Teflon) sliders to accommodate the horizontal displacement demands. The force needed to overcome the static friction increases as the vertical reaction in the bearing increases and pier flexure can become the primary mechanism of accommodating horizontal movement (Chen 2008). The role of pier flexure in cases with sliding bearings can be understood by considering the frictional forces that must be overcome for sliding to take place between the beam and the bearing. The coefficient of friction of PTFE is approximately 5%. Therefore, if a bridge has a million-pound reaction, a friction force of approximately 50,000 lbs. must be overcome for sliding to take place. For typical length bridge piers, a 50,000-lb. shear force can lead to relatively large deformations that may accommodate much of the necessary thermal movement. The pier design may need to include consideration of the effects of this movement. For guided disk or pot bearings, the force necessary to slide can be further magnified by misaligned guides. Chen (2008) showed that because of frictional forces necessary to slide, the bridge often does not thermally “breath” about the fixed pier, which is often the focal point of the lateral guides in horizontally curved bridges. As a result, the guides are often misaligned and much larger forces can develop before sliding occurs.

2.2.5 STEEL LAMINATED ELASTOMERIC BEARINGS

The shear deformational characteristics of rubber limit its load carry capacity as the thickness of the elastomer increases. As depicted in Figure 2.1, steel laminates are typically used to control bulging in the elastomer. The steel laminates produce independent layers of elastomer, which therefore results in shearing of the individual layers relative to each other through the depth of the bearing. The end product is a series of alternating layers of steel and elastomer that results in a vertically stiff and horizontally flexible bearing, which accommodates the bridge movements without inducing significant horizontal loads to the substructure. An elastomer cover is included on the outside of the steel plates to ensure protection from the environment.

2.2.6 ADVANTAGES OF STEEL LAMINATED ELASTOMERIC BEARINGS

Steel laminated elastomeric bearings have many potential advantages compared to other types of bearings, including the following:

- Steel laminated elastomeric bearings can provide flexibility in the longitudinal and lateral direction of the bridge girders while still maintaining the necessary stiffness in the vertical direction to safely support the large girder reactions.
- The horizontal stiffness remains relatively constant over the design life as opposed to PTFE surfaces, where debris or other corrosive action on the sliding surfaces can increase the frictional resistance over time.
- Steel laminated elastomeric bearings allow for short-term over-rotations with relatively low probability of damage (Roeder and Stanton 1996).

- Steel laminated elastomeric bearings are an economically efficient alternative for accommodating bridge movements due to temperature and vehicular use both from an initial installation perspective and from a maintenance perspective.

There are many advantages of using elastomeric bearings and which make potentially extending the use of the bearings to *higher demand applications* particularly attractive.

2.2.7 SHORTCOMINGS OF STEEL LAMINATED ELASTOMERIC BEARINGS

Although the previous section discussed the advantages of elastomeric bearings, there are also potential shortcomings to using steel laminated elastomeric bearing design:

- Steel laminated elastomeric bearings may be limited to supporting lower vertical loads than their design alternatives.
- The rotational limits of steel laminated elastomeric bearings are lower than the rotational capacities of many other types of bearings.

2.3 Geometry characteristics and material properties

The geometry attributes and engineering properties of the materials used in elastomeric bridge bearings must be established before the engineer of record can design a bearing. The applicable material properties and geometry characteristics are discussed in this section, along with their impact on the bearing performance. In the following subsections, the key criteria are presented along with a discussion of their impact on the behavior of a bearing.

2.3.1 SHAPE FACTOR

The shape factor of one elastomer layer of a laminated bearing is defined as the ratio of the loaded area to the area free to bulge, thus indicating the confinement level of the elastomer. Generally, a higher shape factor leads to axially stiffer bearings. A denser reinforcement layout leads to an increased shape factor. Although the translational stiffness of the bearing is essentially unaffected, the use of large shape factors leads to bearings with higher axial and rotational stiffness due to the bulging restraint. If the bearing does not have a uniform reinforcement layout, the shape factor of the bearing is defined as the largest shape factor of the individual layers. For a bearing with a uniform reinforcement layout the shape factor is defined in

$$S = \frac{L \cdot W}{2 \cdot t \cdot (L + W)} \qquad \text{Eq. 1}$$

where:

L = the length of the bearing parallel to the span of the bridge,

W = the width of the bearing perpendicular to the span of the bridge, and

t = the thickness of an individual elastomer layer of the bearing.

2.3.1.1 Vertical stiffness of steel laminated elastomeric bearings

As mentioned previously, the vertical stiffness is directly related to the shape factor. The vertical stiffness of an elastomeric bearing is an important property of the bearing considering both for pure compression from the girder reaction as well as for accommodating the necessary girder rotation. The vertical stiffness becomes particularly important for *higher demand applications* such as steel tub girder systems where the axial and rotational behavior can be a concern. The axial stiffness of the bearing is important in calculating the relative deflection across an expansion joint, as expansion joints are sensitive to relative deflections (Roeder, Stanton et al. 1989). The axial stiffness is also important in cases of rocking motions (i.e. tall structures with base isolation). The rotational stiffness, usually associated with the lift-off phenomenon is directly related to the axial stiffness. Lift-off is defined as the phenomenon where separation occurs between the girder and the top of the bearing under rotation, decreasing the area over which the compression is resisted.

The behavior of a steel-laminated bearing in compression can be simulated as the behavior of stacked bonded rubber blocks, assuming that the steel laminates are axially rigid relative to the rubber. Early work (Gent and Lindley 1959) was conducted assuming linear elastic behavior for rubber and accounting for incompressibility, resulting in the proposed apparent Young's modulus, E_a', for the bonded rubber block given by:

$$\frac{1}{E'_a} = \frac{1}{E_a} + \frac{1}{E_b} \qquad \text{Eq. 2}$$

where E'_a is the apparent Young's modulus of the equivalent bonded incompressible rubber block, E_b is the modulus of bulk compression, and E_a is given by:

$$E_a = \frac{4}{3} E(1 + S^2) \qquad \text{Eq. 3}$$

where E is the Young's modulus of the rubber, often replaced (Muhr and Thomas 1989) by $3G$, where G is the shear modulus of the rubber, and S is the shape factor, equal to the ratio of the loaded area over the area that is free to bulge. The above equations were developed for infinitely long strips of bonded rubber and have reasonable agreement with experimental data for low levels of stress, and low values of shape factors.

Subsequent research (Gent and Meinecke 1970) developed analytical expressions for rubber blocks of any cross-section. Specifically, for rectangular sections the published solution for E_a is given by:

$$E_a = 3G\left[\frac{4}{3} - \frac{2\,(l\,w + 4\,t^2)}{3\,(l^2 + 8\,t^2 + w^2)} + \frac{1}{3}\left(\frac{w^2}{l^2}\right)\left(1 - \frac{192w}{\pi^5 l}\sum_{n=1,3,5\ldots}^{\infty}\frac{1}{n^5}\tanh\left(\frac{n\pi l}{2w}\right)\right)\right] \qquad \text{Eq. 4}$$

where l is the length of the block, w is the width of the rubber block, and t is the thickness of the rubber block. More recent research (Yeoh, Pinter et al. 2002) has developed an analogous expression relaxing the assumption of incompressibility in the elastomer. The corresponding value of E_a is given by:

$$E_a = 3G\left[\frac{4}{3} - \frac{2\,(l\,w + 4\,t^2)}{3\,(l^2 + 8\,t^2 + w^2)} + \frac{8}{t^2}\sum_{n=1,3,5\ldots}^{\infty}\frac{4wl}{n^2\pi^2\lambda_n^2} - \frac{8w}{n^2\pi^2\lambda_n^2}\tanh\left(\frac{\lambda_n l}{2}\right)\right] \quad \text{Eq. 5}$$

where

$$\lambda_n^2 = \frac{n^2\pi^2}{w^2} + \frac{12G}{t^2 E_b} \quad \text{Eq. 6}$$

The expressions presented above were developed for linear elastic material and are in good agreement for unfilled rubbers. However, filled rubber expresses nonlinearities in behavior at lower values of deformation and loads leading to a divergence of experimental results and predictions of the above equations. Filled rubber is rubber with added particles, such as carbon black, that modify the properties of the rubber, mitigate aging effects, and reduce the consumption of binder materials. Researchers (Muhr and Thomas 1989) have tried to reduce this divergence by providing a relationship that accounts for the material nonlinearities (strain-dependent shear modulus, $G_{\bar{\gamma}}$) based on the average shear strain in the layer, $\bar{\gamma}$, weighted for energy density. The proposed expression for the apparent compression modulus, $E_{c(ec)}$, is

$$E_{c(e_c)} = 3G_{\bar{\gamma}}(1 + 2S^2) \quad \text{Eq. 7}$$

where

$$\bar{\gamma} = \sqrt{3(1 + 2S^2)} \cdot e_c \quad \text{Eq. 8}$$

AASHTO (AASHTO 2012) specifies the compressive strain of each layer, e_c, as

$$e_c = \frac{\sigma_c}{4.8 \cdot G \cdot S^2} \qquad \text{Eq. 9}$$

The above expression was adopted from previous research (Stanton, Roeder et al. 2008), acknowledging the fact that this simplified expression is prone to inaccuracies. Lately, Van Engelen and Kelly (2014) proposed an approximation for the apparent compression modulus of square pads, corrected for the influence of rubber bulk compressibility. The proposed expression is:

$$E_a = \left(\frac{1}{6.748GS^2} + \frac{1.38}{E_b}\right)^{-1} \qquad \text{Eq. 10}$$

More recent research of bonded cylindrical discs (Anderson, Mott et al. 2004, Qiao and Lu 2014) proves the high sensitivity of the vertical stiffness on Poisson's ratio (ν) for values of ν close to 0.5 and large shape factors (larger than 10). This fact combined with the fact that for neoprene rubber (elastomer under consideration in this study) the values of ν can range from 0.499 to 0.4999 (Holownia 1980) justifies the difficulty of finding an expression valid for the calculation of vertical stiffness of an elastomeric bearing. The complexity is further aggravated when accounting for the significant sensitivity of the measurement of ν at low volumetric strains considering difficulties of fitting the testing sample fitting into the testing device (Peng, Shimbori et al. 1994).

All the above expressions are developed based upon the assumption of perfectly parallel rigid layers. Another expression, developed based on the fitting of experimental data (Podolny and Muller 1994) from finished bearings, predicts lower values of stiffness for higher shape factors. The proposed equation neglects the role of bulk compression, but

accounts for the plan aspect ratio. The proposed expression for the apparent compression modulus, E_a, is

$$E_a = \left(\frac{GS^2}{Ct^2}\right)E \qquad \text{Eq. 11}$$

where

$$C \approx \frac{0.47}{\frac{L}{W}} + \frac{0.9}{\frac{L}{W}} + 1 \qquad \text{Eq. 12}$$

2.3.2 STEEL REINFORCEMENT

As previously mentioned, the main role of the steel reinforcement is to provide axial stiffness to the bearing by restricting bulging. As a result, in-plane tensile stresses are developed in the steel layer when the bearing is in compression. Therefore, the steel reinforcement must be designed to sustain these tensile stresses. However, the plate thickness that is typically required for sustaining the vertical loads will usually be less than the practical thickness required for fabrication purposes.

2.3.3 EFFECTIVE ELASTOMER THICKNESS

A steel laminated elastomeric bearing consists of layers of steel and elastomer. As mentioned previously, the elastomer is the material that accommodates the horizontal thermal movements. A poorly detailed bearing may experience rollover as depicted in Figure 2.2b. From a code perspective (EN1337-3 2005, AASHTO 2012), the minimum effective elastomer thickness is limited to twice the value of the design shear deformation

to avoid rollover at the edges of the bearing. The code-targeted shear behavior of elastomeric bearings is depicted in Figure 2.2a.

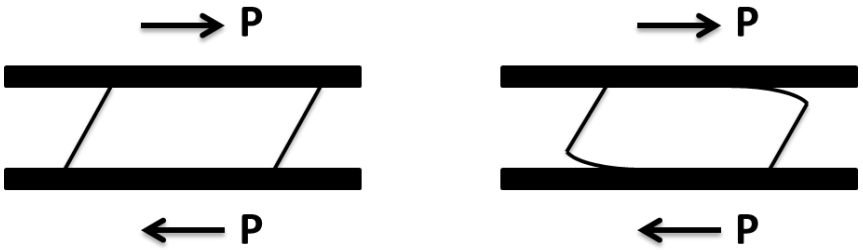

(a) (b)

Figure 2.2: Bearing (a) without and (b) with rollover at the edge

2.3.4 SHEAR MODULUS/HARDNESS

Steel laminated elastomeric bearings are advantageous because of their relatively small horizontal stiffness compared to their high axial stiffness. As a result, the bearings resist vertical deformation while allowing translational deformations in the horizontal direction through shearing of the elastomer. Therefore, the most important property taken into consideration when designing the bearing is the shear modulus of the elastomer.

The shear modulus of the elastomer at 73°F is typically used for design. Traditionally, the Shore A durometer hardness has been specified for characterizing the shear modulus. However, numerous studies (Stanton, Roeder et al. 2008, AASHTO 2012) have reported that the relationship between hardness and shear modulus can vary significantly. To account for this variability, AASHTO assigns a range of values for a given Shore A hardness value and directs the engineer to design for the least favorable

value for each design check. A higher durometer value generally indicates a stiffer elastomer.

2.3.4.1 Temperature dependence of shear modulus

The elastomer shear modulus value range, being the most important material property for the design of an elastomeric bearing, should be evaluated for the design life of the bearing. However, the elastomer shear modulus is heavily dependent on the temperature (Yura 2002). If not accounted for, the variation of the shear modulus with temperature (the material becomes stiffer at lower temperatures) can result in slip of the bearing as the frictional force between the bearing and the superstructure is overcome. Slipping in the opposite direction as the superstructure expands under increasing temperature, requires the friction to be overcome again. However, this is less likely to happen due to the softer material properties at higher temperatures. As a result, slip between the bridge bearings and the superstructure is more likely a one directional, low-temperature driven, cumulative phenomenon.

2.3.5 BULK MODULUS

The bulk modulus represents the resistance of a material to volumetric change when subjected to hydrostatic pressure loading. The bulk modulus is volumetric-strain dependent and as a result is important to be characterized for the volumetric strain range of interest. The bulk modulus is often measured by means of a confined pressure test (Peng, Shimbori et al. 1994). Although usually treated as incompressible, elastomers tend to be slightly compressible. The small amount of compressibility can significantly affect bearing properties of interest at high levels of confinement.

2.4 Failure modes

A bearing experiences various types of loads and deformations throughout the design life. This can lead to a number of modes in which the bearing can fail. The most common modes that should be considered in bearing design are described in the following subsections.

2.4.1 COMPRESSION

There are two possible failure modes of a steel laminated elastomeric bearing subjected to compression. The first mode consists of debonding of the elastomer at the edge of the reinforcement layer. This has effectively no impact on the capacity of the bearing. However, it can be an initiation point for delaminations to propagate at the reinforcement surface, reducing the effectiveness of the reinforcing and increasing the area that is free to bulge (Figure 2.3a). This failure mode is a result of poor manufacturing process or large cyclic axial loads (Stanton, Roeder et al. 2008). The second compression failure consists of the yielding and potentially fracturing the steel reinforcement as depicted in Figure 2.3b. This type of failure is less frequent as the failure load required can be up to 10 times the design value (Stanton, Roeder et al. 2008).

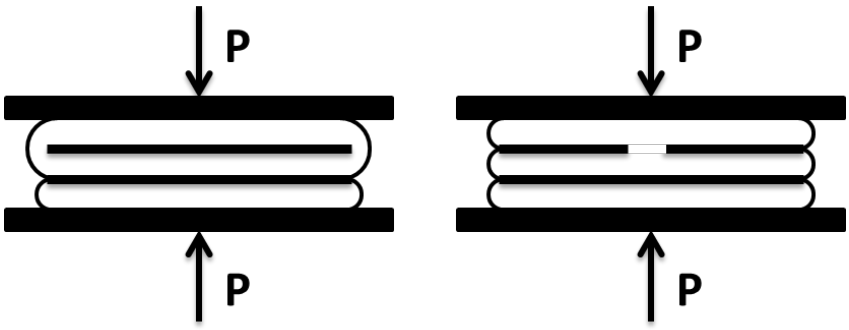

(a) (b)

Figure 2.3: Compression failure due to (a) tension debonding and (b) fractured steel plates

2.4.2 SHEAR

A steel laminated elastomeric bearing is expected to experience significant shear deformations during its design life, mainly due to thermal expansion and contraction of the superstructure. Other loadings that can result in significant horizontal movements of the superstructure are earthquake, wind, and even traffic loads.

2.4.2.1 Cyclic Shearing

Cyclic shear deformation of a bearing can cause the creation and propagation of cracks at the interface between the reinforcement layer and the elastomer (AASHTO 2012). Cracks are initiated at locations where tension debonding has occurred or the vulcanizing process was not completely successful. As the cracks propagate the tensile stresses at the steel shims are relieved, allowing adjacent layers of elastomer to bulge as one. This failure mode is illustrated in Figure 2.4.

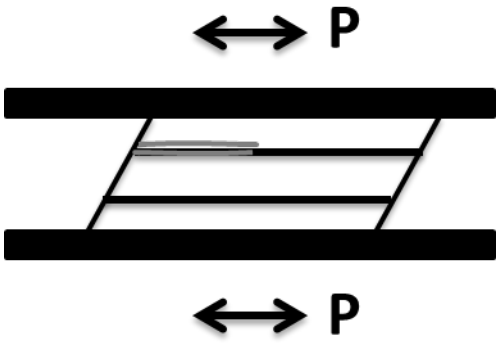

Figure 2.4: Delamination due to cyclic shear loading

2.4.2.2 Slipping

Knowledge of the bearing shear stiffness in each direction is important so that slipping is avoided. Slipping occurs when the force developed at the bearing-girder interface (or the bearing to substructure interface) due to the shearing of the bearing exceeds the static friction. The bearing shear stiffness ($K_{bearing}$) is dependent only on the plan area ($A=LB$), the total rubber thickness (H_{tot}), and the average rubber material shear modulus (G) and can be computed as:

$$K_{bearing} = \frac{G \cdot L \cdot B}{H_{tot}} \qquad \text{Eq. 13}$$

In *higher demand applications,* i.e. curved box girders, it has been observed that the shearing of the bearing due to temperature effects on the bridge superstructure does not happen consistently in one direction throughout the year. The shearing direction is dependent on the bridge curvature but also the direction of the solar radiation, enabling predominantly longitudinal or transverse movements. Initial research conducted

numerically (Nguyen and Tassoulas 2010) showed insignificant variability on the bearing shear stiffness for different shearing directions, although a reduction of the maximum shear strain was observed. However, the study was limited to low height to length ratios and no experimental data exists to validate or contradict these conclusions.

2.4.3 ROTATION

The rotational and axial demands on the bearing are often interrelated since both demands tend to increase when span lengths are increased. However, the design requirements for increased axial and rotational demands are often contradictory. To accommodate the high axial load, an axially stiff bearing is required. However, in order to prevent lift-off (Figure 2.5a) a flexible bearing is required. While lift-off of the bearing on its own does not constitute a failure, the ramifications of lift-off can affect the axial performance since the vertical reaction must be resisted by a smaller area of the bearing, and thus, local compressive failure can initiate as a result of lift-off.

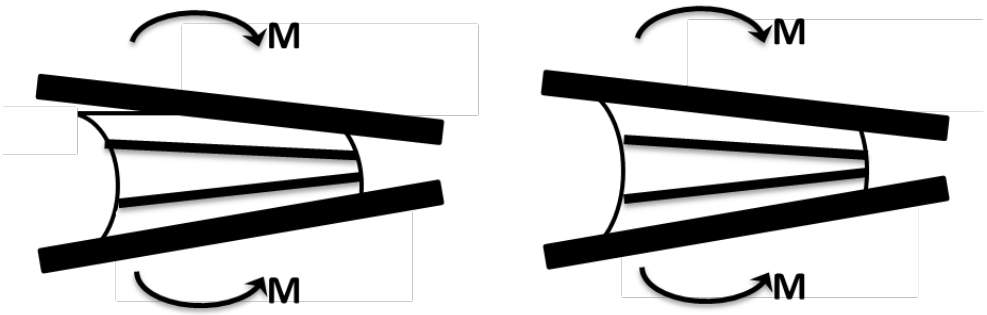

(a) (b)

Figure 2.5: Bearing deformation for applied moment (a) with and (b) without lift-off

Past AASHTO provisions did not allow lift-off, and, as a result, the structural engineer had to find the balance between accommodating both the axial load and the rotational demands. Based upon research conducted by Stanton et al. (Stanton, Roeder et al. 2008) that showed that the effect of lift-off, if accounted in the design, does not cause detrimental effects to the bearing, partial lift-off is allowed in the current version of AASHTO (AASHTO 2012).

2.4.4 STABILITY

The shear modulus of an elastomeric bearing decreases with increasing axial load (Gent 1964, Stanton, Scroggins et al. 1990, Weisman and Warn 2012). The degradation in the stiffness makes instability in the bearing a potential concern. The buckling capacity decreases as the shear strains are increased, however, the thickness of the rubber layer is believed to have a greater influence than the shape factor in this effect (Buckle, Nagarajaiah et al. 2002). Tests associated with previous research were conducted at lower axial stress levels and shape factors up to approximately 15 were investigated. In addition, the bearing pads that were tested were significantly smaller than pads that would fit the characterization for *higher demand applications*. Because of stability concerns AASHTO does not allow exceeding half the buckling stresses.

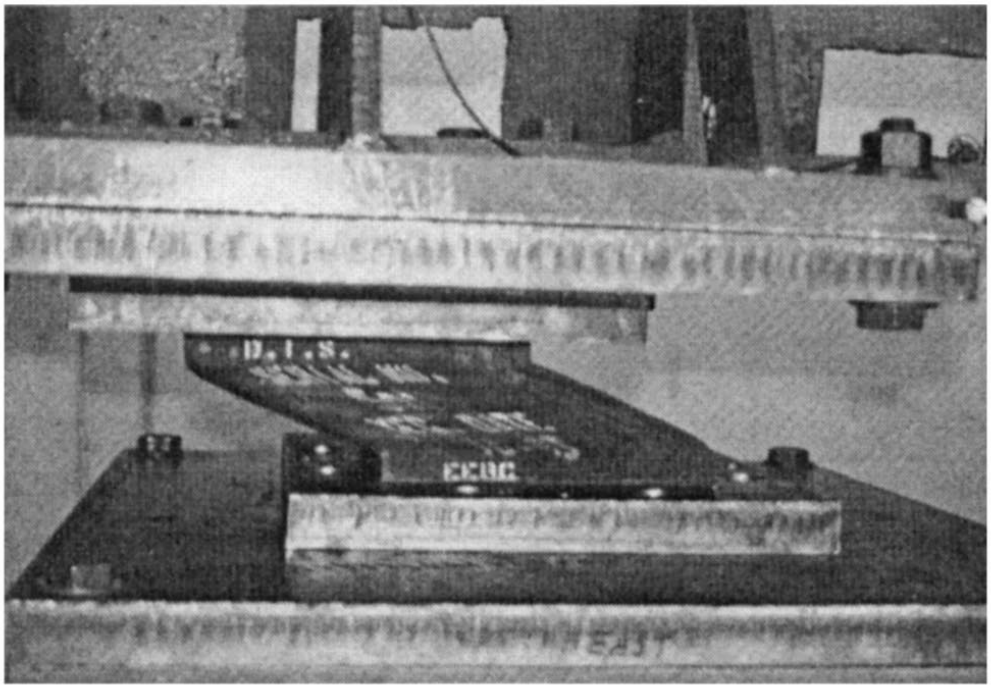

Figure 2.6: Bearing in buckled configuration (Buckle, Nagarajaiah et al. 2002)

2.4.5 SLIPPAGE

Another common failure mode is the slippage (walking out) of the bearing when it is not attached via a sole plate to the superstructure or via mechanical devices to the pier (McDonald, Heymsfield et al. 2000, Nims and Parvin 2000, Heymsfield, McDonald et al. 2001). In some cases, stability limits conflict with the limits imposed to prevent slippage. In such a case, occasional bearing slippage is preferred as no detrimental consequences have been reported as long as the slippage occurs between the bearing and the beam and not the bearing-pier interface (Bradberry, Cotham et al. 2005). However, in such a case, the sole plate must be designed to account for the relative displacement of the bearing.

2.5 Historical development of code provisions

This portion of the literature review focuses on the historical development of design procedures for steel laminated elastomeric bearings. Although research on bearings has been conducted all over the world, design provisions in AASHTO (AASHTO 2012) are mainly a result of research funded by the National Cooperative Highway Research Program (NCHRP). Pertinent NCHRP studies are summarized below.

2.5.1 PERFORMANCE OF ELASTOMERIC BEARINGS - NCHRP 298

NCHRP 298 (Roeder, Stanton et al. 1987) presented the results on the investigation of the behavior of steel laminated elastomeric bearings under room and low temperatures. The study also focused on the behavior under compression, shear, rotations, and combined loading, as well as investigating the limits for stability and fatigue.

The effect of low temperature on the shear modulus of the elastomer was found to be noticeable and significant below 32 degrees Fahrenheit. In addition to the instantaneous stiffening of the elastomer, the shear modulus was found to continue to increase when the elastomer was exposed for longer periods to temperatures below 32 degrees Fahrenheit. This effect is called crystallization and was further investigated in subsequent research studies (Roeder, Stanton et al. 1989).

The investigation on the compressive and rotational behavior led to limits in the compressive stress of 1600 psi and the no-lift-off provision for the girder rotation. Furthermore, during this study, the 50% shear strain limit due to the shearing of the bearing (provision still exists today) was imposed as a result of observations of rollover during the

tests. Rollover was believed to create a potential tearing failure in the elastomer, which would likely increase under repeated loading.

The reduction of the bearing shear stiffness with increasing load was also reported in this study, with no limit established or mathematical model presented. However, the difficulties in calculating the axial stiffness of a multi-layer steel laminated elastomeric bearing were identified.

2.5.2 LOW TEMPERATURE BEHAVIOR AND ACCEPTANCE CRITERIA FOR ELASTOMERIC BRIDGE BEARINGS - NCHRP 325

During this study (Roeder, Stanton et al. 1989) the behavior of natural rubber and neoprene steel laminated elastomeric bearings was investigated. The major outcome was that, although both materials experienced an increase in shear modulus at low temperatures, the effect was more prominent for neoprene bearings for the same room temperature shear modulus. Moreover, the crystallization effect was extensively studied leading to a limit of the ratio of the shear modulus at cold temperature to the shear modulus at room temperature to a value less than four for both natural rubber and neoprene compounds. The phenomenon of relaxation was also investigated during this research study, however subsequent research (English, Klingner et al. 1994) showed that relaxation tests do not represent realistic bridge behavior. Finally, acceptable fabrication tolerances were reduced.

2.5.3 ELASTOMERIC BRIDGE BEARINGS: RECOMMENDED TEST METHODS - NCHRP 449

NCHRP 449 (Yura, Kumar et al. 2001) investigated the test methods that should be used for evaluating steel laminated elastomeric bearings, proposed test methods to be used for material acceptance, and limiting criteria. The researchers proposed the elimination of the following previously required tests: Shore A Hardness, shear resistance, ozone resistance, and compression set. Also, aging tests were determined to be irrelevant for bearing sizes and shape factors utilized in civil engineering applications.

In addition to the elimination of certain tests for steel laminated elastomeric bearings, NCHRP 449 proposed an inclined shear test as a method to measure the shear stiffness of the bearings. The test involved inclined plates inducing shear in a bearing under compression. The inclined compression test provides a unique pair of axial load vs. shear strain values. Due to the fact that in the current study the effect of axial load on the shear stiffness for bearings that generally would be classified as higher demand applications needed to be investigated, this test method was not considered.

The detrimental effect of misalignment of steel laminates on the performance of elastomeric bearings was also investigated. The conclusions were that the horizontal misalignment of the laminates has less impact on the performance of the bearing than does variations in the rubber layer thickness or rotational misalignments. Lastly, the need for a better understanding of the temperature dependent interaction between the bridge superstructure and the elastomeric bearing was indicated, especially for the case of low-temperature stiffening including crystallization.

2.5.4 ROTATION LIMITS FOR ELASTOMERIC BEARINGS - NCHRP 596

NCHRP 596 (Stanton, Roeder et al. 2008) focused on the rotational response of steel laminated elastomeric bearings. The study included static and cyclic tests for the evaluation of stiffness and failure limit states. It also involved finite element simulations.

Experimental results confirmed the existence of reserve axial load capacity even after debonding of the elastomer from the steel laminates. This led to the conclusion that there is no unique definition of failure. However, it was observed that this debonding phenomenon can expedite the propagation of delamination due to cyclic shearing. Experiments also proved the ability of steel-laminated bearings to carry axial loads up to 10 times greater than their design values and addressed a need for improvement of the manufacturing quality.

The finite element portion of the study indicated that stiffer compounds performed better for comparable loads. This improvement was markedly evident for bearings with higher shape factors. Furthermore, the difficulties for matching compressive stiffness were further confirmed and the need of investigating the effect of the aspect ratio on the axial and rotational performance of a bearing was indicated. Lastly, a proposal was made to relax the no-lift-off provision.

2.5.5 CURRENT DESIGN APPROACHES

Although some U.S. states, including Texas, follow their own design approaches and methodologies, all methodologies are generally based on AASHTO (AASHTO 2012) provisions for elastomeric bearings. The current AASHTO provisions allow the designer

to choose between two methods, “Method A” and “Method B”, for proportioning the bearing. These two methods are described in the following subsections.

2.5.5.1 Method A

Relative to Method B, Method A produces inherently more conservative designs as a result of the stress limits associated with it. The implicit rotational and stability limits are met as a result of the geometrical constraints imposed by this method. Specifically, the Method A provisions are presented in Table 2.1.

Table 2.1: AASHTO Limits for Method A

Geometric limit	Compressive stress limit	Rotation limit	Shear deformation limit	Stability limit
$\frac{S_i^2}{n} < 22$	$\sigma_s < 1.25GS_i$ & $\sigma_s < 1.25\ ksi$	Implicitly accounted for	$\Delta_s < \frac{h_{rt}}{2}$	$h_{rt} < \frac{L}{3}, \frac{W}{3}, \& \frac{D}{4}$

In the table above, σ_s is the average compressive stress from applicable service load combinations, S_i the shape factor of an internal elastomer layer, n the number of internal layers, G the shear modulus of the elastomer, Δ_s the maximum shear deformation of the elastomer from applicable service load combinations, and h_{rt} the total elastomer thickness. L and W are the plan dimensions of a rectangular bearing and D is the diameter of a circular bearing.

2.5.5.2 Method B

Method B adopts a total shear strain approach, namely the explicit summation of the shear strain components at the steel-elastomer interface coupled with an amplification factor on cyclic components. Cyclic components include shear strains caused by traffic, earthquakes, and other transient loads. Thermal shear strains may not be counted as cyclic due to their low strain rates. The shear strain components corresponding to a specific deformation mode are depicted in Figure 2.7.

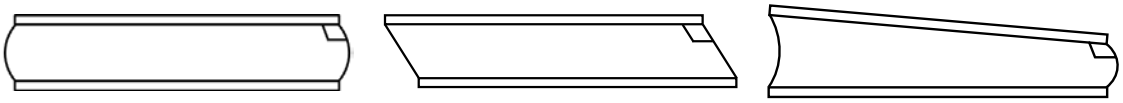

(a) γ_α (b) γ_s (c) γ_r

Figure 2.7: Shear strain at the steel-elastomer interface due to (a) axial load, (b) shear load, (c) rotation

The limit (γ_{cap}=5.0) for the total shear strain as a summation of the static values and the amplification of the cyclic components is not representative of the ultimate strain the material can withstand. Rather, it is an empirical limit, reflecting monotonic and cyclic test data (Stanton, Roeder et al. 2008) and is currently adopted by AASHTO (AASHTO 2012) and the European code (EN1337-3 2005). The shear strains due to each deformation mode are calculated according to equations summarized in Table 2.2.

Table 2.2: Shear strain components at the steel-elastomer interface

Bearing geometry	γ_α	γ_s	γ_r
Rectangular	$1.4\left(\frac{\sigma_s}{GS_i}\right)$	$\frac{\Delta_s}{h_{rt}}$	$0.5\left(\frac{L}{h_{ri}}\right)^2\frac{\theta_s}{n}$
Circular	$1.0\left(\frac{\sigma_s}{GS_i}\right)$	$\frac{\Delta_s}{h_{rt}}$	$.375\left(\frac{D}{h_{ri}}\right)^2\frac{\theta_s}{n}$

In the table above, h_{ri} is the thickness of an internal elastomer layer and θs the maximum service limit state rotation angle.

In addition to the total shear strain limits, Method B accounts for stability as a failure mode of the bearings. As a result, the design of taller bearings with reduced shear forces is permitted. The checks associated with stability include the comparison of two geometry-related factors *A* and *B*. The equations for those factors are as follows:

$$A = \frac{1.92\frac{h_{rt}}{L}}{\sqrt{1+\frac{2.0L}{W}}} \qquad \text{Eq. 14}$$

$$B = \frac{2.67}{(S_i+2.0)\left(1+\frac{L}{4.0L}\right)} \qquad \text{Eq. 15}$$

and the following condition should be satisfied: $2A \leq B$.

If the former condition is not satisfied the capacities should be compared to the average compressive stress. In the case of bridges where the deck is free to translate horizontally the following expression should be satisfied:

$$\sigma_s \leq \frac{GS_i}{2A - B} \qquad \text{Eq. 16}$$

If the bridge deck is fixed against horizontal translation the following expression should be satisfied:

$$\sigma_s \leq \frac{GS_i}{A - B} \qquad \text{Eq. 17}$$

For the purposes of this study, the first expression is used since the case of elastomeric bearings that are also used to accommodate horizontal translations will be addressed.

AASHTO also provides expressions for checking the thickness of the steel reinforcement against yielding and fatigue. However, for constructability purposes, particularly for bearings designed for higher demand applications, the thickness will always be larger than the minimum specified by AASHTO, which also includes expressions for the axial deflections.

2.6 Finite Element Modeling of Bearings

In order to simulate a steel-laminated elastomeric bearing in any Finite Element Method (FEM) formulation the steel and rubber materials must be simulated. Modeling steel in an elastomeric bearing is straightforward, especially since the steel plates in the bearing normally remain elastic. However, modeling rubber can be significantly more challenging.

Rubber having an isotropic, almost incompressible, non-linear elastic stress-strain relationship is often simulated by hyperelastic material models to capture this behavior. Hyperelastic material models express mechanical properties in terms of a strain energy density function (U). Each function (model) relates the strain energy per unit volume stored in the material with the strain or strain invariants at that point.

Parameters of these functions are often calibrated to match data from simple laboratory tests. In the case of steel-laminated elastomeric bearings, simple shear tests on the elastomer are commonly used for model calibration. Less often, the bulk modulus or laterally constrained uniaxial compression test is also used. The following section will describe some commonly used hyperelasticity models and expressions that are used for material calibration against experimental result. However, it should be noted that parameters obtained from a specific deformation mode should be used to simulate similar deformations with the finite element method approach.

2.6.1 RUBBER MATERIAL MODELS

As stated earlier, a hyperelastic material model describes the relation of the strain energy density function (U) with the state of strain at any point. As a result, the stresses can be expressed as a partial derivative of the strain energy density function (U) with respect to the first and second invariant of the right Cauchy-Green deformation tensor. The invariants are expressed in terms of stretch ratio (λ) or shear ratio (γ). The stretch (or the stretch ratio) λ is defined as the ratio of the length of a deformed line element to the length of the corresponding undeformed line element. The shear ratio γ is defined as the ratio of the relative lateral displacement of two undeformed line elements to their corresponding distance. The right Cauchy-Green deformation tensors and the respective invariants for the uniaxial compression and simple shear deformation modes are presented below.

Consider a rubber disk subjected to uniaxial compression. The deformation of such a rubber block is depicted in Figure 2.8.

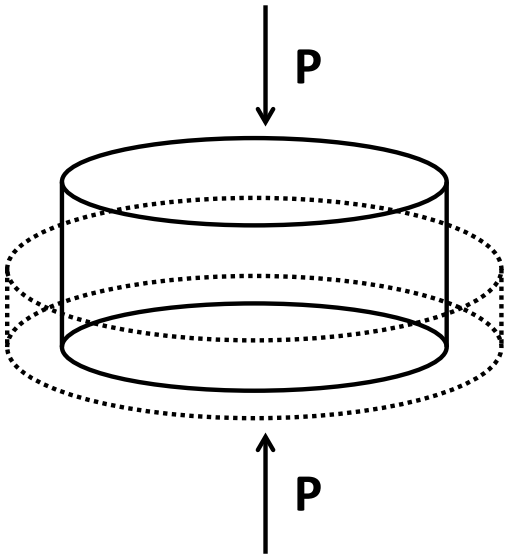

Figure 2.8: Uniaxial compression mode of deformation

The right Cauchy-Green deformation tensor for this deformation mode is:

$$\begin{bmatrix} \lambda^2 & 0 & 0 \\ 0 & \lambda^{-1} & 0 \\ 0 & 0 & \lambda^{-1} \end{bmatrix}$$

The respective strain invariants are:

$$I_1 = \lambda^2 + \frac{2}{\lambda} \qquad \text{Eq. 18}$$

$$I_2 = 2\lambda + \frac{1}{\lambda^2} \qquad \text{Eq. 19}$$

Consider a rubber block subjected to simple shear. The deformation of such a rubber block is depicted in Figure 2.9.

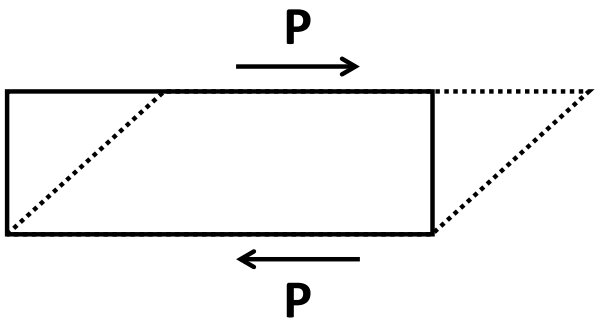

Figure 2.9: Simple shear mode of deformation

The right Cauchy-Green deformation tensor for this deformation mode is:

$$\begin{bmatrix} 1+\gamma^2 & \gamma & 0 \\ \gamma & 1 & 0 \\ 0 & 0 & 1 \end{bmatrix}$$

The respective strain invariants are:

$$I_1 = I_2 = 3 + \gamma^2 \qquad \text{Eq. 20}$$

Consider a rubber block subjected to bulk compression. The deformation of such a rubber block is depicted in Figure 2.10.

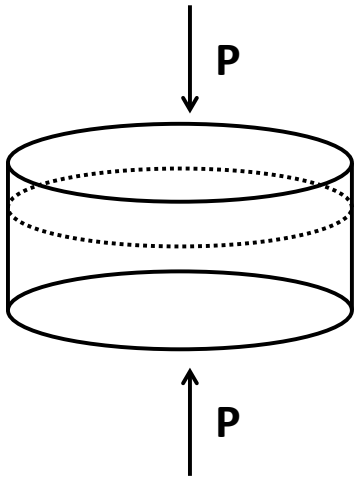

Figure 2.10: Bulk compression mode of deformation

The right Cauchy-Green deformation tensor for this deformation mode is:

$$\begin{bmatrix} \lambda^2 & 0 & 0 \\ 0 & 1 & 0 \\ 0 & 0 & 1 \end{bmatrix}$$

The respective strain invariants are:

$$I_1 = 2 + \lambda^2 \qquad \text{Eq. 21}$$

$$I_2 = 1 + 2\lambda^2 \qquad \text{Eq. 22}$$

Note that the invariants for this deformation mode are more complicated in form, due to the need to account for elastomer compressibility.

2.6.1.2 Mooney-Rivlin (1940) hyperelastic material model

The Mooney-Rivlin strain energy potential is

$$U = C_{10}(I_1 - 3) + C_{01}(I_2 - 3) + \frac{1}{D_1}(J_{el} - 1)^2 \quad \text{Eq. 23}$$

where C_{ij} and D_1 are material parameters, I_1 and I_2 are first and second strain invariants of the right Cauchy-Green deformation tensor, and J_{el} is the elastic volume ratio. The engineering stress expressions for the uniaxial compression, simple shear, and bulk compression modes of deformation are respectively:

$$\sigma_{11} = 2\left(\lambda - \frac{1}{\lambda^2}\right)(C_{10} + \frac{1}{\lambda}C_{01}) \quad \text{Eq. 24}$$

$$\sigma_{12} = 2(C_{10} + C_{01})\gamma \quad \text{Eq. 25}$$

$$\sigma_{11} = \frac{2}{D_1}(\lambda - 1) \quad \text{Eq. 26}$$

2.6.1.3 Neo-Hookean (Ogden 1997) hyperelastic material model

The Neo-Hookean strain energy potential is

$$U = C_{10}(I_1 - 3) + \frac{1}{D_1}(J_{el} - 1)^2 \quad \text{Eq. 27}$$

where C_{10} and D_1 are material parameters, I_1 is the first strain invariant of the right Cauchy-Green deformation tensor, and J_{el} is the elastic volume ratio. The engineering stress expressions for the uniaxial compression, simple shear, and bulk compression modes of deformation are respectively:

$$\sigma_{11} = \left(\lambda - \frac{1}{\lambda^2}\right)C_{10} \quad \text{Eq. 28}$$

$$\sigma_{12} = 2C_{10}\gamma \quad \text{Eq. 29}$$

$$\sigma_{11} = \frac{2}{D_1}(\lambda - 1) \quad \text{Eq. 30}$$

2.6.1.4 Yeoh (1993) hyperelastic material model

The Yeoh strain energy potential is

$$U = C_{10}(I_1 - 3) + C_{20}(I_1 - 3)^2 + C_{30}(I_1 - 3)^3 + \sum_{i=1}^{3} \frac{1}{D_1}(J_{el} - 1)^{2i} \quad \text{Eq. 31}$$

where C_{i0} and D_i are material parameters, I_1 is the first strain invariant of the right Cauchy-Green deformation tensor, and J_{el} is the elastic volume ratio. The engineering stress expressions for the uniaxial compression, simple shear, and bulk compression modes of deformation are respectively:

$$\sigma_{11} = 2\left(\lambda - \frac{1}{\lambda^2}\right)\left[C_{10} + C_{20}\left(\lambda^2 + \frac{2}{\lambda} - 3\right) + 3C_{30}\left(\lambda^2 + \frac{2}{\lambda} - 3\right)^2\right] \quad \text{Eq. 32}$$

$$\sigma_{12} = 2C_{10}\gamma + 4C_{20}\gamma^2 + 6C_{30}\gamma^3 \quad \text{Eq. 33}$$

$$\sigma_{11} = \frac{2}{D_1}(\lambda - 1) + \frac{2}{D_2}(\lambda - 1)^3 + \frac{2}{D_3}(\lambda - 1)^5 \quad \text{Eq. 34}$$

2.6.2 OTHER IMPORTANT PARAMETERS FOR MODELING

Selecting the appropriate material model parameters for the deformation mode and temperature under investigation is a crucial portion of elastomeric bearing modeling with the finite element method. However, other modeling aspects such as friction definition, mesh density, and element type need to be chosen based on the expected outcome of each finite element study. Each of these aspects is further discussed below.

2.6.2.1 Friction

When the slipping behavior of steel laminated elastomeric bearings without bonded sole plates is to be investigated, friction at the elastomer-concrete and the elastomer-steel interface needs to be considered. It is advisable to use a penalty-based Coulomb friction

model using a friction coefficient ranging from 0.3 to 0.4 (Muscarella and Yura 1995, Yura 2002). Although values for the coefficient of friction have been measured outside of this range at low temperatures, it is suggested to use a value of 0.3 and 0.4 for the elastomer-steel and the elastomer-concrete interface respectively. For cases where the domain of research is directly related to friction, the coefficient of friction should be reflecting relevant test data.

2.6.2.2 Mesh Density

Mesh size should be chosen based on mesh sensitivity studies for the analysis output parameters of interest. The use of approximately twenty elements over the length of the bearing has been shown to be adequate (Gerhaher, Strauss et al. 2011) to capture roll over behavior. The number of elements in the thickness direction needs to be determined by conducting a convergence study for the measure of interest (Gerhaher, Strauss et al. 2011). For the scope of this study, one layer of quadratic elements was used to simulate each elastomer layer.

2.6.2.3 Element type

When elastomer material is defined as hyperelastic and nearly incompressible, the use of hybrid elements is needed (Dassault-Systèmes 2012). Hybrid elements avoid numerical instabilities in displacement-controlled calculations by independently interpolating the pressure stress. Also, in order to avoid the “volume strain locking” and the “hourglass effect,” fully integrated elements or reduced integration elements with hourglass control should be used (Gerhaher, Strauss et al. 2011). Finally, the choice

between linear and higher order elements should be based on the convergence target and the output needs (e.g., to capture the effect of bulging of a bonded elastomer layer under compression, a minimum of either two layers of linear elements over the thickness or one layer of quadratic elements should be chosen).

2.7 Summary

This chapter has provided the background information steel-laminated elastomeric bearings. The chapter also presented the historical evolution of code provisions resulting from research on steel-laminated elastomeric bearings. Meanwhile, the lack of research on bearings used to accommodate large vertical reactions and significant translations and rotations was identified. To address this issue, the stiffness properties and strength limits should be known. This dissertation investigates the stiffness properties and strength properties of such bearings both experimentally and numerically in the following ways:

- The axial stiffness of a series of steel-laminated bearings is measured experimentally. The disagreement with theory is identified and possible explanations (friction, manufacturing imperfections) are investigated numerically.
- The shear stiffness of a series of steel-laminated bearings is measured experimentally with varying axial pressure and directivity. Disagreement with unique value of shear stiffness proposed by codes (GA/h) is identified and modified expressions are proposed as a result of an extensive parametric numerical study.
- The temperature-dependent material model coefficients of neoprene rubber for different hyperelastic material models are evaluated. In the absence of such information in the published literature, the evaluation of such coefficients is essential for the accurate numerical modeling of elastomeric bearings and was done concurrently with a companion study (Sun 2015).

- The strength limits of steel-laminated elastomeric bearings are evaluated experimentally. Those include tearing of elastomer (total shear strain) and stability.

CHAPTER 3: EXPERIMENTAL PROGRAM

3.1 Introduction

In order to gain a better understanding of the rubber and steel-elastomer composite layered behavior and performance a thorough experimental program was developed and conducted. The program is described in this chapter. Measurements of the basic material properties were necessary as well as the determination of the respective material coefficients, which are essential input for the subsequent parametric finite element studies that were a part of the overall research project and reported in Han (2016). Furthermore, the experimental studies were important to establish the fundamental behavior of the bearings with the range of load and deformational demands applied in service. The experimental program included both small-scale material tests on the elastomer that were presented by Sun (2015) as well as full scale steel-laminated elastomeric bearings that were tested in modes of deformation of interest. This dissertation presents the results from the full-scale tests and therefore, this chapter primarily focuses on full-scale experimental tests. The next section provides a brief overview of the small-scale material tests, conducted to develop coefficients for material models. Results are presented in Chapter 5. The remainder of the chapter outlines the full-scale testing program.

3.2 Material testing

Although extensive materials research has been previously conducted on elastomers and particularly neoprene rubber, no previous research studies were found with the intent to establish material coefficients considering the range of temperatures that the bridge bearings will see in practice. As hyperelastic material models do not utilize coefficients that can be measured by physical testing, representative material tests conducted by Sun (2015) were used to evaluate material coefficients for different models under a wide range of temperatures. Most coefficients were obtained through a series of shear and bulk compression tests since those modes of deformation are predominant in structural and mechanical engineering applications (Gent 2012).

3.2.1 TEST SETUP

The target of this research study was the use of elastomeric bearings in higher demand applications. The resulting bearings tend to be larger in both plan and thickness. Potential variations in the temperatures during the vulcanizing process raises questions on the resulting variations in the properties of the elastomer throughout the bearing. Therefore, a major aspect of the materials testing program was targeted at measurements of the variations in material properties across the width/length and thickness of the bearings. These tests were carried out in an MTS testing machine (Figure 3.1).

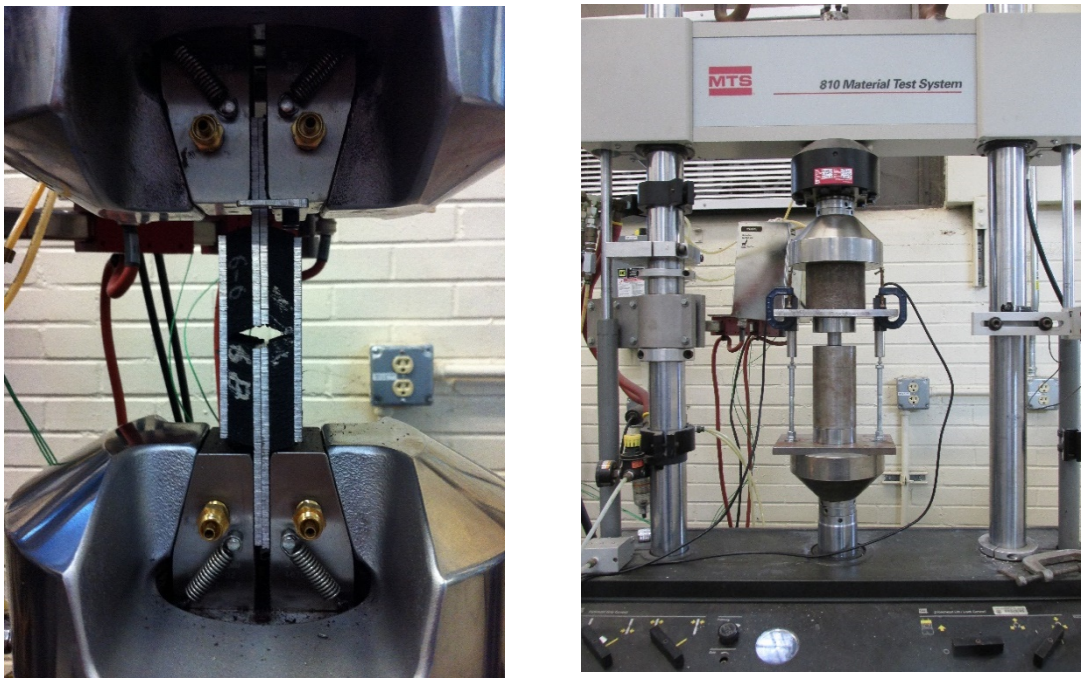

(a) (b)

Figure 3.1: Specimens being tested in (a) shear, (b) bulk compression in an MTS testing machine

These tests on the bearing properties were generally conducted at a temperature of 75 °F. However, bearings used in bridge applications experience a wide spectrum of temperature conditions with typical ranges from -10°F to 120°F (AASHTO, 2012). Tests utilized for the development of the material coefficients were conducted by Sun (2015) under temperatures between -4°F and 68°F. Depending on the loading conditions, the strain rate demands can vary from quasi static (thermal movements) to dynamic (earthquake/truck traffic). To capture the variety of cases in which the neoprene rubber material can be loaded, the test setup had to be able to operate under a wide range

temperatures. For temperatures under 32°F, an Instron testing hydraulic testing machine equipped with a cold temperature environmental chamber, seen in Figure 3.2, was used.

Figure 3.2: Instron material testing machine with environmental chamber

Sun (2015) developed a new shear testing method to determine the material properties of the bearings. Specimens were taken directly from the finished bearing and they were tested in shear, however only two rubber blocks were tested at a time. More information about the new testing method is presented in the Sun's doctoral dissertation (Sun, 2015). The new testing method was verified against the standard quad-shear test as per ASTM D4014 (2012), and it was found that both methods yield almost equivalent force deformation curves.

The specimens used for the material coefficient determination had dimensions as suggested in ASTM D4014 (2012) and were extracted from the bearing through successive cuts. They consisted of 4 identical neoprene rubber blocks bonded to steel plates being repeatedly pulled apart as illustrated in Figure 3.1a and Figure 3.3.

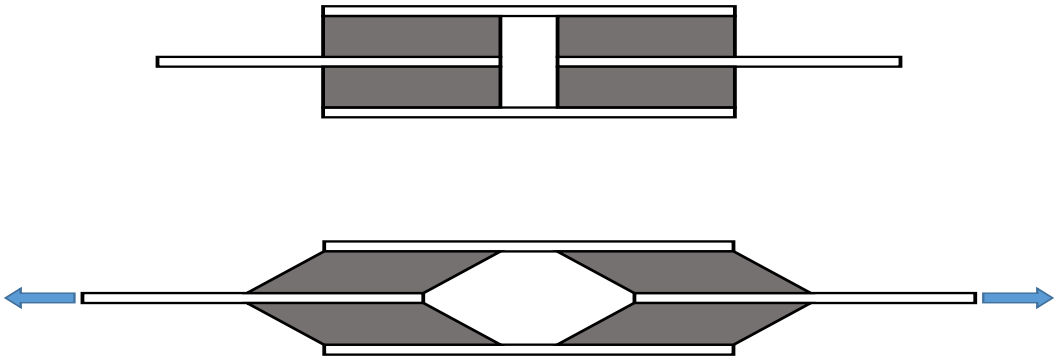

Figure 3.3: Quadruple shear test specimen in undeformed and deformed configuration

The specimens used for the bulk behavior determination consisted of a neoprene rubber cylinder machined to a tight-fit in a steel thick-walled cylinder. Steel pistons were used to compress the rubber piece as depicted in Figure 3.4.

Figure 3.4: Bulk compression specimen

More information about the test matrix and testing protocol followed during the tests is provided by Sun (2015).

3.2.2 MATERIAL COEFFICIENT DETERMINATION

In order to determine the material coefficients of the theoretical models for elastomers described in Chapter 2 the non-linear least squares algorithm was utilized. For determining the coefficients related to the hysteresis of the elastomer, where the closed formed solution parameters were not related to experimentally measurable values, a standard optimization method using a genetic algorithm was deployed. Each genetic algorithm generation was evaluated through an ABAQUS (Dassault-Systèmes 2012) run. The optimum result possessed recursive outcomes that were within 0.01% of each other. The results of this procedure are presented in Chapter 5.

3.3 Full scale bearing testing

The full-scale bearing tests in this study consisted of the testing of bearings that qualify as *higher demand applications*. Higher demand applications include the range of compressive stresses as well as the magnitude of the applied shear and rotational demands on the bearings. The larger forces and deformations lead to larger bearings in terms of the thickness and plan area of the bearings. The dimensions of the bearings that were tested are listed in Table 3.1.

Table 3.1: Test matrix of bearings tested

Bearing Pad	Width (in.)	Length (in.)	No. of "t"	Layer Thickness "t" (in.)	Cover (in.)	Steel Thickness (in.)	Total Height (in.)
XL	24	36	12	0.5	0.375	0.12	8.31
L	36	23	5	0.5	0.375	0.12	3.97
M	27	14	7	0.5	0.375	0.12	5.21
S	18	9	2	0.375	0.25	0.12	1.61

Each test specimen was labeled with bearing pad type letter (XL-L-M-S). The modes of deformation that were tested were:

- Pure compression
- Compression combined with shear (under different axial loads and different directions)
- Compression combined with imposed rotation

Due to geometric constraints and increased risk of damaging the test setup not all bearings were tested under all deformation modes. Each deformation-mode-specific sub-section that follows presents the bearings tested.

3.3.2 FULL SCALE COMPRESSION TESTING

This section is dedicated to the description of the test setup and testing protocol that was followed for the testing of bearings in compression. The purpose of the tests was to evaluate the axial stiffness of the bearings, as literature (Roeder, Stanton et al. 1989) suggested a potential discrepancy may exist between the calculated and measured axial stiffness, attributed to unknown reasons. Another purpose of the tests was to evaluate the current design limits for axial stress on bearings, as many previous studies were focused on smaller plan area bearings.

3.3.2.1 Test Setup

For this portion of the research investigation, a uniaxial self-reacting testing frame was developed for the experimental testing of full scale bearings. A schematic of the test-setup is shown in Figure 3.5. The test frame was capable of applying 4,000 kips in compression, a capacity dictated by the capacity of the hydraulic rams. The load was transferred from the actuators to the bearing through a stiff transfer beam. To avoid non-parallel movement of the self-reacting frame, restraining beams were placed on top and bottom of the system, as can be seen in Figure 3.6. To avoid the creation of a load path through the restraining beam, the connections were made through slotted holes, and Teflon (Polytetrafluoroethylene – PTFE) sheets were placed in the interface. To validate that there

were no differential movements, two linear potentiometers were placed at each side of the transfer beam to monitor displacements. The axial deformation of the bearing was taken as the average of the two recorded values.

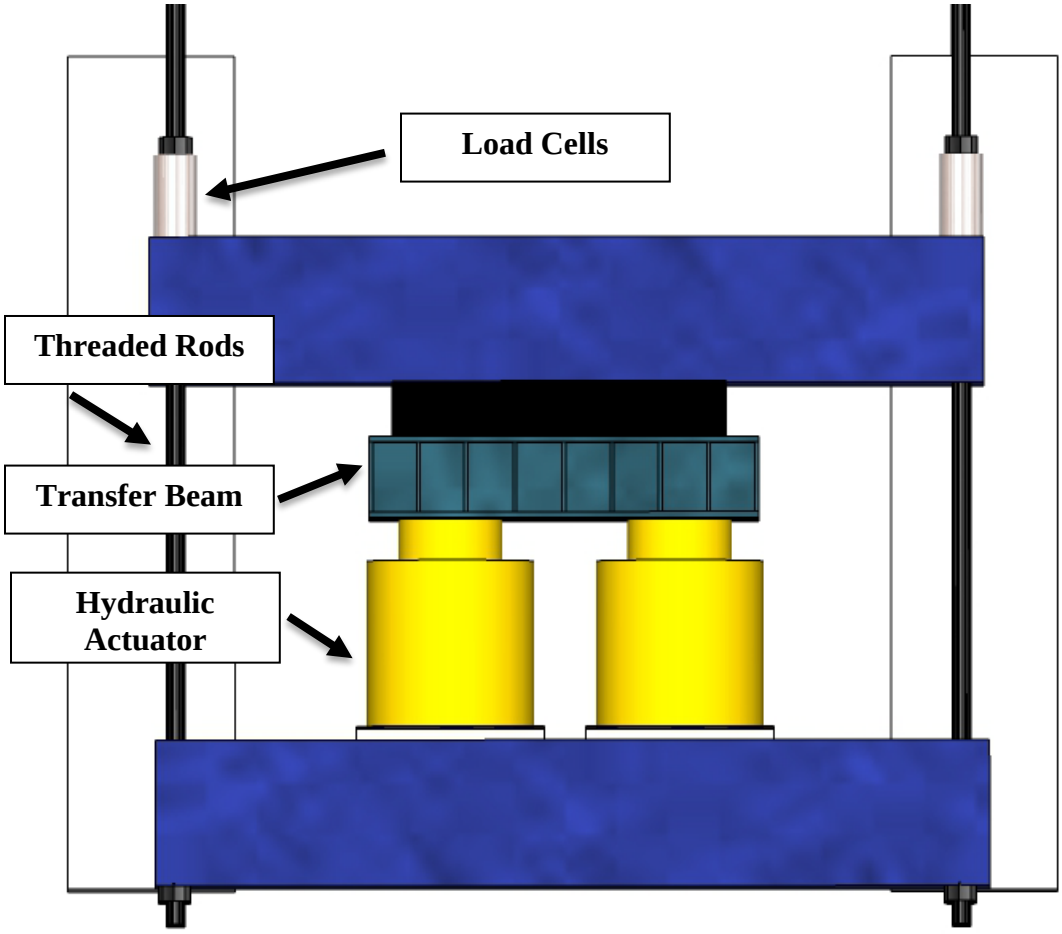

Figure 3.5: Schematic of the self-reacting test setup

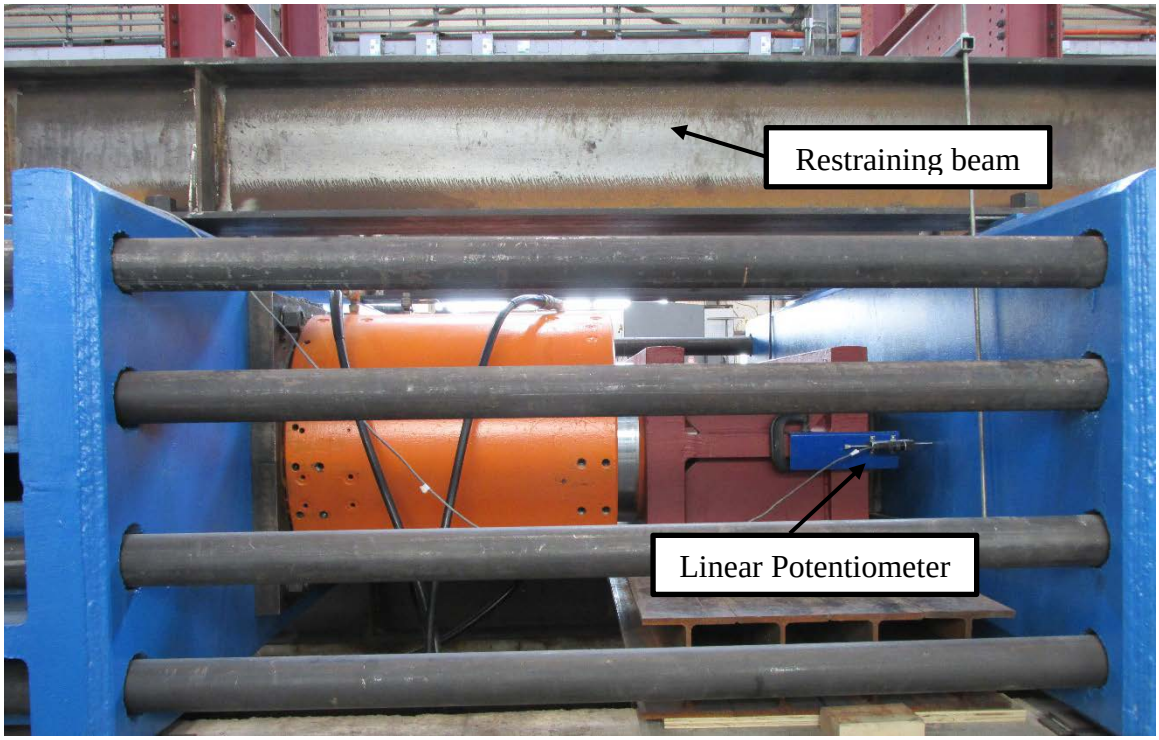

Figure 3.6: Test setup

3.3.2.2 Test matrix and testing protocol

To obtain the axial stiffness, each bearing was cyclically loaded to the target load six times. The reported stiffness is the value of the slope of the linear regression line of the loading portion of the sixth cycle. Each cycle duration was approximately 10 minutes. All the aforementioned bearing sizes were tested under compression.

As part of this research project, the bearing performance under large stress levels that exceed the current AASHTO (2012) design values was a major interest to evaluate the bearing behavior for use in *higher demand applications*. A bearing in compression under such levels can be seen in Figure 3.7.

Figure 3.7: Bearing tested in compression with observed shim misalignment

3.3.3 FULL SCALE SHEAR TESTING

This section is dedicated to the description of the test setup and testing protocol that was followed for the tests of bearings in shear. The purpose of the tests was to evaluate the shear stiffness in different directions and under various axial loads. In addition, the slip performance and the effect of rollover were assessed as well as the potential of buckling.

3.3.3.1 Test setup

The test setup developed for these experiments provided for the ability of shearing larger bearings at higher levels of axial stress. Figure 3.8 shows the setup, which consisted of two perpendicularly placed self-reacting frames. The horizontal frame is responsible for

applying the axial load and the vertical frame is responsible for shearing the bearing. As can be seen in Figure 3.9, in order to achieve the self-reacting ability of such a frame, two bearings were sheared simultaneously. In addition, for better representation of actual conditions (particularly for tests where the bearing may slip), two concrete blocks simulating the pier cap were added in the shearing plate without disturbing the symmetry of the self-reacting system.

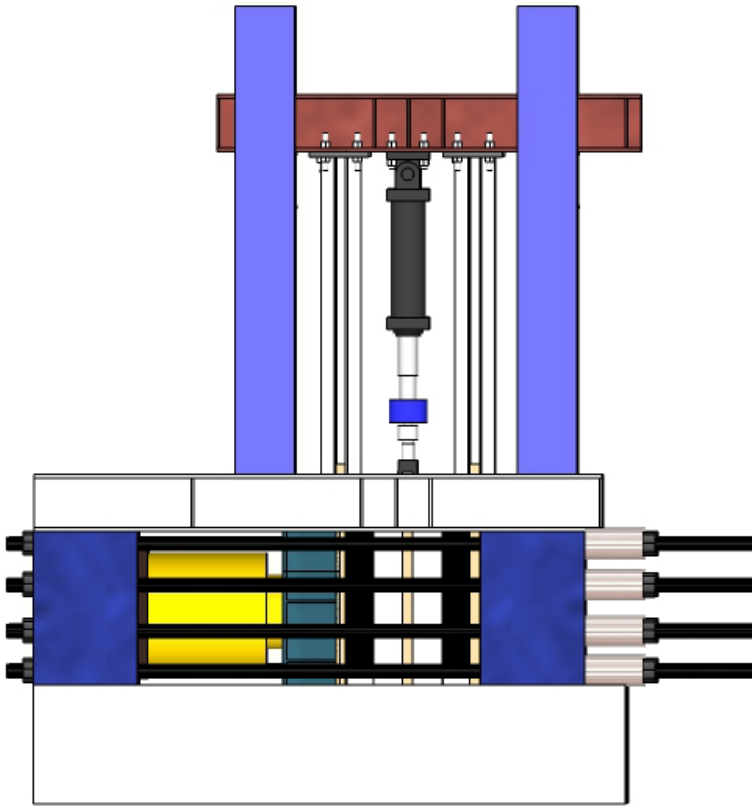

Figure 3.8: Schematic of the test setup

This setup permitted the measurement of the shear stiffness of the bearings to evaluate several components of the behavior, including:

1) Measurements of the shear stiffness in the different directions by rotating the bearing
2) The evaluation of the impact of the axial pressure on the shear stiffness,
3) Measurements of the friction coefficient between the bearing and the concrete/steel
4) Measurements of the potential for rollover of the bearing.

Figure 3.10 depicts the test setup as constructed at FSEL and Figure 3.11 illustrates a bearing with applied shear to it. The rollover phenomenon can be seen at the top left and bottom right edges.

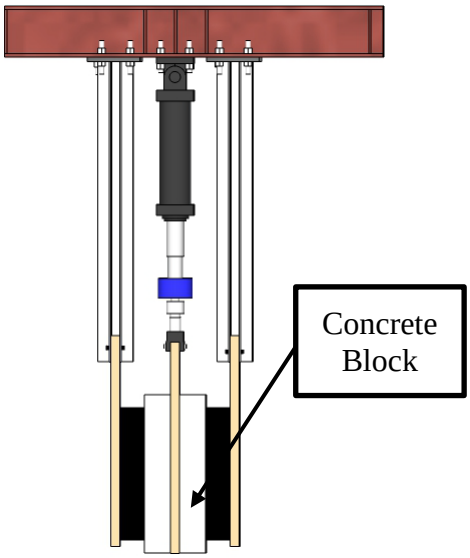

Figure 3.9: Schematic of the self-reacting shear frame

Figure 3.10: Combined axial and shear test setup at FSEL

Figure 3.11: Bearing tested in shear

3.3.3.2 Test matrix and testing protocol

As stated previously, the main purpose of the full-scale experiments was to evaluate the shear stiffness properties of the bearings, to validate the material tests results, to obtain a better understanding of the behavior under various axial loads, and to gain data for validation of the FEA models that were used in the study. In addition, the rollover occurrence was visually assessed.

Table 3.2 presents the main variables of the tested bearings as well as the naming scheme used in the investigation. Table 3.3 summarizes the tests that were conducted for each specimen. It is worth noting that tests associated with 50% of the maximum allowable axial load with current AASHTO design procedure and 100% shear strain were not conducted in the initial portion of the study to minimize the risks of instabilities caused by eccentricities in axial load induced in the system by differential slipping.

Table 3.2: Test matrix of bearings tested in shear

Bearing Pad	Width (in.)	Length (in.)	Layer Thickness "t" (in.)	Total Height (in.)	Shape Factor	Aspect Ratio
S	18	9	0.375	1.61	8	2
M	27	14	0.5	5.21	9.22	1.93
L	36	23	0.5	3.97	14.03	1.57

Table 3.3: Matrix of conducted tests

Shear Strain Level / Axial Stress Level	50% Shear Strain			75% Shear Strain			100% Shear Strain		
	S	M	L	S	M	L	S	M	L
0.5 ksi	✓	✓	✓	✓	✓	✓	✗	✗	✗
0.8 ksi	✓	✓	✓	✓	✓	✓	✓	✓	✓
1.0 ksi	✓	✓	✓	✓	✓	✓	✓	✓	✓
1.5 ksi	✓	✓	✓	✓	✓	✓	✓	✓	✓
2.0 ksi	✓	✓	✓	✓	✓	✓	✓	✓	✓

In order to define the shear stiffness of the bearing the procedure followed was consistent the procedure specified in the material-level portion this study (Sun 2015). Specifically, the shear stiffness was defined as the slope of the line determined by points in the deformation curve associated with the 0.2 and 0.4 elastomer shear strain. This process in conceptually illustrated in Figure 3.12.

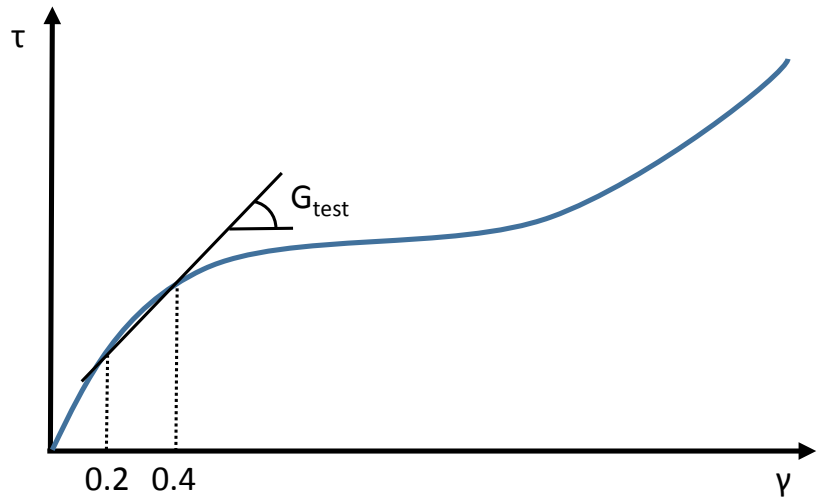

Figure 3.12: Shear stiffness definition

The fact that the expected location of the bearings was not accessible by the laboratory crane due to vertical constraints (beams holding the shear self-reacting system in place), a procedure for placing and engaging the specimens was developed. Consequently, the bearings were initially placed on supports, seen in Figure 3.13, fabricated to ensure the bearing placement at a location concentric with the location of the applied load and the bearing placement at the expected angle. Subsequently, the test setup was moved at the bearing support location and the outside plates were clamped, creating a sandwich structure that did not allow the bearing to fall when the shear test setup was placed in its designated position. The clamped configuration is depicted in Figure 3.14. Finally, an initial axial load of 20 kips was applied to ensure that the bearings didn't slide under gravity loads and the clamps were removed. The pre-testing configuration is shown in Figure 3.15.

Figure 3.13: Bearings on supports before being placed in the shear test setup

Figure 3.14: Clamped configuration entering the test setup

Figure 3.15: Test setup with engaged bearings

A testing protocol consisting of two parts was followed throughout the shear tests in the study. After reaching a target axial load, each bearing was sheared five times to the desired shear strain. The duration of each cycle was approximately one minute. At the end of the fifth cycle the axial load was increased to the next desired level and the process was repeated until the maximum target axial load was reached. After the process was completed, the axial load was dropped to the clamping load of 20 kips. The bearing was left in place overnight to release the stresses that had built-up due to the inherent rubber hysteretic behavior and the testing was resumed the following day under the same protocol for a different maximum shear strain. The maximum axial load and maximum shear strain applied in this testing phase, 2 ksi axial pressure and 100% shear strain, respectively. However, after the completion of the testing protocol, higher axial loads and shear strains were applied in an effort to evaluate the failure limits for those devices, without damaging the test setup. A graphical representation of the protocol followed is illustrated in Figure 3.16.

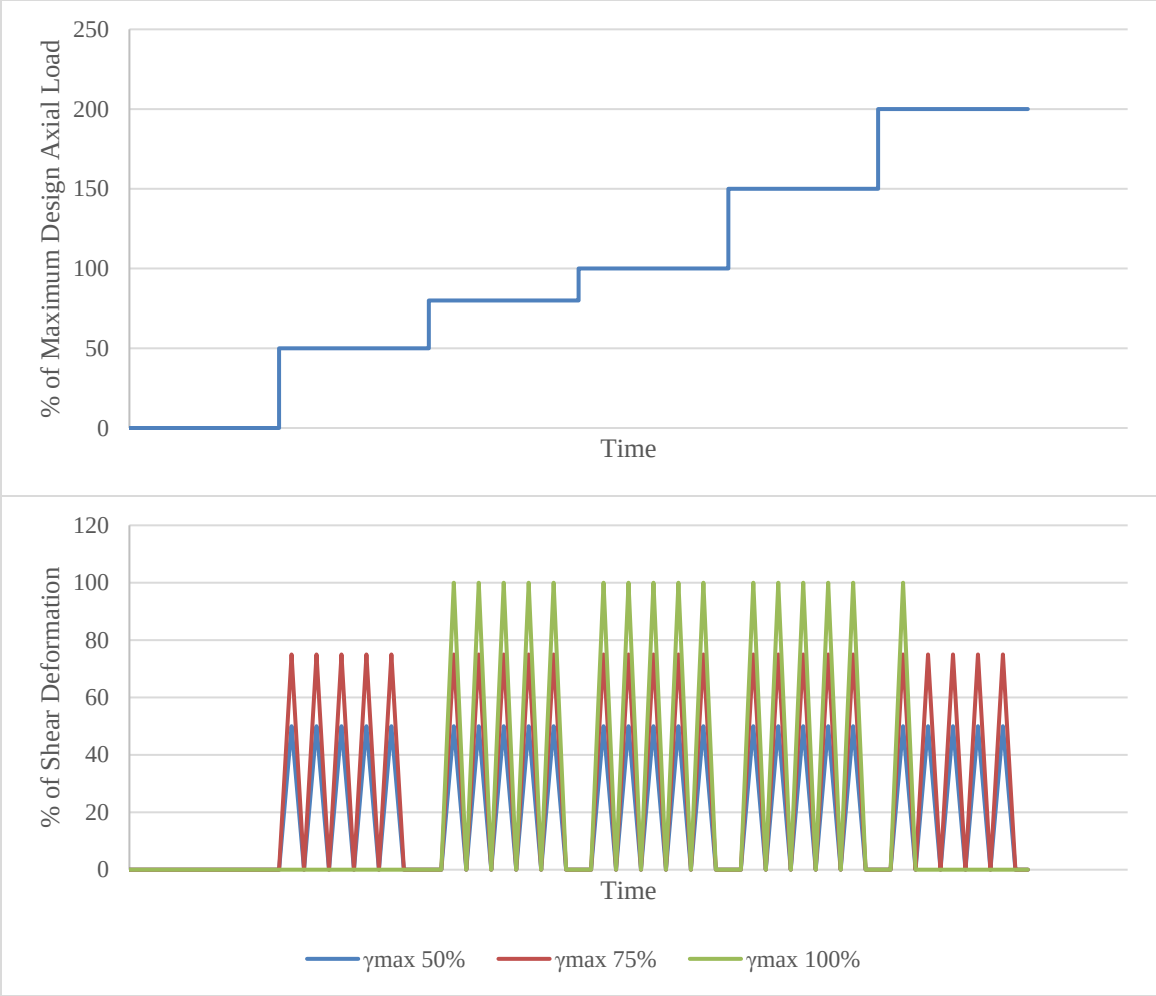

Figure 3.16: Testing protocol

3.3.4 FULL SCALE ROTATIONAL TESTING

This section describes the test setup and testing protocol that was followed for the rotational tests on the bearings. The purpose of these tests was to evaluate the rotational stiffness and strength of the bearing and investigate the effects of the lift-off phenomenon, which is the situation that arises when the girder rotation leads to a separation between the bearing surface on one side and the girder flange.

3.3.4.1 Test setup

An extensive review of the literature on previous bearing tests did not provide any information of previous testing programs in which setups were developed capable of accommodating compression, shear, and rotation for elastomeric bearings with the load and displacement requirements necessary for bearings used in qualifying as higher demand applications. Stanton et al. (2008) made use of a setup capable of compression, shear, and rotations; however, that setup was limited in capacity to accommodate and test conventional size bearings. Such a setup was found to be impractical to accommodate bearings classified for higher demand applications due to the much larger load and deformational limits.

The approach taken in this part of this study was to make use of the test setup used in the compression and shear portions of the investigation. The application of rotational deformations at the bearings utilizing an external load source such as a lever system was not an option due to the inherent instability of the self-reacting system configuration. Instead of an imposed force, an imposed rotation was chosen to be applied to the bearings by means of compressing two inclined surfaces against the two bearings. In order to achieve the desired angles of rotation in the range of 0.5 to 2.0 degrees (0.009 and 0.035 radians) the inclined surfaces were created by attaching machined aluminum shims at the plates of the shear self-reacting system, as depicted in Figure 3.17.

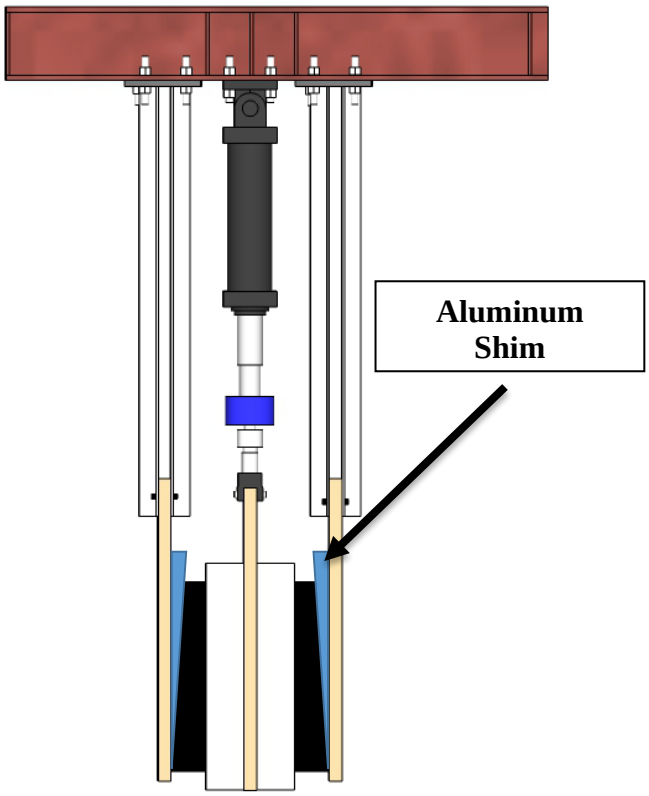

Figure 3.17: Modification to the shear test setup for rotation

There were three primary objectives for the rotational tests. The first objective was to assess the rotational stiffness and strength of the bearing as a function of the axial load/stress. The second objective was focused on the lift-off phenomenon for bearings that classify for higher demand applications. Lift-off is permitted by AASHTO in the design of elastomeric bearings, however those provisions reflect conclusions from research conducted in significantly smaller bearings. The final objective of the rotational tests was obtaining data for the FEA studies for use in validating the models in this mode of deformation and producing failure identification processes.

In curved bridges shearing of the bearing as well as the rotation of the girders occurs in two perpendicular directions. In the case of lift-off, when shearing and lift-off occur in two perpendicular directions, the shearing will typically occur over a localized region of the bearing which will often result in torsion in the bearing. The setup that was developed, allowed this phenomenon to be also experimentally investigated.

3.3.4.2 Test matrix and testing protocol

After the bearings were inserted in the test setup, axial load is applied using the two actuators with a capacity of 2 million lbs. each. Because the axial loads were applied to the bearings through the angled shims, the resulting deformations on the bearings is combined axial compression at a fixed rotation as shown in Figure 3.18. Figure 3.19 depicts the expected high shear strains at the compression side of the bearing.

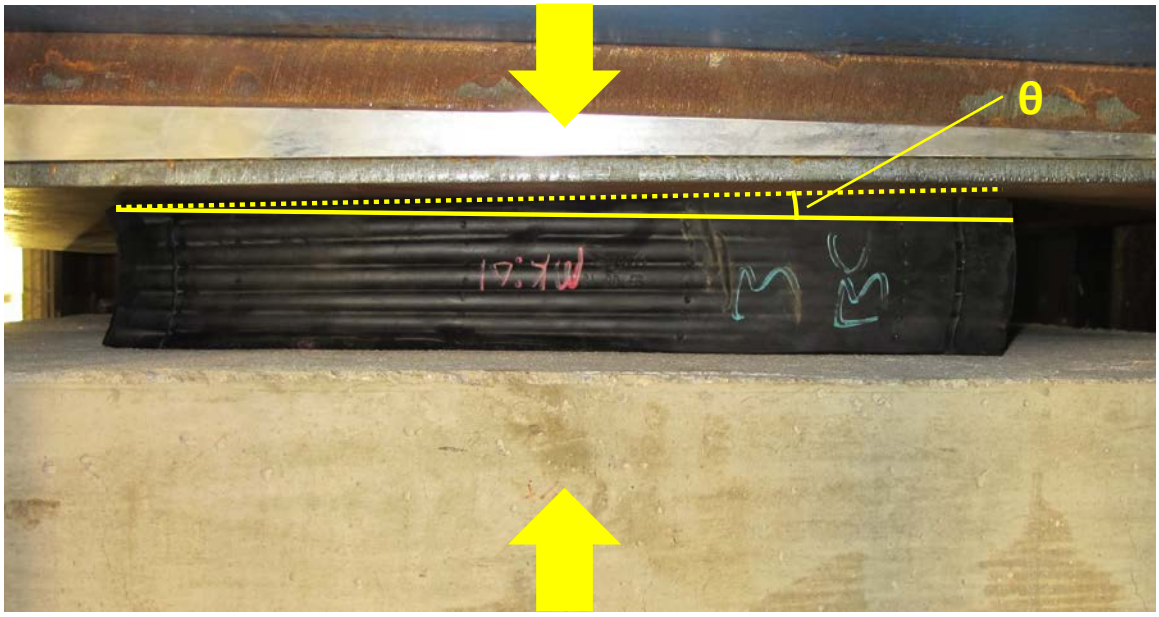

Figure 3.18: Compression-induced rotation at a bearing

Figure 3.19: Increased local shear deformations noticeable at the compression side of the bearing

Due to geometrical constraints caused by the size of the test setup, smaller size bearings were not tested in rotation. Table 3.4 presents the main variables of the tested bearings. The test protocol consisted of axially loading the bearings for a given rotation implied for specific shims.

Table 3.4: Test matrix of bearings tested in rotation

Bearing Pad	Width (in.)	Length (in.)	Layer Thickness "t" (in.)	Total Height (in.)	Shape Factor	Aspect Ratio
M	27	14	0.5	5.21	9.22	1.93
L	36	23	0.5	3.97	14.03	1.57

3.4 Summary

This chapter provided an overview of the experimental program that included both material tests as well as full scale testing of the bearings. The purpose of the laboratory experiments was to:

- Establish sets of material coefficients for the neoprene material under different temperatures (material level testing).
- Evaluate properties of bearings in compression, shear, and rotational deformation modes (full-scale testing).
- Assess the accuracy of the total shear strain approach to be applied in higher demand application bearing design.

Results obtained from the experimental program are described in Chapter 5.

CHAPTER 4: DESCRIPTION OF NUMERICAL SIMULATIONS

4.1 Introduction – Purpose of Numerical Simulations

In an effort to obtain a better understanding of the information learned from the experimental studies, and to gain insights into some of the disagreement between theory and experimental results, a series of numerical simulations were developed and performed for steel-laminated elastomeric bearings. This chapter provides a description of the modeling techniques used in the numerical simulations, and a description of the simulations that were conducted to evaluate the effect of laminate imperfections on the axial stiffness of steel-laminated elastomeric bearings and the effect of axial load and shear directivity on the shear stiffness. This chapter is limited to describing the analysis techniques and analysis cases. The results of this study are presented in Chapter 6. Note that additional extensive numerical simulations were conducted in a companion study to this project, and are reported by Han (2016).

4.2 Modeling Techniques

The three-dimensional numerical simulations of the steel-laminated elastomeric bearings were conducted in the general purpose finite element software ABAQUS (Dassault-Systèmes 2012).

4.2.1 GENERAL DESCRIPTION

The models utilized solid elements simulating the alternating steel and rubber layers. The bond between rubber and steel was simulated by merging their coinciding nodes at the interface, effectively imposing a continuity constraint. This is a reasonable assumption for working stress levels and typical manufacturing procedures as debonding is not expected under loading within design limits for a properly manufactured bearing.

Each model was comprised of:

- Two analytical rigid plane surfaces simulating the substructure and the superstructure. The bottom surface, which simulated the substructure (pier cap or abutment), was fully fixed. The top surface, simulating the superstructure (bridge girder), was the surface where the forces or displacements were applied. The magnitude of those forces and displacements were case-specific, and are discussed in subsequent subsections. The preference of analytical rigid over discrete rigid is a result of reduced computational effort and is discussed more thoroughly in the Contact Definition subsection.

- A series of alternating steel and rubber layers, with the case-specific geometry. The dimensions and number of layers ensured that the variables of interest (i.e. shape factor, aspect ratio, imperfection, total rubber thickness) were accurately modeled. In general, the layers are described as rectangular prisms. In the imperfection study the shape of the layers is described in the Model Description subsection.

The geometry definition of a steel-laminated elastomeric bearing is simple as it consists of a series of alternating prisms, bounded by two surfaces. An example of a meshed bearing can be seen in Figure 4.1.

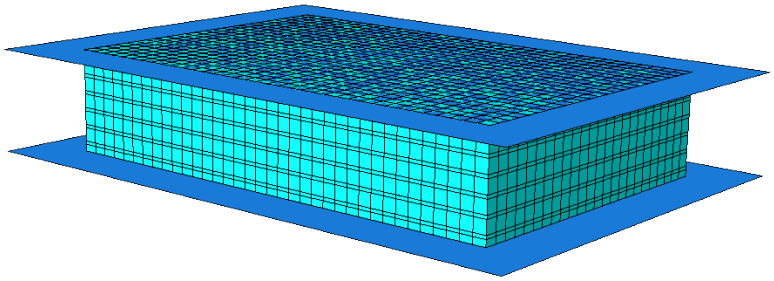

Figure 4.1: Meshed bearing model

4.2.2 MATERIAL MODELS

This subsection provides a description of the material models used for steel and rubber in the simulations.

4.2.2.1 Steel

Steel was simulated with a bilinear elastic-plastic material law. Per the manufacturer's specification, the nominal mechanical properties of ASTM A36 steel were used for the steel laminate. The yield stress was equal to 36 ksi and Poisson's ratio was equal to 0.3. Young's modulus was set equal to 29000 ksi and post-yielding tangent modulus was set at 150 ksi. It is noted that yielding was not expected to occur in the simulations, but the bilinear material law was chosen to allow the evaluation of more loading cases in future analyses that might result in yielding of the steel laminates.

4.2.2.2 Rubber

As discussed in Chapter 2, hyperelastic material models are used to simulate rubber behavior. As seen in Chapter 5, a good fit was obtained for all material models that were considered (i.e. Yeoh, Mooney-Rivlin, Neo-Hookean models). The Yeoh material model (1993) was utilized for simulating the neoprene material at room temperature throughout the numerical studies. This material model had been used in previous and concurrent studies on elastomeric bearings at The University of Texas at Austin (Nguyen and Tassoulas 2010, Sun 2015, Han 2016). The following hyperelastic material coefficients were used for the numerical studies:

C_{10}=61.65 psi; C_{20}=-56.15 psi; C_{30}=88.69 psi;

D_1=6.70E-06psi; D_2=3.00E-08psi; D_1=3.00E-9psi

More information on the material testing and parameter determination can be found in Sun (2015) and in Chapter 5.

4.2.3 ELEMENT TYPE AND MESH

The rubber and steel components of the elastomeric bearing model utilized the C3D20RH element type of ABAQUS. C3D20RH is a continuum/brick (C), three-dimensional (3D), 20-node, quadratic, reduced integration (R), hourglass control, and linear pressure, hybrid element (H). It was selected against the 8-node and the 20-node fully-integrated elements because of its efficiency during the computational simulations. The use of a hybrid element was necessary as a result of the almost incompressible material behavior.

A mesh sensitivity study was performed to optimize the computational time needed for the analyses without jeopardizing the accuracy of results. The characteristic element dimension was varied between 0.125 in. and 0.5 in., resulting in one to four elements per rubber layer. Every time the element size was halved, the computational cost was increased by approximately one order of magnitude.

Table 4.1: Apparent modulus results for mesh sizes considered

Characteristic Element Length (in.)	E_A/E	Difference (%)
0.125	484.1	-
0.25	482.2	-0.4
0.5	482.7	-0.3

Table 4.1 shows differences in the axial stiffness of a fully bonded rubber layer (L/W=1, S=20) as obtained by analyses with different characteristic element lengths. As can be seen, the selected characteristic element length was not significantly affecting the measure of interest. The characteristic element length of 0.5 in. was chosen for the analyses. This was the maximum element size that could be used without violating the ¼ aspect ratio limit due to the shim thickness of 0.125 in.

4.2.4 CONTACT DEFINITION

In order to apply the desired pressure, rigid top and bottom plane surfaces were defined. The definition of those surfaces allowed the measurement of forces and displacements as those rigid surfaces have only 6 degrees of freedom (3 translational and 3 rotational), all associated with the analytical rigid surface reference point; the centroid of the rigid surface. The purpose of simulating portions of the model assumed as rigid surfaces is computational efficiency, especially when the modelling invokes contact element definitions. Analytical rigid surfaces were chosen over discrete rigid surfaces as they resulted in even lower computational costs when utilized with contact properties (Dassault-Systèmes 2012).

For the cases where the effect of friction was investigated, a penalty-based formulation for the contact interaction was defined. The penalty-based formulation allows some relative motion between the contact surfaces, although the friction force is not overcome. This modeling is preferred to overcome numerical difficulties associated with singularity points when using the ideal *Coulomb friction* model. The relative motion allowed, or "elastic slip", is a small fraction (≈0.05%) of the characteristic element length, enough to mitigate the computational difficulties without affecting the overall behavior. The elastic slip value should be defined as the minimum value that does not lead to numerical difficulties for convergence. The abovementioned process is depicted in Figure 4.2. This method was chosen due to its increased numerical stability for the range of contact pressures considered herein.

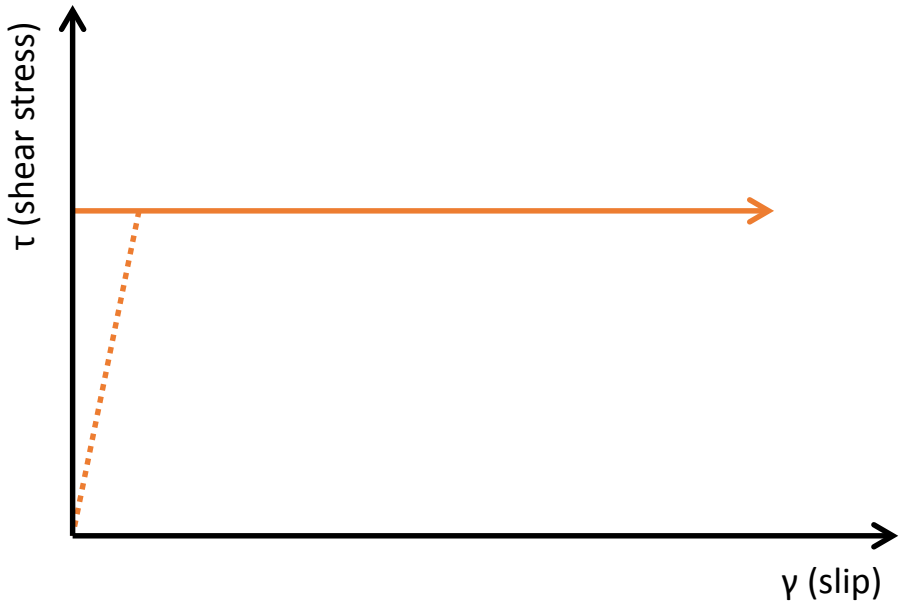

Figure 4.2: Frictional behavior with Coulomb friction (solid line) and penalty friction (dotted line) formulation

4.2.5 SOLVER

The Abaqus/Standard (Implicit) solver was utilized for all the simulations. The solver imposes equilibrium of internal forces with externally applied loads at each increment through Newton-Raphson iterations. The stiffness matrix of the numerical model is also updated prior to each incremental solution attempt. This allows for larger increments throughout the analysis leading to effectively lower computational costs.

4.2.6 MODEL VALIDATION

As described earlier, numerical studies were conducted in an effort to understand and evaluate discrepancies between theoretical predictions and experimental observations.

This effort was carried out through a series of parametric studies, as described later in Chapter 6, in which assumptions concerning the configuration (i.e. perfectly straight and parallel configuration) and loading (simple shear) of the steel-laminated elastomeric bearing were relaxed. As a result, the model was benchmarked for validity against theoretical predictions without the assumptions relaxed. The two benchmark problems were the following two:

- Axial Stiffness of Bonded Rubber Blocks
- Rubber Blocks in Simple Shear

4.2.6.1 Axial Stiffness of Bonded Rubber Blocks

For this benchmark problem two cases were investigated. Two rectangular prismatic rubber layers bonded to steel laminates with different shape factors (S=10 and S=20) were axially loaded with a pressure of 1000 psi. The pressure-deflection curves and stiffness values were obtained from the FEA analyses and were evaluated against theoretical predictions. The two cases were selected such that in the first case (S=10) the axial stiffness was dominated by shearing (bulging) of the elastomer, and in the second case (S=20) the axial stiffness was dominated by volumetric compression resistance. Table 4.2 summarizes the properties of the layers for the benchmark cases that were considered.

Theoretical models, presented in Chapter 2, have been developed for predicting the axial stiffness of rectangular bonded rubber layers. Figure 4.3 illustrates the increase in the apparent modulus of rubber for a range of shape factors accounting for rubber compressibility, as predicted by models discussed in Chapter 2, for a square plan area layer.

Table 4.2: Properties of Axial Stiffness Benchmark Cases

Case	Length (in.)	Width (in.)	Thickness (in.)	Shear Modulus (psi)	Bulk Modulus (ksi)	Shape Factor
1	10	10	0.25	100	338	10
2	20	20	0.25	100	338	20

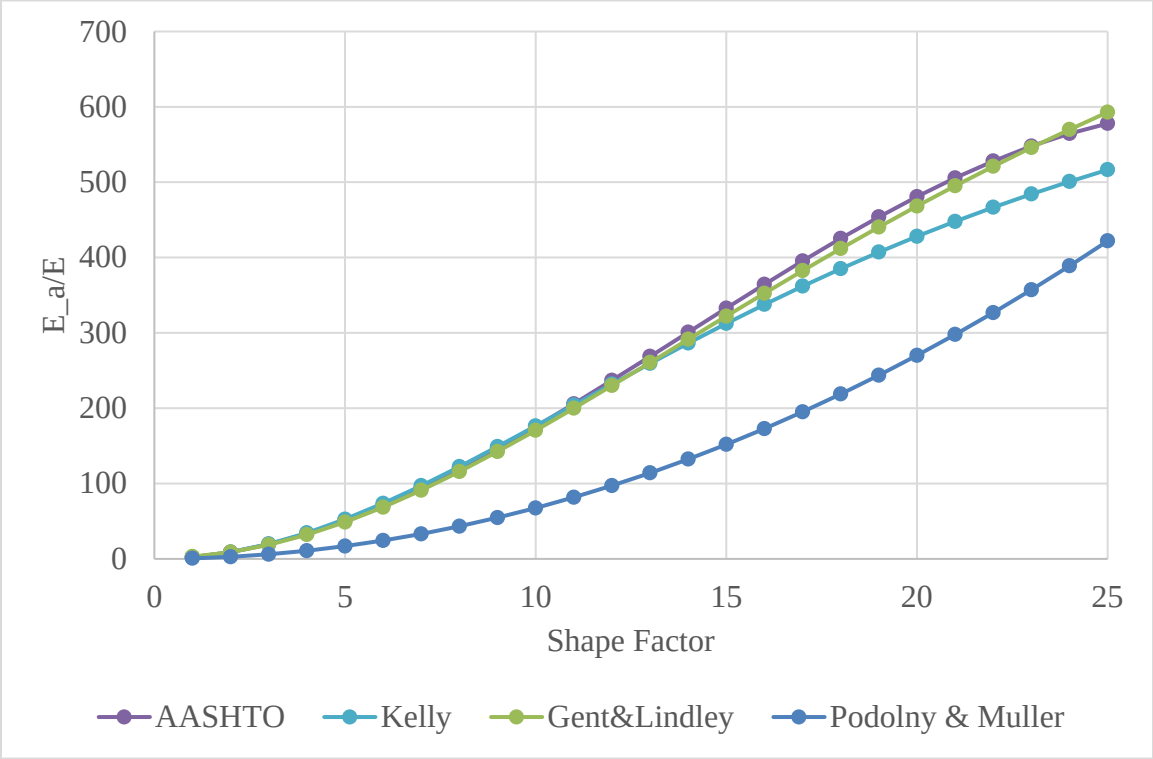

Figure 4.3: Effect of shape factor on apparent modulus to Young's modulus ratio (L/W=1.0, E/K=1500)

As can be seen, apart from the Podolny & Muller (1994) prediction, which is purely empirical, all other models predict approximately the same increase in apparent stiffness as a function of the shape factor. For comparison purposes, the FEA results were compared

with predictions from Kelly et al.(2011). The comparison is summarized in Table 4.3. Difference are attributed to:

- Linear material assumption prediction equation (Van Engelen and Kelly 2014).
- Approximation of material properties used in the prediction equation compared to the material properties used for the FEA.
- Numerical approximations.

Table 4.3: FEA vs. theoretical apparent axial modulus prediction comparison

Case	Ea/E (FEA)	Ea/E (Kelly et al.)	Difference (%)
1	185	176	4.74
2	434	428	1.41

Figure 4.4 illustrates the two layers employed for the axial stiffness benchmark testing in a rainbow contour scheme for displacement magnitudes. Reds imply increased displacements and blues indicate regions of displacements close to zero. Apart from the measure of interest (i.e. the axial stiffness) two more observations support the validity of the models. First, the displacements are larger (reds) close to the middle of the layer at the middle of the side, and tend to zero at corners and at the steel material. Second, bulging is more prominent in Case 1, as expected, due to the larger restraint against bulging as a consequence of the higher shape factor (S). All of the above suggest the validity of the models utilized in the parametric study with the regards to the axial bearing behavior.

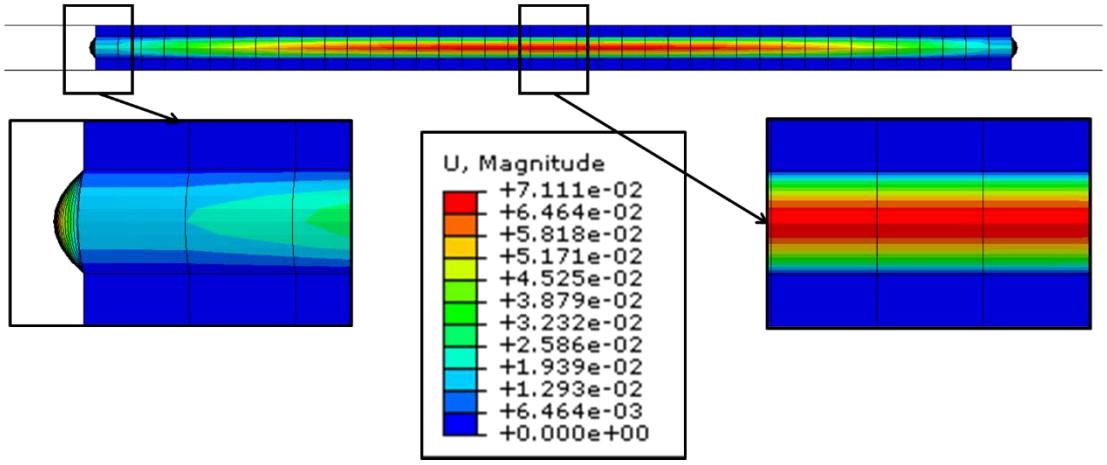

(a)

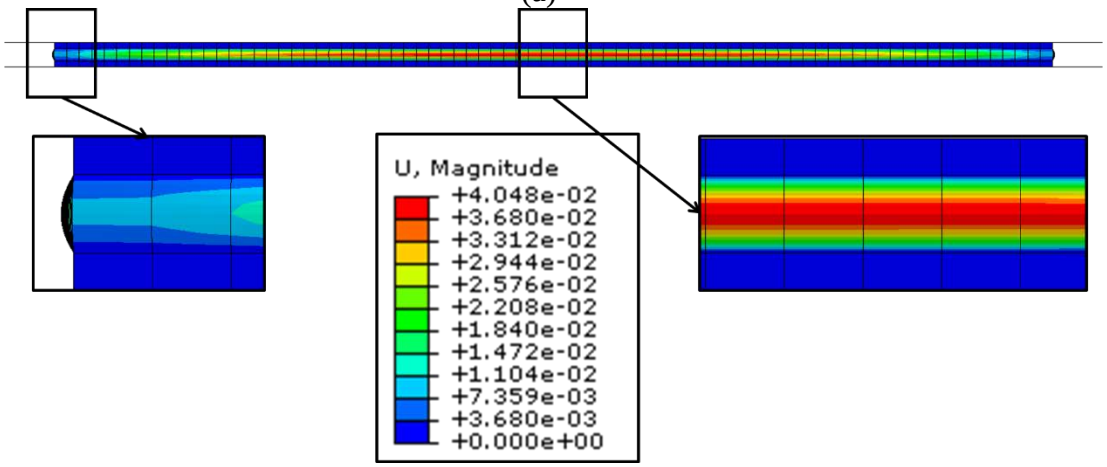

(b)

Figure 4.4: Displacement contours of benchmark models under compression (elevation view); (a) Case 1 and (b) Case 2

4.2.6.2 Rubber Blocks in Simple Shear

For this benchmark problem, the same rubber layers were modeled with the difference lying only in the loading condition. The loading condition was simple shear and the target shear strains were set to 50%. This implies that a displacement at the top relative

to the bottom of the rubber layer equal to half of the layer thickness was applied. The expected force required to simply shear the rubber layer at the aforementioned shear strain is $\frac{GA}{h_r}\Delta\gamma \cdot h_r = \frac{GA}{2}$. The results were compared with theoretical predictions and are presented in Table 4.4.

Table 4.4: FEA vs. theoretical shear force prediction comparison

Case	Force FEA (kips)	GA (kips)	Difference (%)
1	5.02	5	0.39
2	20.08	20	0.40

As can be seen the differences between the FEA and the theoretical predictions are small. Figure 4.5 illustrates the two layers under a top steel layer deflection of half the layer thickness. As expected, the strain field is uniform in the layer, a fact attributed to the small dimension of the thickness relative to the other layer dimensions.

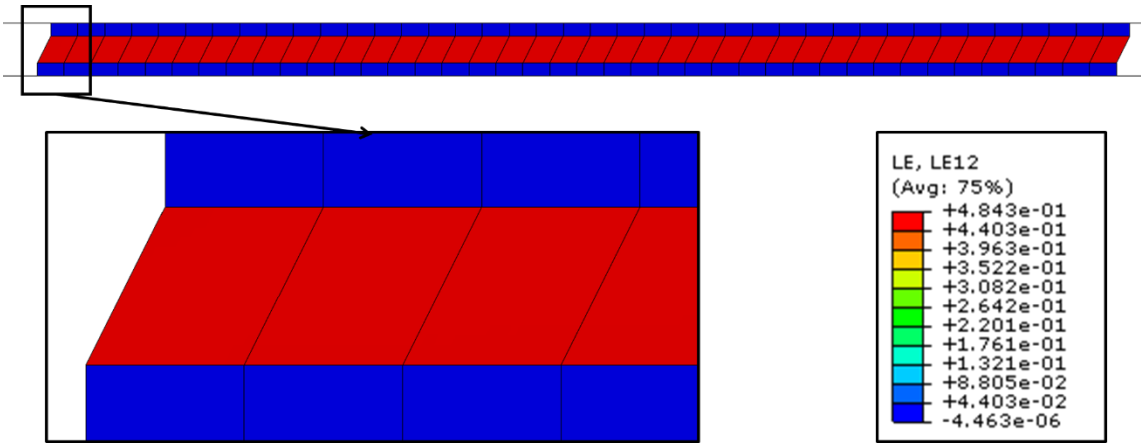

(a)

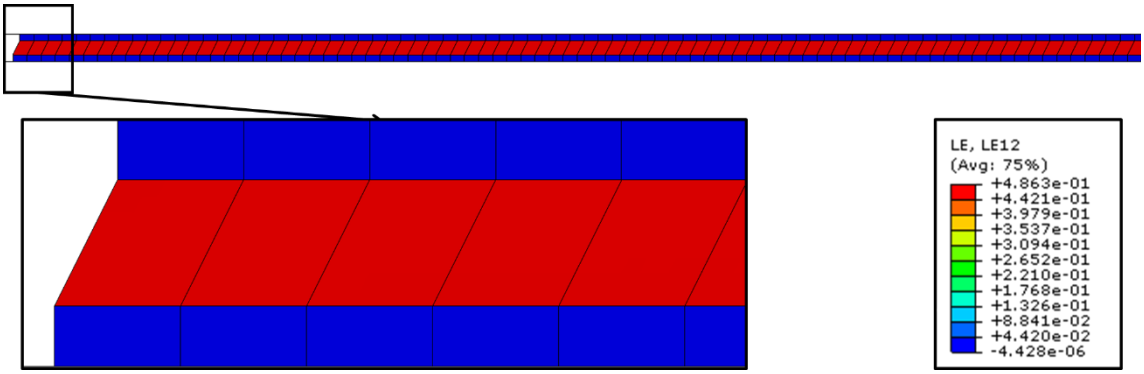

(b)

Figure 4.5: Shear strain contours of benchmark models under simple shear (elevation view); (a) Case 1 and (b) Case 2

The results of the shear benchmark problem were in a better agreement than the axial stiffness benchmark results, possibly due to the following reasons:

- The better numerical approximation of the shear modulus compared to the bulk modulus of the elastomer

- Simpler state of deformation as the compression of the layer combines shear deformations and bulk compression, as explained in Chapter 2.

4.3 Effect of imperfections on the axial stiffness of elastomeric bearings

The assumption of bonded rubber blocks in series has been used for determining the axial stiffness of steel-laminated elastomeric bearings (AASHTO 2012). This assumption, however, assumes perfectly parallel rigid shims, fully bonded to the rubber, as depicted in Figure 4.6.

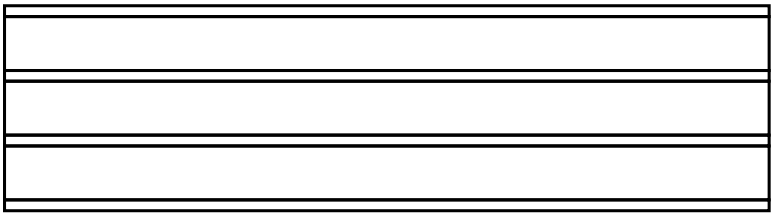

Figure 4.6: Schematic (elevation) of a bearing with perfect steel laminates configuration without rubber cover layers

Figure 4.3 represents axial stiffness values for ideal system configurations. However, due to manufacturing practices, perfectly straight and parallel configurations are rarely obtained (Anderson, Mott et al. 2004). The section cut shown in Figure 5.13 shows the existence of simultaneous misalignment and bent shim imperfections. In addition, in common practice the cover layers are rarely bonded to the substructure and the superstructure (Bradberry, Cotham et al. 2005). As a result, the transfer of forces from the superstructure to substructure is relying on the friction between the bearing and the substructure and the bearing and the superstructure. The effects of those conditions (i.e. bent shim imperfections, misalignment, and friction), not taken into consideration in the design calculations, are investigated independently in this portion of the study.

4.3.1 IMPERFECTION CONFIGURATIONS – SHIM BENDING

Steel-laminates, being thin steel plates, are prone to have an imperfect shape with out-of-straightness values varying with their overall dimensions as well as their thickness. During the vulcanization process, the rubber material is more prone to deformations due to the high temperatures and pressures under which the bearing is cured, due to unavoidable flow in the mold (Yerzley 1939). The final product may qualitatively look similar to that illustrated in Figure 4.7.

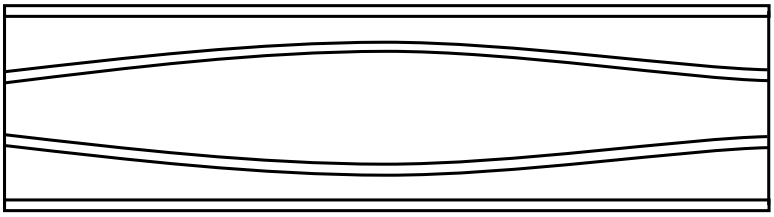

Figure 4.7: Schematic (elevation) of a bearing with steel shim bending

As can be seen, the result of such imperfections is the creation of regions where bulging is less restrained and thus the resulting axial stiffness is lower.

4.3.2 IMPERFECTION CONFIGURATIONS - SHIM MISALIGNMENT

Another case where the restraint against bulging can be locally reduced is the case of straight, non-parallel steel laminates, as was observed in cuts, shown in Figure 5.11. This can be caused by the malfunction of seats, usually located at the bearing corners, used for keeping the steel laminates at specified locations during the vulcanization process. A sketch of such an imperfection is shown in Figure 4.8.

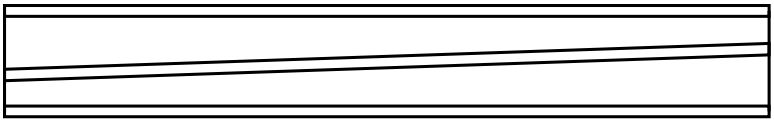

Figure 4.8: Schematic (elevation) of a bearing with misaligned steel laminates configuration

4.3.3 MODEL DESCRIPTION

To evaluate the effects of imperfections on the axial stiffness of the bearing, Finite Element models incorporating those imperfections were developed. Although the imperfections described in the previous paragraphs can occur simultaneously, as seen in Chapter 5, in this study their effect on the axial stiffness of the bearing is evaluated independently. Also, for reasons of computational efficiency, the impact on axial stiffness was calculated for three layers and two layers for the case of bending imperfection and misalignment, respectively. Friction cases utilized only one layer of rubber as they pertain only to cover layers.

4.3.3.1 Bending cases – 3 rubber layer models

For the case of bending imperfections, the model utilized three layers of elastomer and four layers of steel. The imperfections were modeled only in the two middle steel laminates such that the top and bottom steel layers remain parallel, as can be seen in Figure 4.7. The geometric imperfections were modeled as half-sine waves, ranging from perfectly straight up to an out-of-straightness of 75% of the layer thickness. Bending of the plates was assumed to occur in only one direction. Analyses were conducted for r 32

combinations of shape factors and plan area aspect ratios, ranging from 8 to 20 and 1.0 to 2.0, respectively. A total of 192 combinations were considered. The axial stiffness for each combination was determined after imposing an axial stress of 1000 psi, as this is a common design value for bridge applications. Figure 4.9 depicts an extreme configuration of bent shims evaluated in this study.

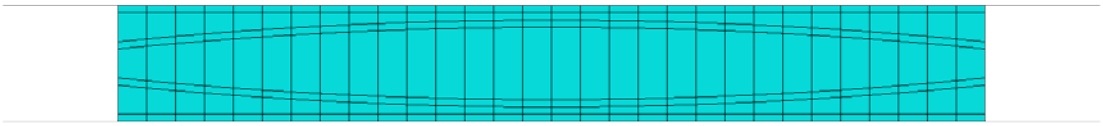

Figure 4.9: Elevation of an imperfect shim case configuration (shim bending)

4.3.3.2 Misalignment cases – 2 rubber layer models

For the case of the misalignment imperfections, the model utilized two layers of elastomer and three layers of steel. The imperfections were modeled only in the middle steel layer by changing the elevation at which the ends of the layer were located. Sixteen cases of imperfections were investigated for all the shape factors and plan aspect ratios considered in the previous study, totaling in 512 cases. The imperfection values ranged between -¼ in. (-50%) and ¼ in. (+50%) misalignment of the left and right edges along the short edge of the bearing. As before, the axial stiffness was evaluated at the axial stress level of 1000 psi. Figure 4.10 depicts an extreme configuration of misaligned shims evaluated in this study.

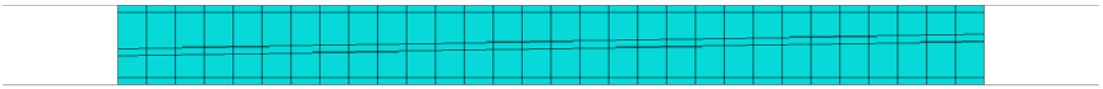

Figure 4.10: Elevation of an imperfect case shim configuration (shim misalignment)

4.3.3.3 Friction cases

In order to evaluate the effect of the friction coefficient on the axial stiffness, FE models with friction coefficients ranging from 0.2 to 0.5 in increments of 0.05 were developed. The range of the coefficients was representative of the range of values measured for rubber in contact with steel and concrete (Muscarella and Yura 1995). The models utilized a single rubber layer, fully bonded on one side and having a frictional contact interaction defined on the other side. The cases were analyzed for the same shape factors and aspect ratios described above, resulting in 160 cases analyzed. As in all previous cases, the axial stiffness was obtained at an axial stress level of 1000 psi. All comparisons were made with the stiffness of the respective fully bonded case. Figure 4.11 illustrates the displaced configuration of a typical friction case analysis. It can be seen that the magnitudes of displacements are significantly higher than the bonded equivalent (Figure 4.4a). Also, the fact that the contact algorithm is imposed only at nodal locations creates penetrations of the surfaces, noticeable close to the edge locations. This effect could be mitigated at the expense of computational efficiency by increasing the mesh resolution. However, for the measure of interest in this study (i.e. axial stiffness) is was found that the improvement in

accuracy would be same as the levels presented in Table 4.1. Therefore, the mesh for this portion of this study was kept unchanged.

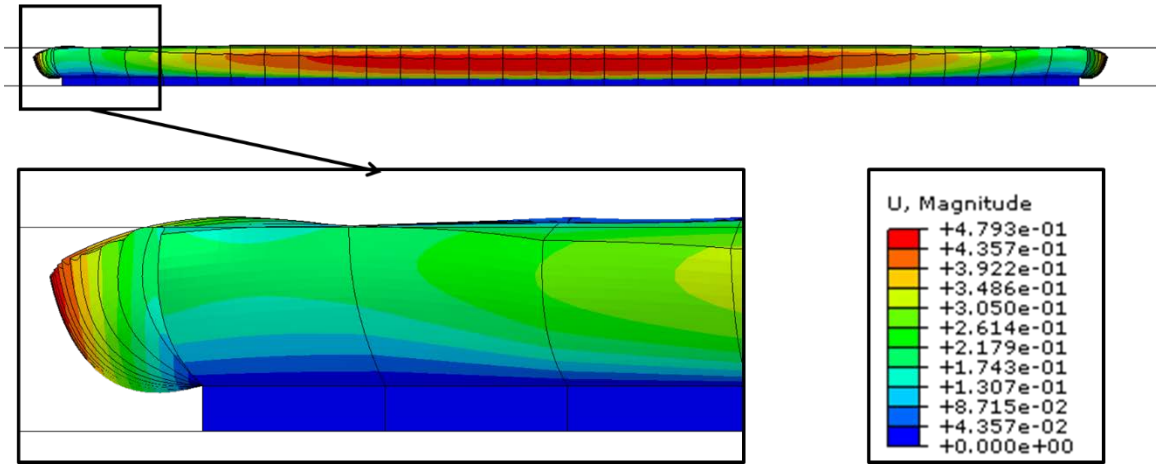

Figure 4.11: Elevation results of a friction case configuration

4.4 Effect of shear directivity and axial pressure on the shear stiffness of elastomeric bearings

Bearings that would qualify for higher demand applications should accommodate large axial loads, shear deformations, and rotations. This often leads to tall bearings relative to their height with plan area aspect ratios greater than 1.0. Although the shear stiffness has been investigated previously, no research has been conducted on shear in taller bearings. The aim of this portion of the study was to validate experiments conducted on taller bearings, that showed directional dependence of the shear stiffness, as discussed in Chapter 5, and to evaluate the shear stiffness variability under different shearing directions and different axial pressures for a range of plan area aspect ratios and length-to-height ratios.

4.4.1 MODEL DESCRIPTION

A matrix of simulations was developed to capture plan area aspect ratios (L/W) and width to total rubber height (W/h_{rt}) ratios of interest (1.0 to 2.0 and 10 to 2.5 respectively) for axial pressures of 1000, 1500, and 2000 psi. The combinations considered are depicted in Figure 4.12. The simulation was performed through a two-step procedure. First, the axial pressure was applied. Subsequently, a shearing deformation equal to half of the total rubber height was performed at 15 degree increments. The limits were representative of typical design limitations and engineering practice, and a total of 525 cases were modeled. The steps followed are illustrated in Figure 4.13. The material parameters described in the previous sections were used in the case of the directional stiffness investigation as well.

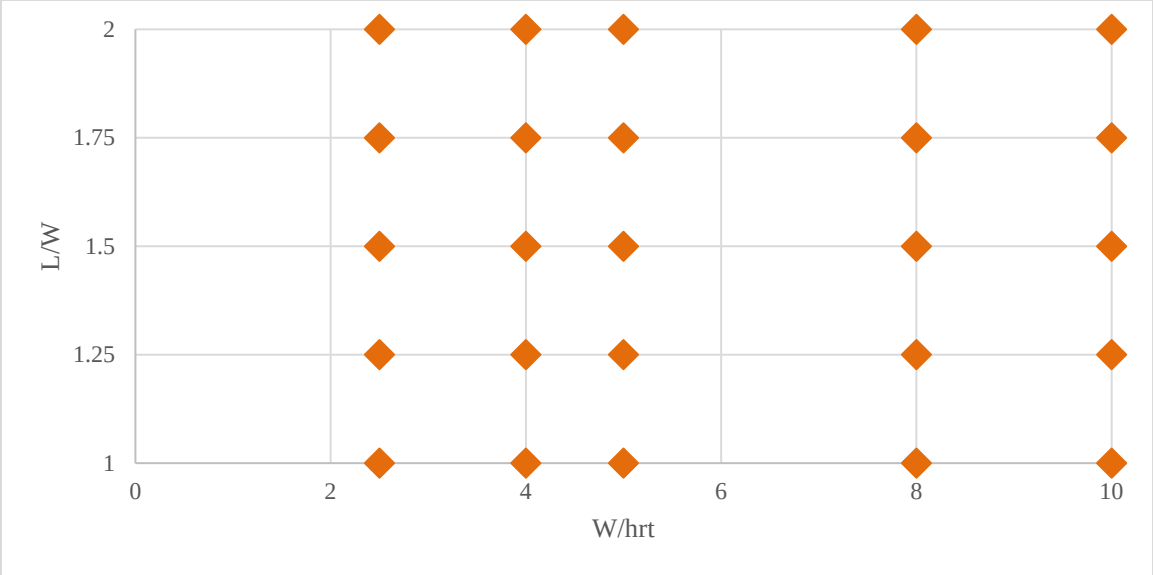

Figure 4.12: Combinations of L/W and W/hrt considered

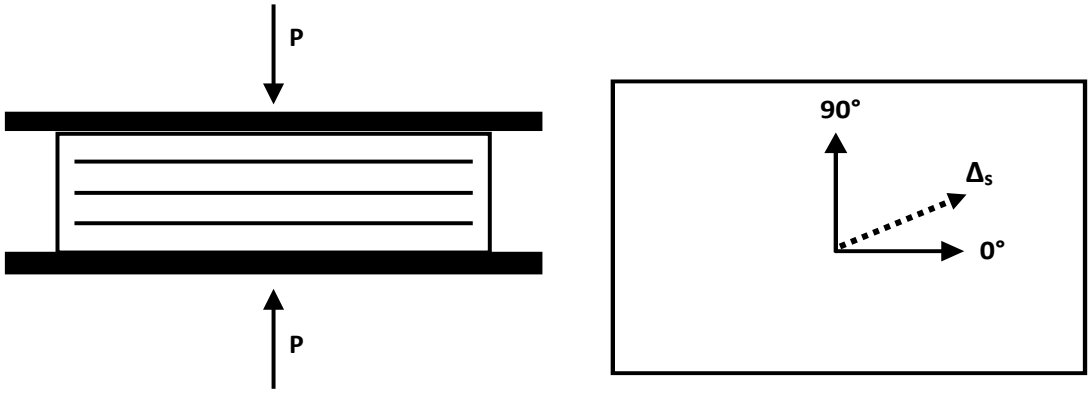

(a) Step 1: Compression (elevation view)

(b) Step 2: Shearing (plan view)

Figure 4.13: Steps followed for the shear directivity evaluation study

The influence of accounting for friction in the models was firstly evaluated. The alternative was to merge the end nodes of the cover layers with the nodes of the top and

bottom rigid surfaces, through which the loads were applied. The evaluation was performed by comparing the friction and tied cases at 15 degree increments for two different bearing height extremes (10 and 2.5 ratio of length to height for the short and tall bearing respectively) and a constant plan aspect ratio of 2.0 to take into account any potential geometry dependence. The bearings under consideration can be seen in Figure 4.14.

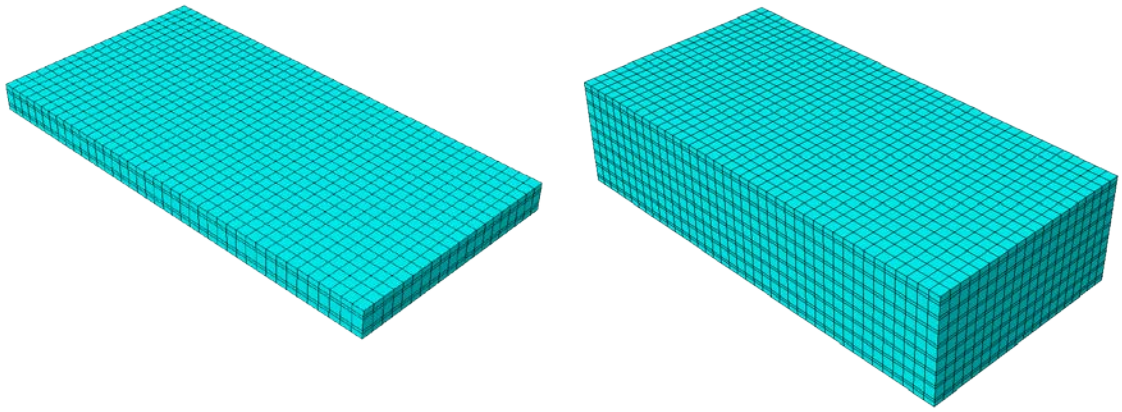

(a) (b)

Figure 4.14: Models used for friction evaluation on directivity; (a) Short bearing and (b) Tall bearing

As can be seen in Figure 4.15 the difference between the friction and the tied cases was negligible for the shorter bearing. For the taller bearing the difference remained below 10%. It is also noticeable that the difference is increasing as the shearing direction is approaching the shearing along the short direction. Assuming that the effect of friction is not significantly affecting the measure of interest, the analyses were performed with the end nodes merged with the end plates to save significant computational cost, associated with the presence of penalty-based contact.

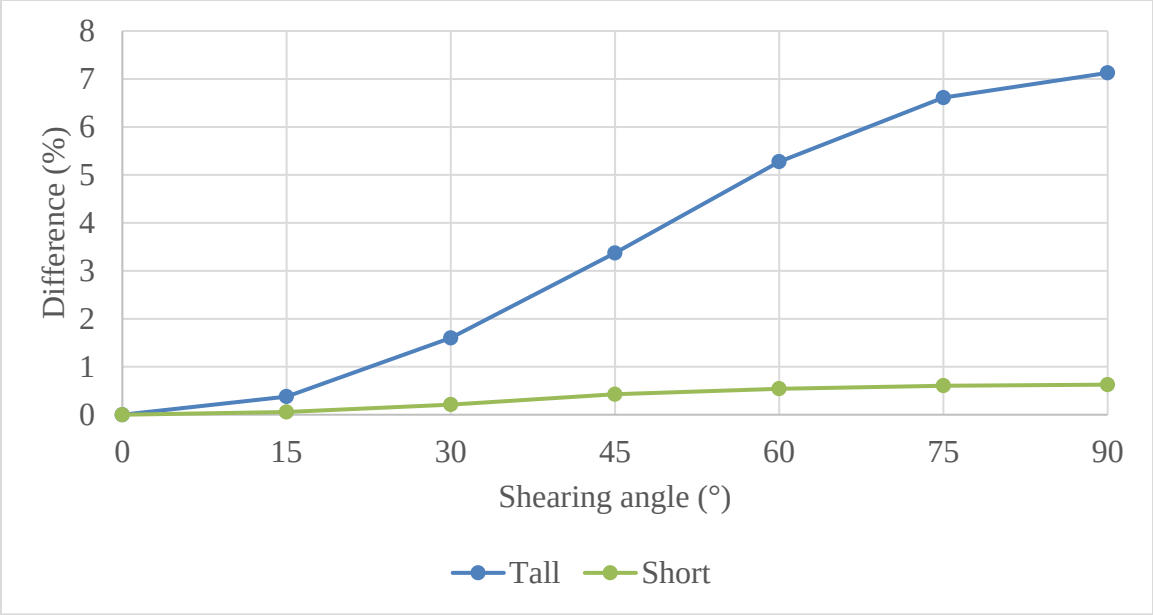

Figure 4.15: Differences in calculated shear stiffness between friction ends and tied ends for a tall and a short bearing

4.5 Summary

This chapter provided an overview of the techniques, methods, and processes that were employed for the numerical simulations that were conducted as part of this research program. Briefly, the purpose of the numerical simulations was to:

- Evaluate the impact of imperfections and friction on the axial stiffness of steel-laminated elastomeric bearings. The simulations were conducted in an attempt to understand the disagreement between theoretical predictions and experimental testing. Sources of imperfections were assumed to be the steel laminate geometry and placement and the amount of friction (friction coefficient) that the cover layer experiences.
- Evaluate the impact of the shear directivity and axial pressure on the shear stiffness of the bearing. The simulations were conducted in an effort to gain knowledge on why the predictions of simple shear are not observed in experimental testing.

Results of the numerical simulations are presented in Chapter 6 of this dissertation.

CHAPTER 5: RESULTS – EXPERIMENTAL PROGRAM

5.1 Introduction

This chapter focuses on the results obtained from the material portion and the full scale portion of the study. The material tests that are discussed in this chapter complement the material tests carried out by Sun (2015). The primary purpose of the material test results that are presented in this chapter was to obtain a measure of the bulk modulus. An overview of the data obtained is presented and the reasoning behind the rationale of the proposed design for elastomeric bearings is described.

Following this introduction, the chapter starts outlining the experimental test results at the material level for neoprene elastomer. Representative test curves for each mode of deformation at different temperatures are presented and material coefficients for the different models presented in Chapter 2 are derived. Subsequently, full-scale experimental results are presented along with test observations. Cases where theory or design provisions did not match with experimental results are related to test observations (i.e. axial stiffness – imperfections and directional shear stiffness – no dominant simple-shear loading). The relation hypothesis is investigated numerically in Chapters 4 6. Strength limits were confirmed to be rational, as no failure was observed for total shear strains higher than current AASHTO limits. Last, a summary of important findings is provided.

5.2 Material test results

Due to the lack of previous tests on material coefficients for the neoprene rubber used in bridge bearing applications, neoprene rubber material with Durometer hardness 50 was tested (Sun 2015) in simple shear and volumetric compression. Apart from providing the source for reliable material modeling for the numerical portion of this study, presented in Chapters 4 and 6 of this dissertation, the tests were conducted and coefficients were derived for a range of temperatures applicable to bridge bearing applications.

5.2.1 TYPICAL RESULTS

This section is focused on the results obtained from the material tests, showing the dependence of the response on the temperature and maximum strain. The bulk compression modulus is represented by the slope of the graph of the applied pressure versus the strain. The bulk compression tests were cyclically conducted at several maximum pressures and a range of temperatures from -4°F to 68°F. As can be seen in Figure 5.1 the stiffness from the volumetric stress-strain curves was virtually the same over the range of temperatures. Another observation that can be made, is that bulk compression shows minimal hysteretic behavior. Finally, it can be seen that the bulk modulus is almost linear over the pressures of interest, as steel-laminated elastomeric bearings are typically not designed for axial pressures of more than two to three ksi (Stanton, Roeder et al. 2008).

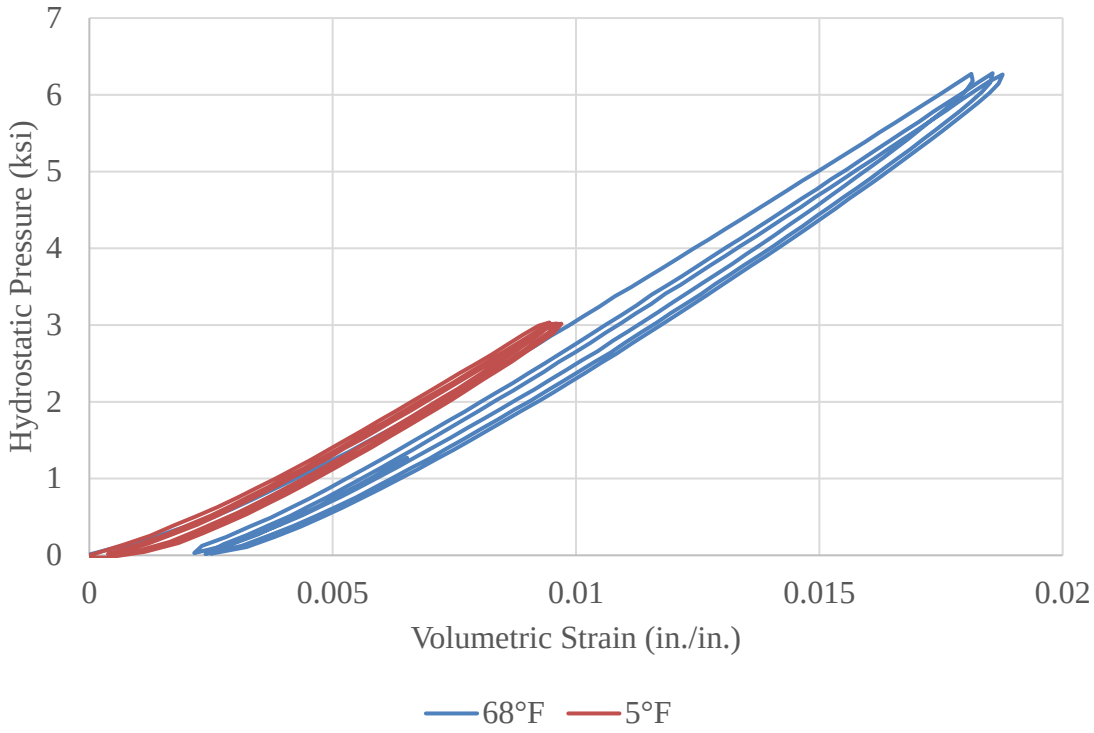

Figure 5.1: Typical volumetric stress-strain test curve for 68°F and 5°F

Figure 5.2 illustrates shear stress-strain results for neoprene rubber under various temperatures for a maximum shear strain of approximately 0.5 in./in. The graphs show that the elastomer stiffness tends to increase with decreasing temperature. While there is a relatively small effect in the temperature of the curves for 68°F and 32°F, the stiffening effect is much more significant as the temperature is reduced below 32°F, which is the freezing temperature of water. In addition, when comparing the curves for various cycles of loading at a given temperature, the stress softening effect (i.e., the stiffer behavior during the first cycle and the softer behavior in subsequent cycles) can be observed more

prominently at lower temperatures. Lastly, the hysteresis tends to increase with decreasing temperature.

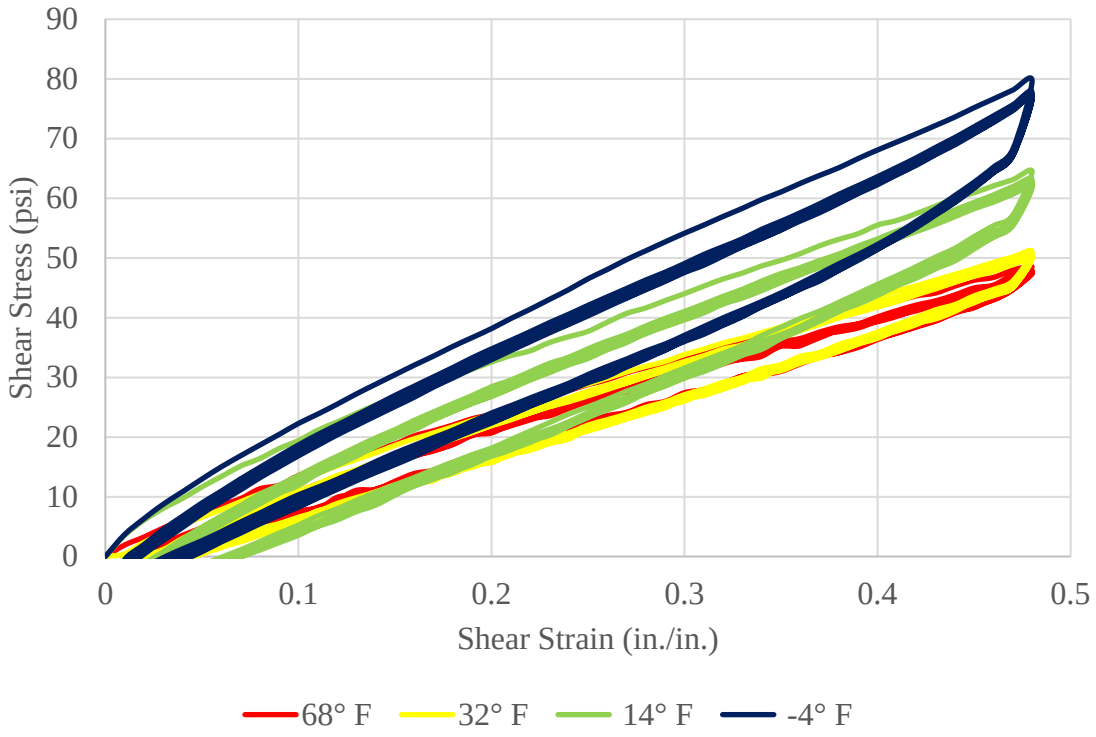

Figure 5.2: Rubber Shear Tests under various temperatures

The behavior seen and described previously as a result of a series of experimental tests, is related to the instantaneous behavior (i.e., the rubber was not conditioned at the test temperature for more than one hour) of neoprene at different temperatures. The results are presented in the following subsections. Subsequently, best fit regressions are proposed for each of the material coefficients for each model. Again, it must be stressed that the values provided are produced from instantaneous material response to temperature change.

5.2.2 HYPERELASTIC MATERIAL COEFFICIENTS WITHOUT HYSTERESIS

The optimized temperature-dependent hyperelastic material coefficients for each temperature, model, and the corresponding values of the Coefficient of Determination, R^2, for the individual temperature and the regressed values are presented respectively in Table 5.1 and Table 5.2 for the Yeoh and the Neo-Hookean material models, described in Chapter 2. The coefficients C_i and D_i are material parameters for the respective hyperelastic material models.

Table 5.1: Optimized material coefficients for each temperature (Yeoh)

Temp (°F)	**C10 (psi)**	**C20 (psi)**	**C30 (psi)**	**D1 (psi^{-1})**	**D2 (psi^{-1})**	**D3 (psi^{-1})**	**R^2**	**R^2 (reg.)**
68	61.65	-56.15	88.69	6.70E-06	3.00E-08	3.00E-09	1.000	0.998
59	64.75	-60.66	98.38	6.70E-06	3.00E-08	3.00E-09	1.000	0.996
50	66.51	-65.76	103.29	6.70E-06	3.00E-08	3.00E-09	0.999	0.998
41	68.36	-69.83	109.01	6.70E-06	3.00E-08	3.00E-09	0.999	0.998
32	67.29	-78.25	131.84	6.70E-06	3.00E-08	3.00E-09	0.997	0.96
23	75.55	-80.62	142.76	6.70E-06	3.00E-08	3.00E-09	1.000	0.997
14	90.94	-100.88	156.03	6.70E-06	3.00E-08	3.00E-09	0.999	0.985
5	95.11	-108.68	197.35	6.70E-06	3.00E-08	3.00E-09	0.999	0.996
-4	100.1	-113.92	207.81	6.70E-06	3.00E-08	3.00E-09	1.000	0.996

Table 5.2: Optimized material coefficients for each temperature (Neo-Hookean)

Temp (°F)	C10	D1	R^2	R^2 (reg.)
68	52.34	6.35E-06	0.986	0.984
59	54.32	6.35E-06	0.986	0.981
50	54.35	6.35E-06	0.992	0.991
41	56.45	6.35E-06	0.977	0.976
32	53.41	6.35E-06	0.991	0.965
23	61.45	6.35E-06	0.985	0.985
14	73.66	6.35E-06	0.973	0.954
5	77.52	6.35E-06	0.983	0.977
-4	81.75	6.35E-06	0.983	0.982

The regressed values are presented in Table 5.3. A representative graph of the test data versus resulting simulations, generated by the regressed parameters is depicted in Figure 5.3. As can be seen, there is reasonable agreement between the test and both material models. The Yeoh model was expected to have a better fit, due to the existence of the higher order terms, as discussed in Chapter 2.

Table 5.3: Regression expressions for hyperelastic material coefficients

Yeoh Model	
C10	$0.008T^2 - 1.0683T + 98.406$
C20	$-0.0066T^2 + 1.2651T - 111.85$
C30	$0.0184T^2 - 2.8707T + 200.25$
Neo-Hookean Model	
C10	$0.0078T^2 - 0.9242T + 80.242$

The regressed parameters, were expected to have a smaller fitness value than the individual datasets. The R^2 values in all cases remained above 0.95 which was deemed a satisfactory fit. For the case of the volumetric coefficients, *Di*, it can be seen that fixed values are proposed for the range of temperatures under consideration, as a result of the temperature-independent volumetric compression behavior.

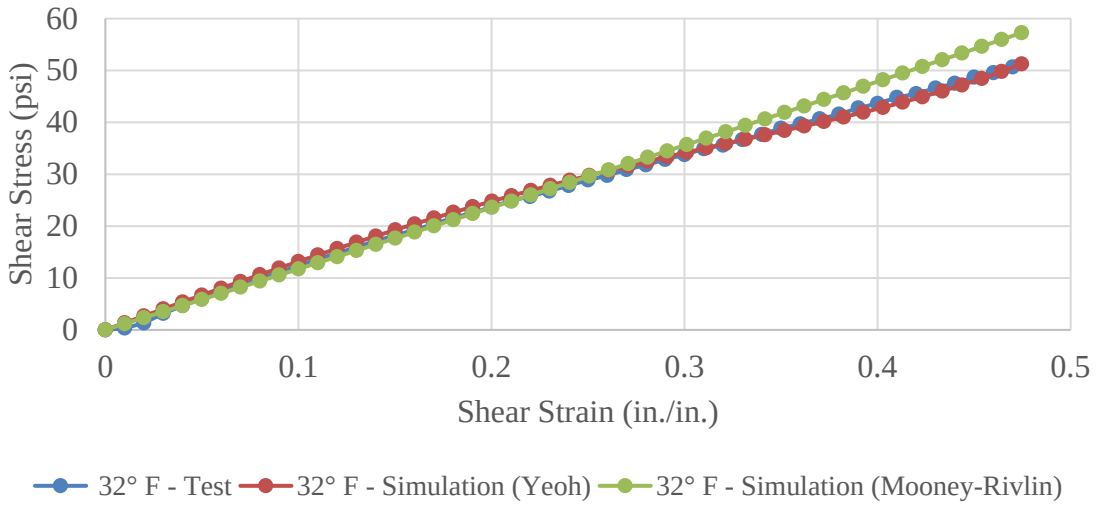

Figure 5.3: Tested and simulated stress-strain curves at 32 °F

5.2.3 HYPERELASTIC MATERIAL COEFFICIENTS WITH HYSTERESIS

Currently, only the general purpose finite element program ABAQUS (Dassault-Systèmes 2012) comes with a predefined material model that allows for including hysteretic behavior. The optimized values and respective regressed expressions for the coefficients of the Yeoh model describing a hyperelastic material with hysteretic behavior are presented in Table 5.4 and Table 5.5. As can be seen, the optimized cases and the cases

coming from the regressed values show an R^2 value very close to unity. Such an agreement is illustrated in Figure 5.4. As shown previously, the bulk behavior can be assumed to have no hysteretic behavior.

Table 5.4: Optimized material coefficients for each temperature (Yeoh - Hysteresis)

Temp (°F)	C10 (psi)	C20 (psi)	C30 (psi)	S	A	m	C	E	R^2	R^2 (reg.)
68	56.81	-52.10	106.0	3.58	3.42E-05	8.07	-0.49	0.035	0.998	0.976
59	59.58	-51.99	106.0	3.02	1.09E-04	7.86	-0.51	0.018	0.998	0.982
50	55.98	-48.25	115.9	5.41	4.18E-06	7.43	-0.50	0.0082	0.995	0.989
41	58.44	-49.85	101.6	6.02	9.69E-07	8.08	-0.36	0.00034	0.998	0.984
32	56.56	-48.20	93.4	5.51	1.68E-05	6.84	-0.46	0.0010	0.997	0.912
23	65.17	-51.58	98.9	6.31	4.46E-05	4.75	-0.69	0.0016	0.998	0.982
14	73.59	-50.54	89.1	6.49	6.81E-07	6.19	-0.54	2.07E-04	0.997	0.988
5	77.59	-50.78	96.8	4.47	4.26E-06	5.08	-0.61	7.25E-05	0.999	0.99
-4	80.96	-50.17	94.4	1.79	5.90E-05	3.61	-0.72	4.61E-11	0.999	0.988

Table 5.5: Regression expressions for hyperelastic material coefficients

Yeoh Model	
C10	$-0.3566T + 76.376$
C20	$-0.0094T - 50.084$
C30	$0.2415T + 92.531$
S	$-0.0028T^2 + 0.1823T + 3.3398$
A	$3E-07T + 2E-05$
m	$-0.0006T^2 + 0.0989T + 4.2391$
C	$0.003T - 0.6392$
E	$2E-05T + 0.0002$

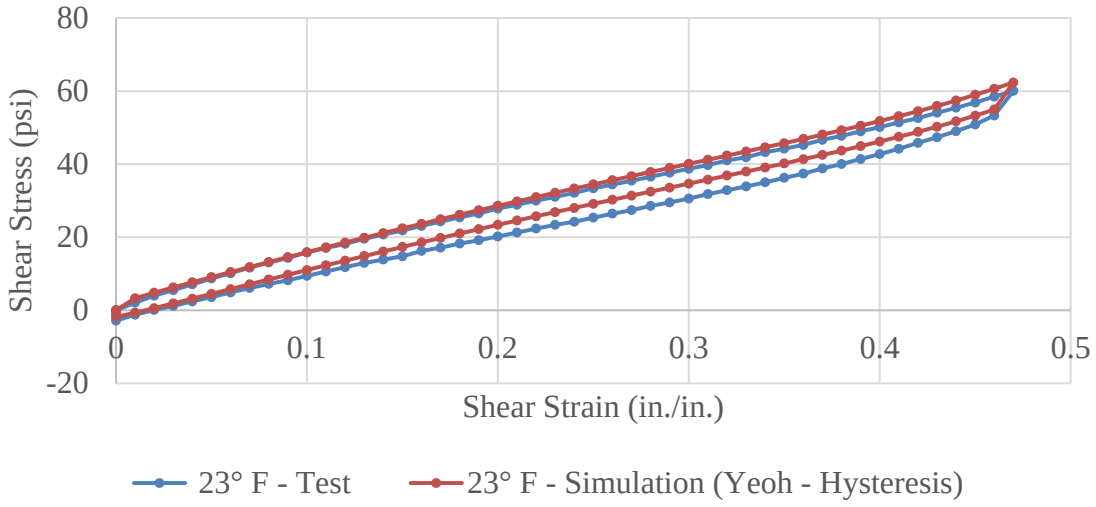

Figure 5.4: Tested and simulated stress-strain curves at 23 °F

5.3 Full Scale Compression Test Results

5.3.1 STIFFNESS RESULTS

This section provides the stiffness results of the tested specimens in comparison with the AASHTO predictions. Figure 5.5-Figure 5.8 illustrate the load-deflection curves of the specimens in comparison with the AASHTO predictions. The naming protocol for the experimental curves shown herein consists of two letters and a number. The first letter refers to the bearing size, (XL) for the extra-large (L) for the large, (M) for the medium, and (S) for the small bearings. The second letter corresponds to the deformation mode of interest, (C) for compression, and the number is a counter of the tests on identical specified bearing geometries. The upper limit as defined by the AASHTO Method A is also indicated by the dashed line.

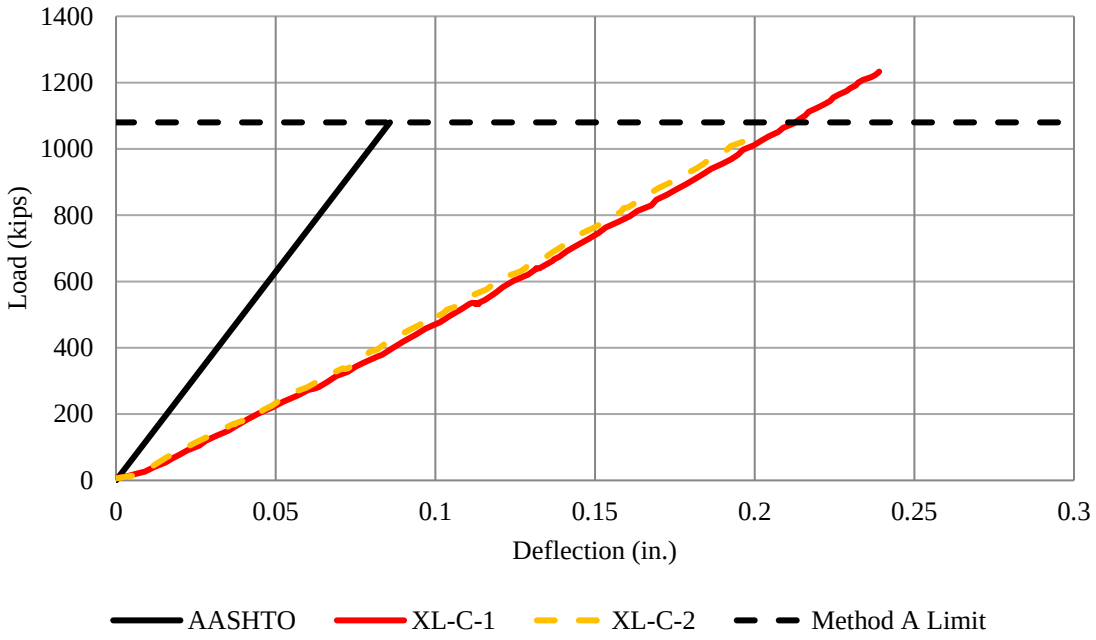

Figure 5.5: Load-deflection curves for extra-large (L) bearings under compression

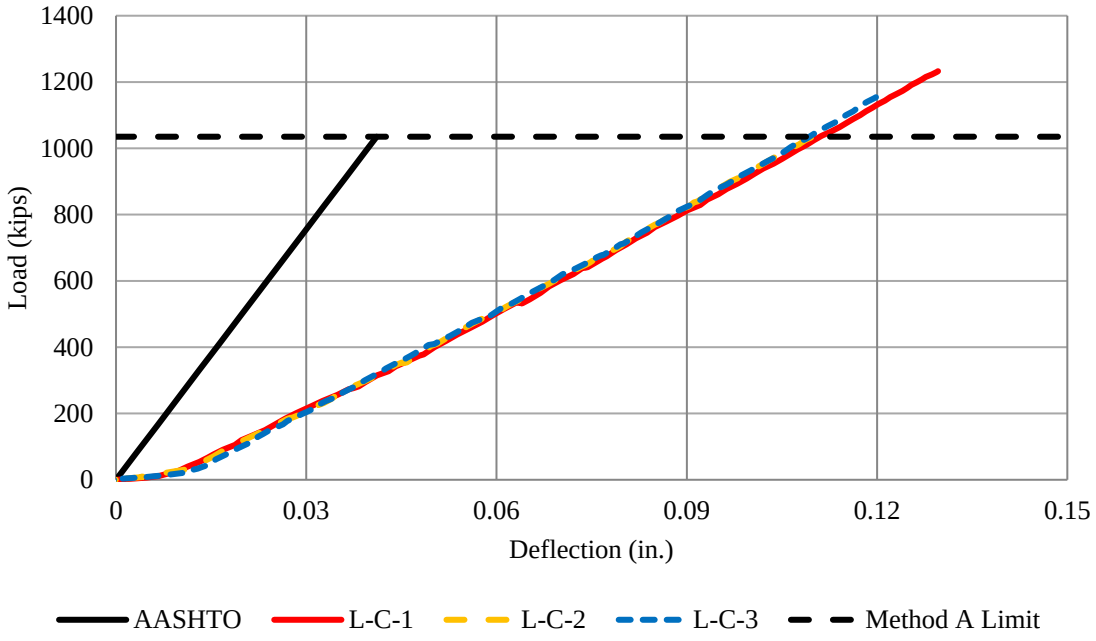

Figure 5.6: Load-deflection curves for large (L) bearings under compression

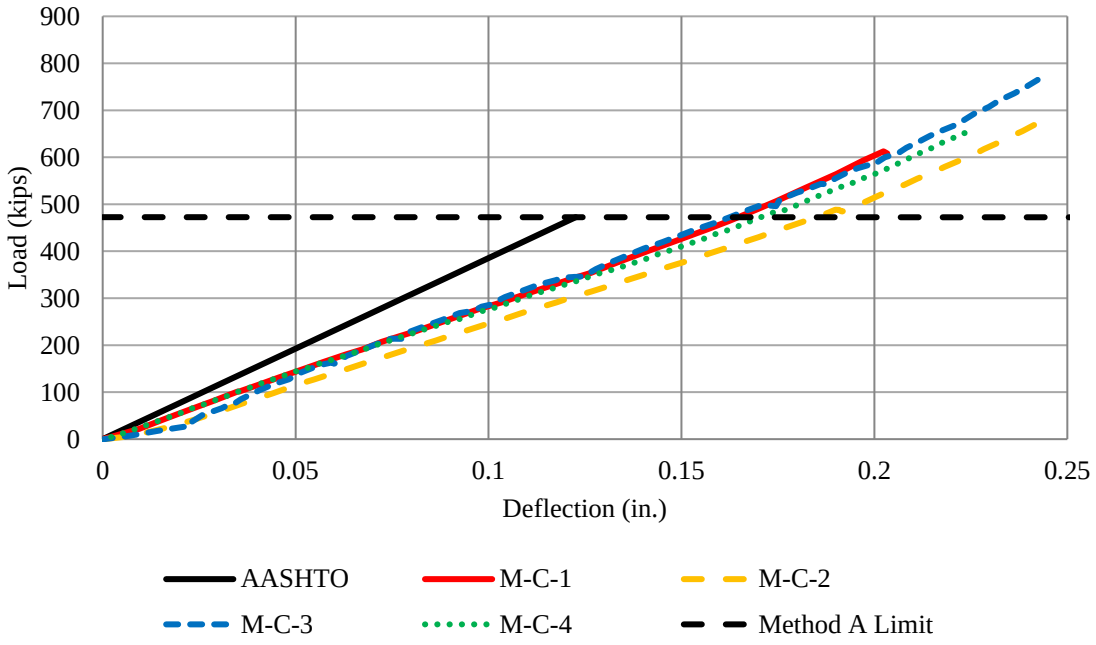

Figure 5.7: Load-deflection curves for medium (M) bearings under compression

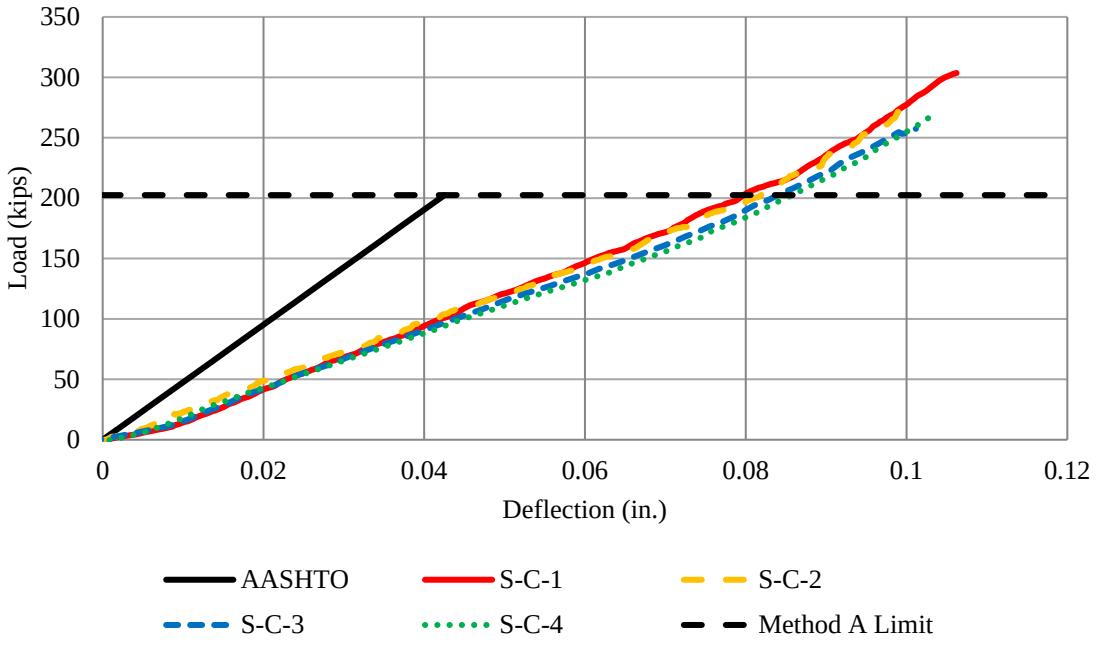

Figure 5.8: Load-deflection curves for small (S) bearings under compression

The graphs of the test results show that there is very little variation in the response of a bearing to axial loading for bearings of the same dimensions and properties, suggesting limited variability in the material properties. However, the discrepancy between the experimental results and AASHTO predictions suggest that there might be parameters, on average equivalent, affecting the axial stiffness in a way that is not captured by the current design provisions.

It also can be seen that AASHTO significantly overestimates the axial stiffness of all bearings tested in this experimental series. This can be a result of the inherent approximations of simplified equations provided, as well as the assumption of perfect bond of the rubber to the contact surface. In order to quantify the differences in stiffness, the results are presented in terms of axial stiffness using a linear regression of the test results. Figure 5.9-Figure 5.12 depict the tested and calculated stiffness values.

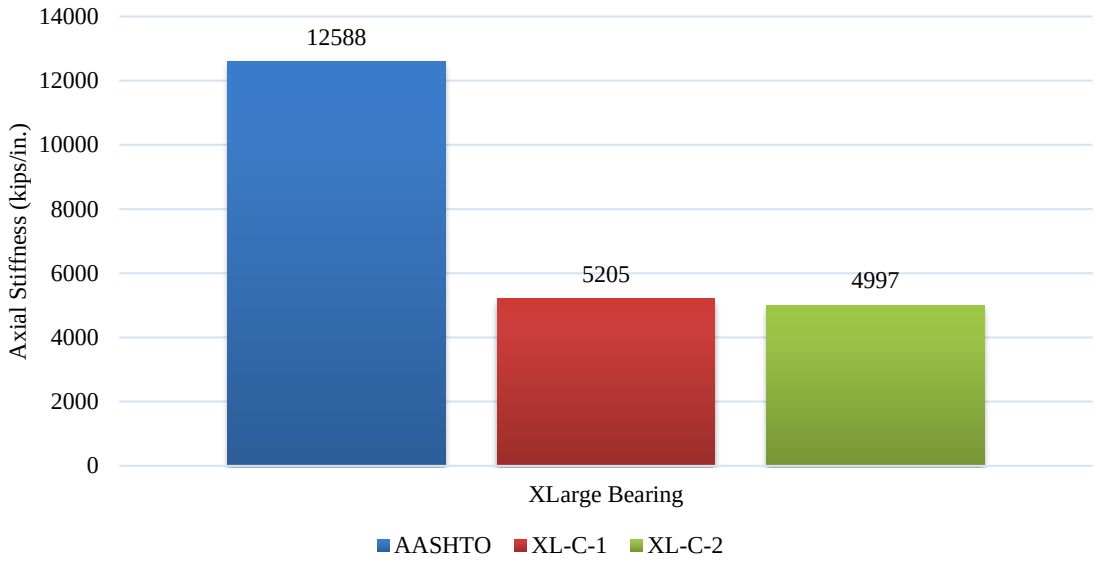

Figure 5.9: Axial stiffness values for extra-large (XL) bearings

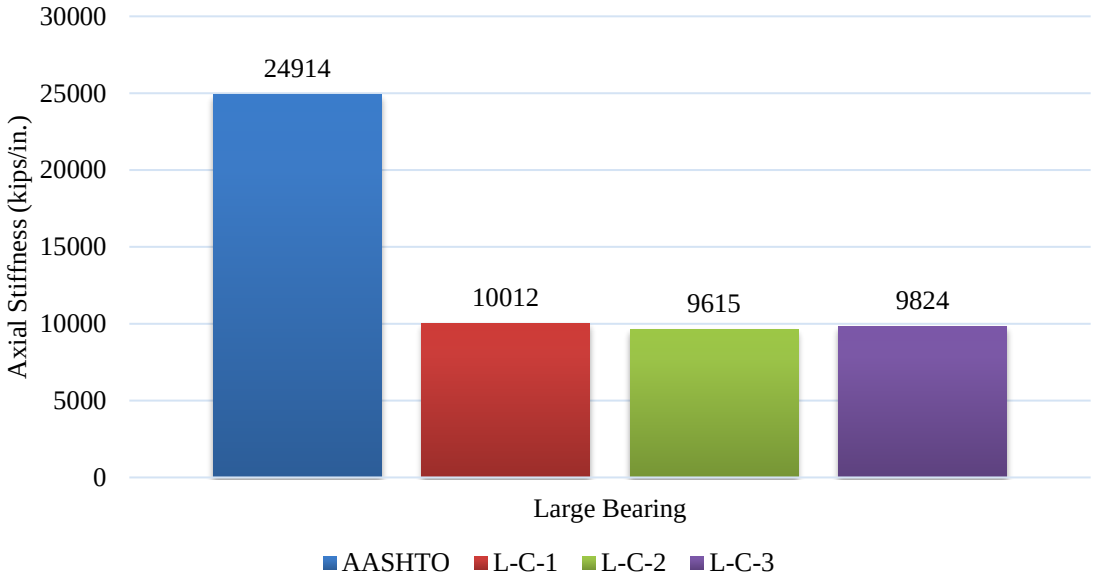

Figure 5.10: Axial stiffness values for large (L) bearings

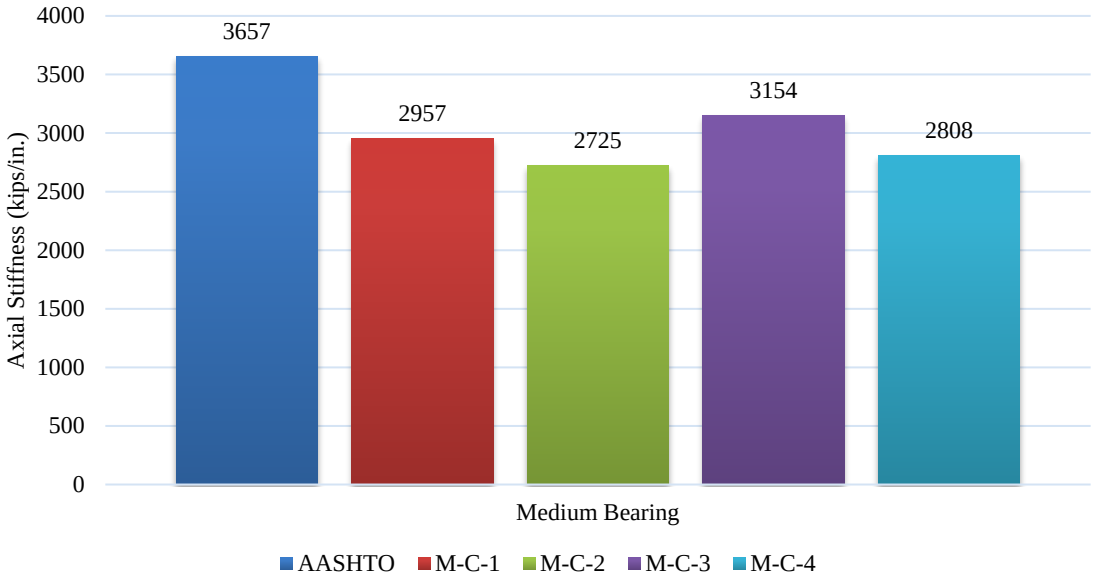

Figure 5.11: Axial stiffness values for medium (M) bearings

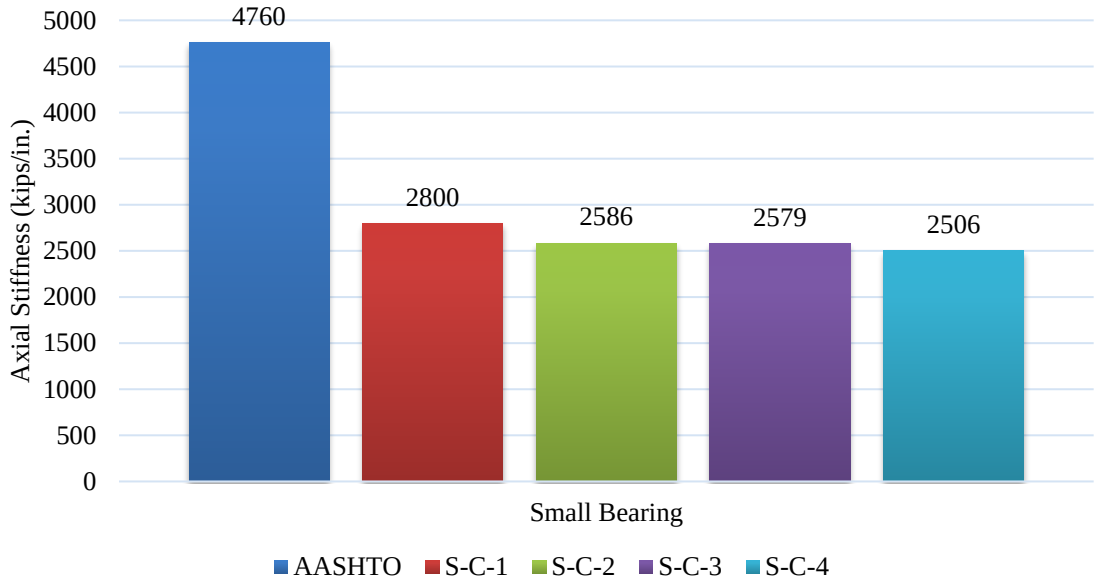

Figure 5.12: Axial stiffness values for small (S) bearings

In general, there is no clear over-prediction relation that can be directly related to the plan area or the shape factor of the bearing. However, the comparison of the AASHTO predictions with the medium sized bearing provides an indication that results and discrepancies can be case-dependent.

5.3.2 TEST OBSERVATIONS

The primary focus of this portion of the study was to measure the axial stiffness of bearings with a range of geometries. The compression testing provided a good means of inspecting the location of the steel laminates close to the surface of the bearing by observing where the bulging occurs. The results indicate that the steel laminates were placed at approximately the locations specified for the finished product, though one bearing had a layer thickness that was not uniform along its length, creating a differential bulging

in this area. Figure 5.14a-b depicts the observed bulging for the two different cases. Figure 5.13 illustrates the section cut of the Bearing (L) demonstrating imperfections in the shim plates and corresponding elastomer layers across the width of the bearing. Note that the cut was done along the short edge of the bearing due to dimensional limitations in the saw capabilities. Consequently, the relative misalignment and imperfection (curved shape) of the laminate, and thickness variations between layers will likely have an impact on the behavior of the bearing. The impact could be a “softer” bearing. These hypotheses, were investigated in the numerical portion of this dissertation.

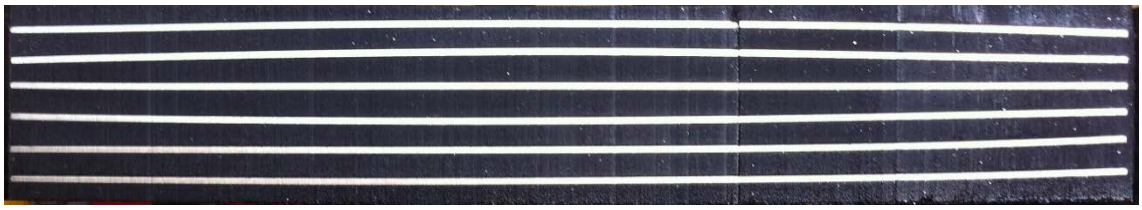

Figure 5.13: Bearing (L) section cut

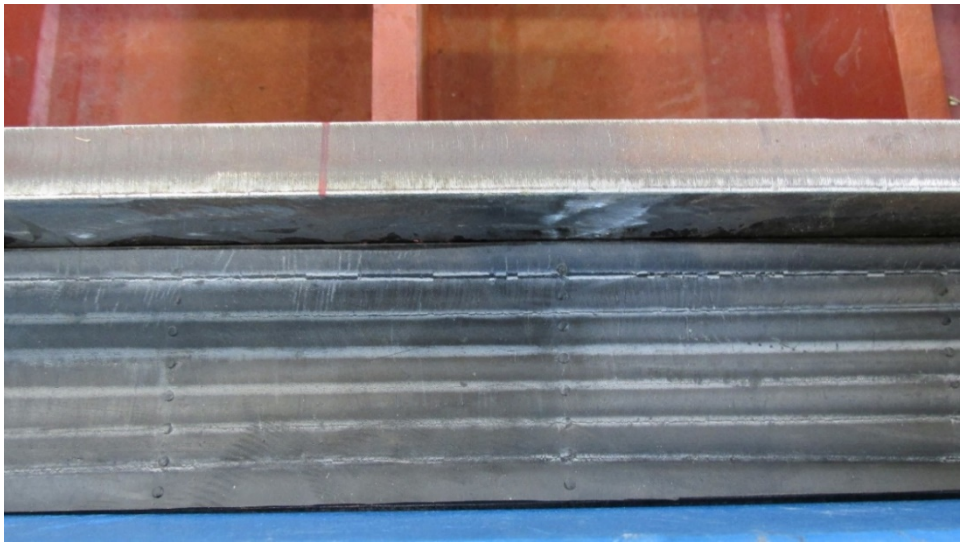

(a)

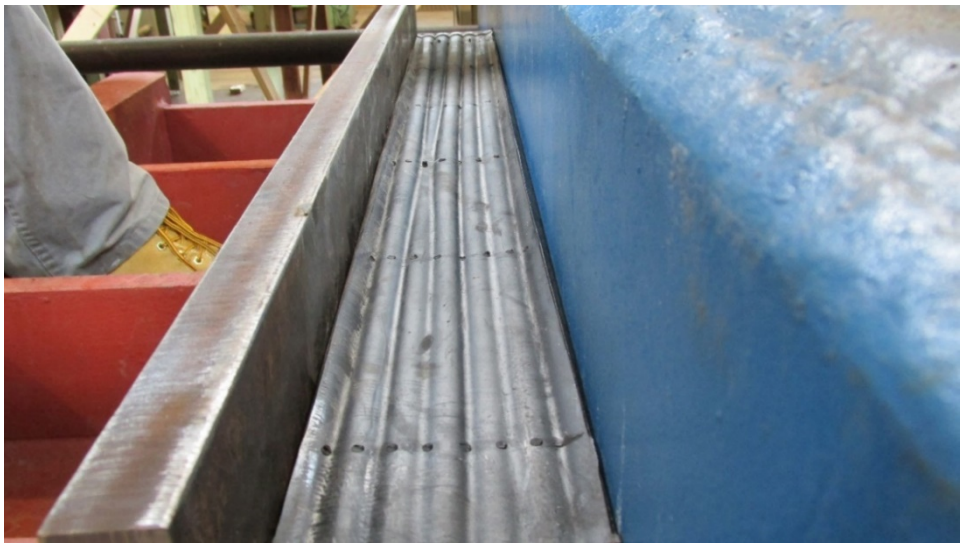

(b)

Figure 5.14: Uniform layer thickness along the bearing length (a), and non-uniform layer thickness along the bearing length (b)

5.4 Full Scale Shear Test Results

5.4.1 STIFFNESS RESULTS

This section is focused on representative data obtained from the shear tests conducted. Bearing XL was not tested in shear in order not to risk the integrity of the test setup, which was severely damaged during testing on Bearing M. Figure 5.15 illustrates the force-displacement curves from the full-scale tests for Bearing S with the idealized linear curves (20%-40% method described in Chapter 3) corresponding to the average, maximum, and minimum shear stiffness obtained from the material level tests. As can be seen, the overall shear stiffness behavior can determined with reasonable accuracy from the material level testing for this bearing configuration.

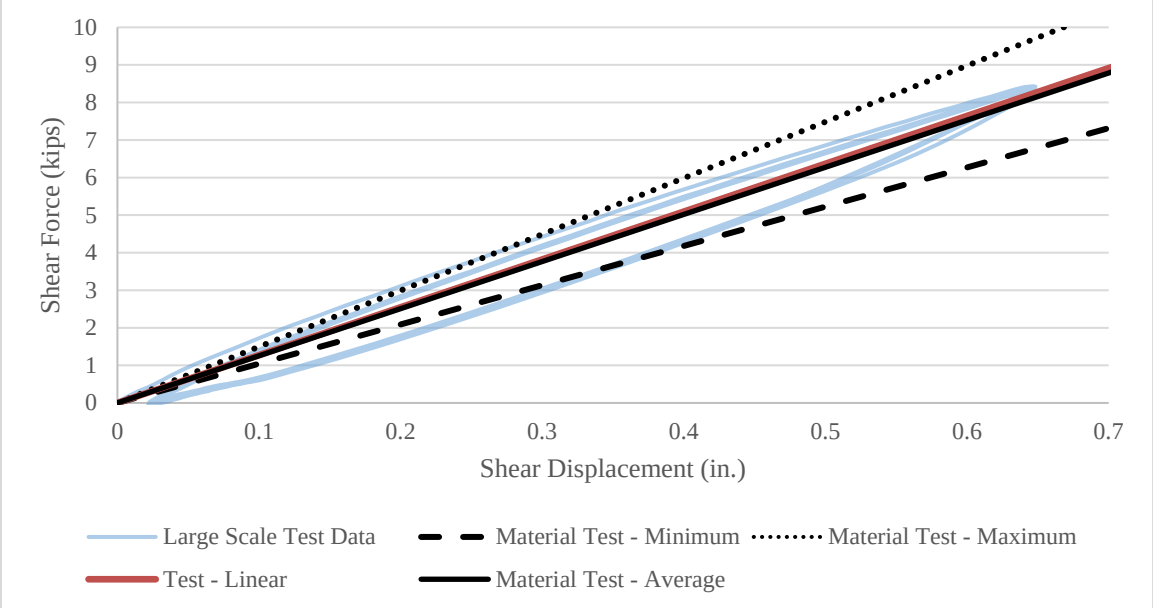

Figure 5.15: Full Scale Test-Material stiffness correlation (S)

Figure 5.16 shows the force-displacement (equivalent to stress-strain) curves for the 50% shear strain series (~0.625 in.) under varying axial loads on Bearing S. Similar curves were generated for the other bearing sizes. Consistent with the literature described in Chapter 2, the shear stiffness for Bearing S was found not to be dependent on the axial pressure applied for this elastomeric bearing geometry, for the axial pressure levels commonly occurring in practice (0.5 – 2.0 ksi). To better illustrate the results, the shear stiffness for each case was calculated according to the procedure described in previous sections and is shown in Figure 5.17. As can be seen, the variability of the shear stiffness is minimal, which can be reflected in the coefficient of variation (CV) of 0.015.

Consistent with findings from Bearing S, the bearing having almost equal length to height ratio, Bearing L, showed no significant variability in shear stiffness with axial pressure, illustrated in Figure 5.18. Bearing XL was not tested in shear in order not to risk the integrity of the test setup, which was severely damaged during testing on Bearing M.

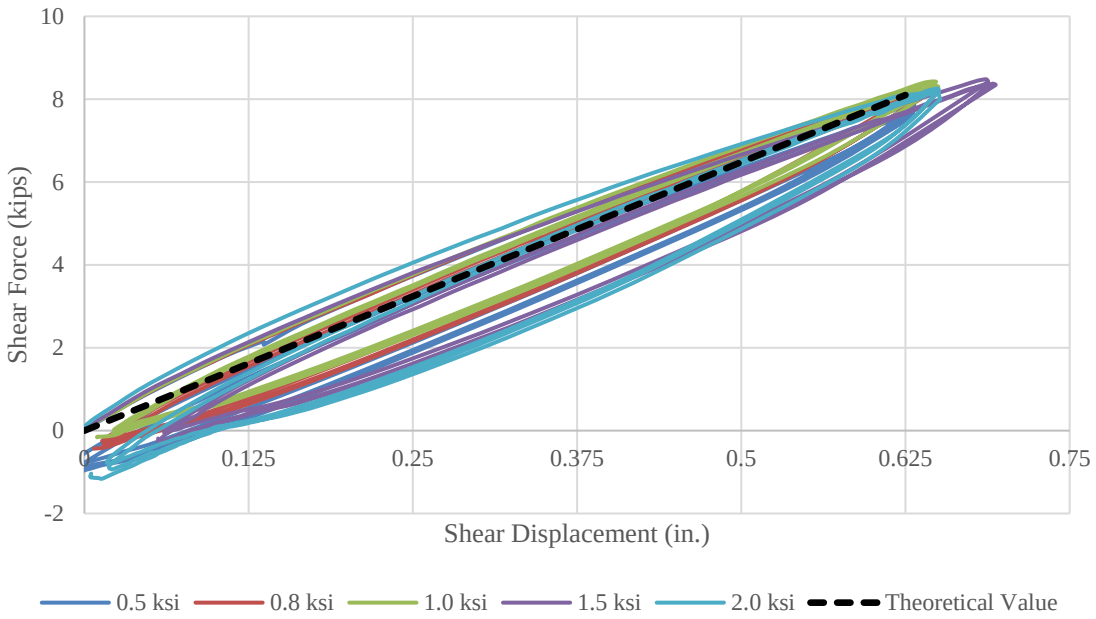

Figure 5.16: Force - displacement curves of the small bearing at different axial loads (S)

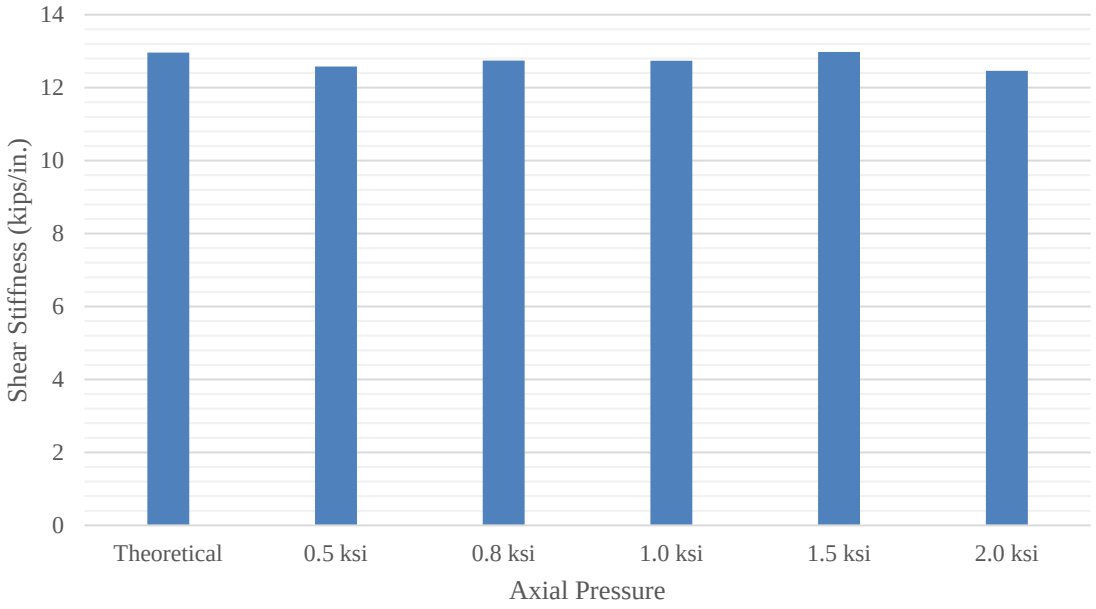

Figure 5.17: Calculated shear stiffness at different axial loads (S)

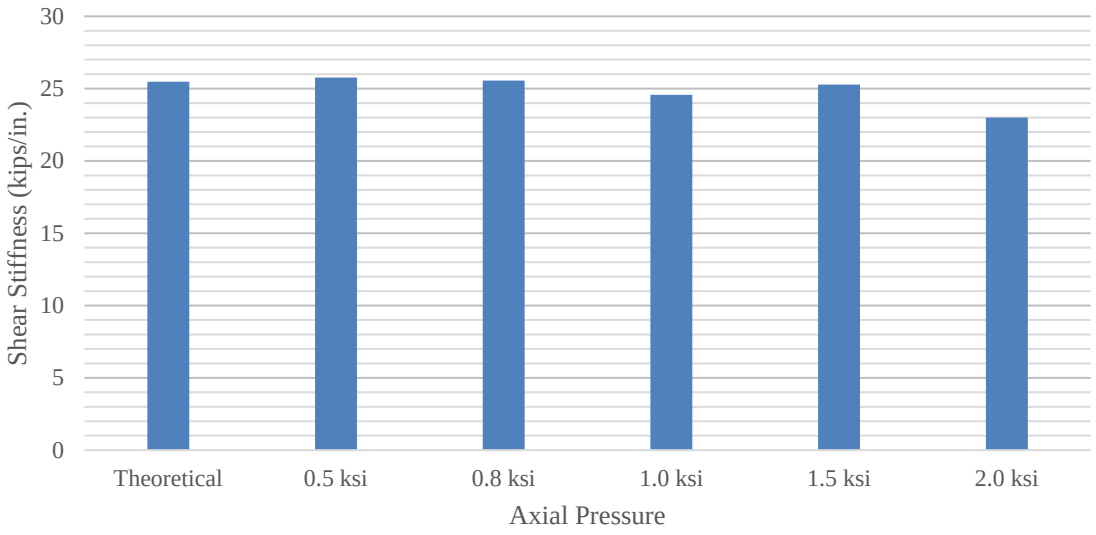

Figure 5.18: Calculated shear stiffness at different axial loads (L)

Although Bearings S and L showed no variability in shear stiffness at tested axial stress levels, Bearing M exhibited a different behavior. Figure 5.19 depicts the force displacement curves at various axial stress levels for Bearing M. Figure 5.20 presents the decrease in shear stiffness with increasing axial stress. This is a sign that the bearing is losing shear stiffness at higher axial stress levels. The results suggest that the assumed (AASHTO 2012) state of the simple shear may not be valid for all bearing configurations and loading cases. This phenomenon is numerically investigated in the numerical portion of this dissertation, and results are presented in Chapter 6.

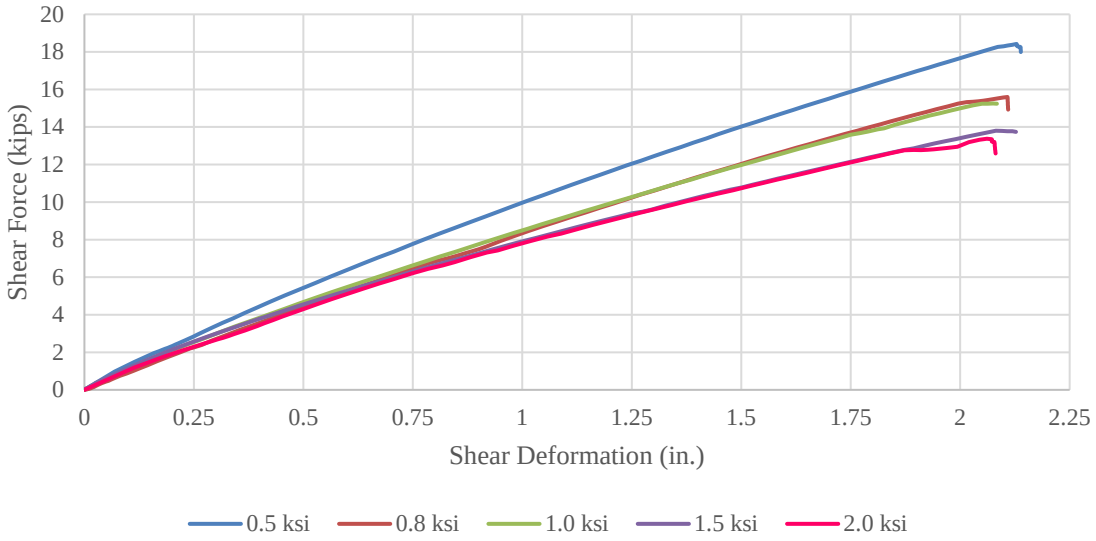

Figure 5.19: Force-Displacement curves (M)

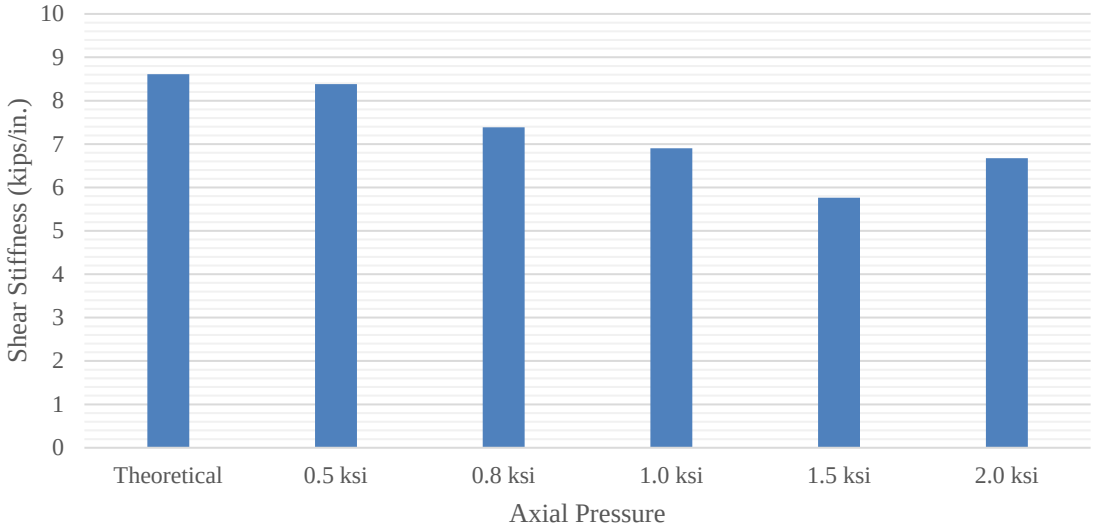

Figure 5.20: Calculated shear stiffness at different axial loads (M)

5.4.2 DIRECTIONAL STIFFNESS RESULTS

Bearings used in higher-demand applications are more likely to be used in bridges with skewed supports and/or horizontal curvature. In these applications, the bearings will likely experience shearing deformations in more than one direction. Although this issue has been investigated numerically proposing no shear-direction dependence (Nguyen and Tassoulas 2010) on the shear stiffness, no experimental results supporting these numerical findings existed prior to this study. Bearings M and L were only tested in the directional stiffness test series. Bearing S was excluded due to the almost equal length to height ratio with Bearing L.

Figure 5.21 illustrates experimental results from tests conducted at FSEL along with the AASHTO prediction. The assumed independence of the shear stiffness (theoretical simple shear stiffness) from the shearing direction is confirmed for this bearing. In order to better illustrate the change in shear stiffness with respect to the shear direction, normalized results to shear stiffness at 0° are shown in Figure 5.22.

Data discrepancy between predictions and measured values can be attributed to various parameters such as the stiffness calculation method, described in Chapter 3, instrumentation errors, and inherent test setup errors. The value of 90° for bearing L was not possible to be assessed due to geometrical constraints of the test setup.

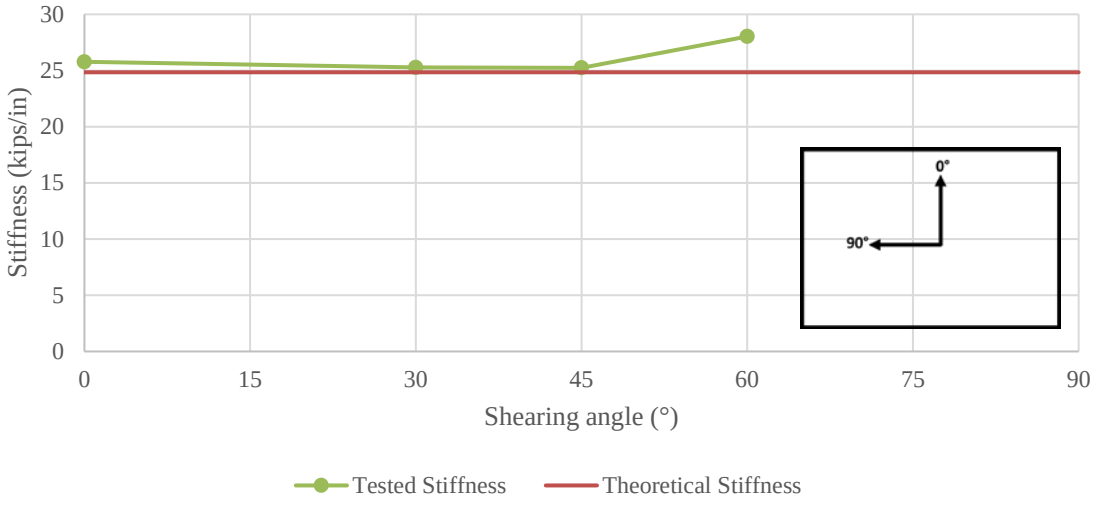

Figure 5.21: Effect of shear direction on shear stiffness (L)

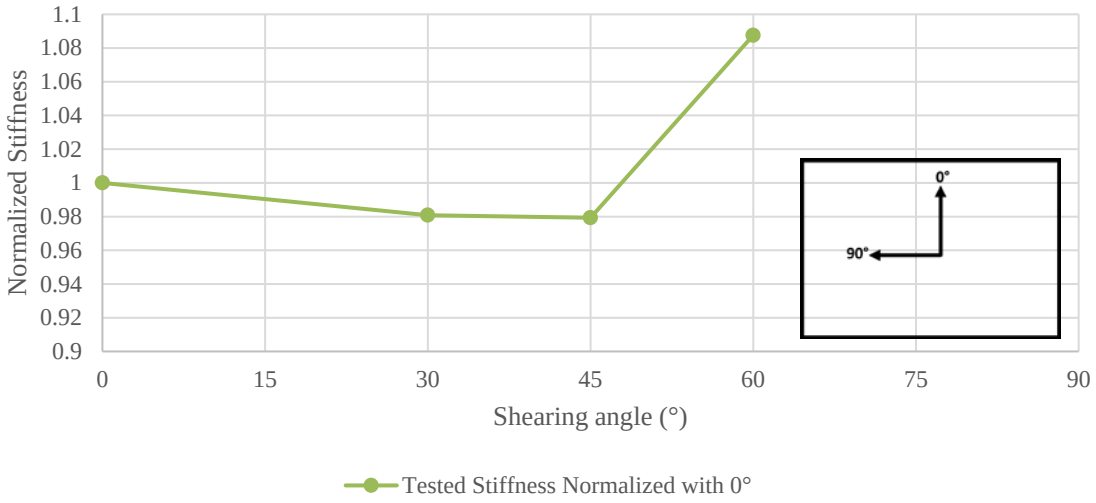

Figure 5.22: Effect of shear direction (normalized) on shear stiffness (L)

Although the findings were consistent with previous numerical studies, this research study expanded the tests to higher shape factors and aspect ratios. As a result, Bearing M was also tested for assessing the effects of shear directionality. As illustrated in

Figure 5.23 and Figure 5.24 for Bearing M, and for an axial pressure of 1200 psi the shear stiffness increases with a tendency to approach the theoretical solution as the shearing direction approaches 90°, exceeding the theoretical value at a testing angle of 90°. In this case, although conservative and safe to be neglected from a slipping standpoint, the change in shear stiffness with respect to the shear direction is not negligible, reaching approximately 45%. This phenomenon is also numerically investigated in the numerical portion of this dissertation, and results are presented in Chapter 6.

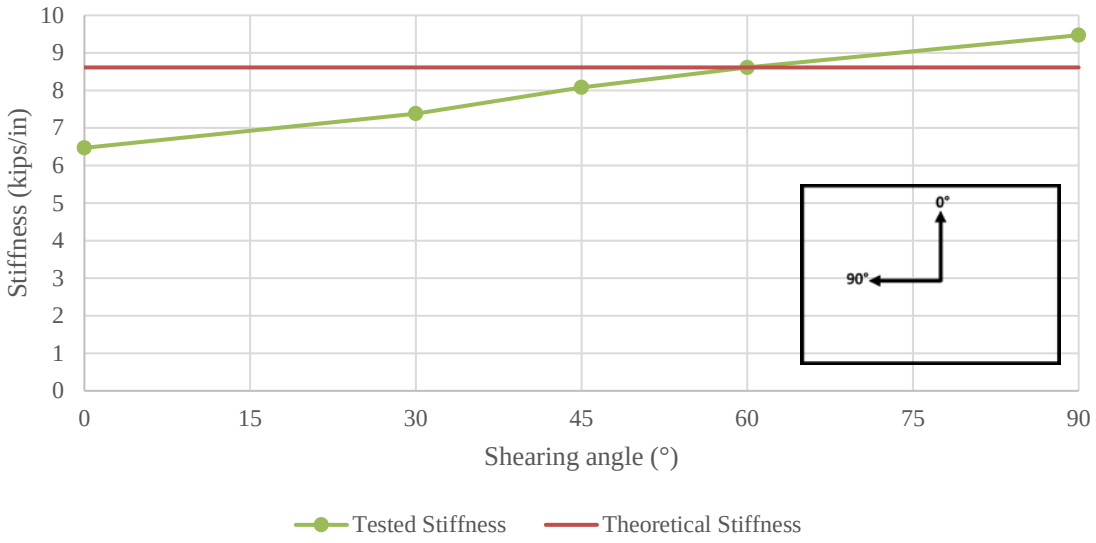

Figure 5.23: Effect of shear direction on shear stiffness (M)

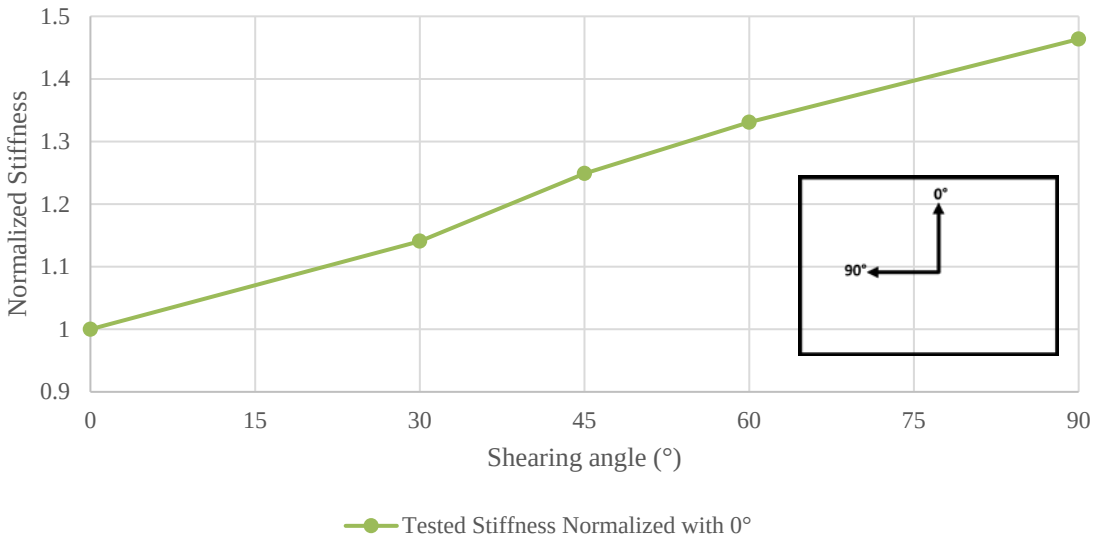

Figure 5.24: Effect of shear direction (normalized) on shear stiffness (M)

5.4.3 TEST OBSERVATIONS

As described in Chapter 2, current AASHTO Method B provisions would limit the axial pressure to 1.0 ksi to limit excessive bulging, more noticeable in bearings with low shape factors (S<10). In addition, any AASHTO method would limit the shear strain due to elastomer shearing to 50%. Bearing M (S = 9.22) at a combination of 1.5 ksi axial pressure and 75% shear strain showed no excessive bulging or rollover as can be seen in Figure 5.25. The phenomenon of rollover (seen on Bearing S in Figure 5.26) is defined as the loss of contact of portion of the bearing surface due the bearing shearing. A similar phenomenon was noticed in Bearing L (Figure 5.27). The disadvantages of the rollover effect are that it reduces the effective area of the bearing and thus increases the effective stress, making it more prone to buckling, and increases the potential of bending the edge of the steel laminates inside the bearing. As a result, high stresses and strains concentrate

in that region and can be associated with an increased potential of distress initiation. It is worth noting that the bearings were inspected after all tests and there were no visible signs of distress in any of the bearings.

Figure 5.25: Bearing M under 1.5 ksi axial load and 75% shear strain

Figure 5.26: Rollover effect on lower portion of bearing S

Figure 5.27: Bearing L under 2.0 ksi axial load and 100% shear strain

Finally, as stability is one of the failure modes a designer must consider, Bearing M was pushed to the point of instability. Due to the larger total rubber thickness, Bearing

M was the bearing most prone to buckling. The bearing was tested to 2.0 ksi axial stress and the target shear strain was placed at 100%, a loading condition exceeding AASHTO limits. Despite the fact that the target shear strain was reached, the bearing was considered to have failed as the loss of axial stiffness (buckling) led to excessive axial deformations, resulting in damage to the test setup. In order to avoid any further damage in the shear test setup the axial load was immediately decreased, allowing for pictures only at the unloading phase. Bearing M can still be seen in the buckled configuration in Figure 5.28. It can be noticed that the excessive axial load caused the top layer of the elastomer to “flow” out at the edges. This phenomenon is less prominent at the concrete-elastomer interface due to increased friction at this location. After unloading, the bond was checked at this location and no signs of debonding were observed at the cover layer.

Figure 5.28: Buckled bearing M

5.5 Full scale rotational test results

5.5.1 COMBINED COMPRESSION AND ROTATION RESULTS

This section provides representative data from tests conducted and describes the main conclusions that were drawn from this portion of the study. As previously discussed, the purpose of this test series was to evaluate the consequences of lift-off, evaluate the validity of the total shear strain approach for calculating the strength limits of a bearing, and use this test as means of validating the concurrent FEA studies (Han 2016). As described in Chapter 3, Bearings S and XL were not tested due to geometrical constraints of the test setup and to minimize the risks of damaging the test setup.

Figure 5.30 shows representative data from a combined compression and rotation test. Regarding the lift-off phenomenon, as expected, the absence of contact between the steel plate and the bearing only happened at lower axial loads, as depicted in Figure 5.29. As a result, the test data chart (Figure 5.30) can be divided in two portions, the lift-off portion associated with lower loads, and the full contact portion where the plate is in contact with the totality of the area of the bearing and the measured stiffness is almost identical to the axial stiffness measured in prior portions of this study.

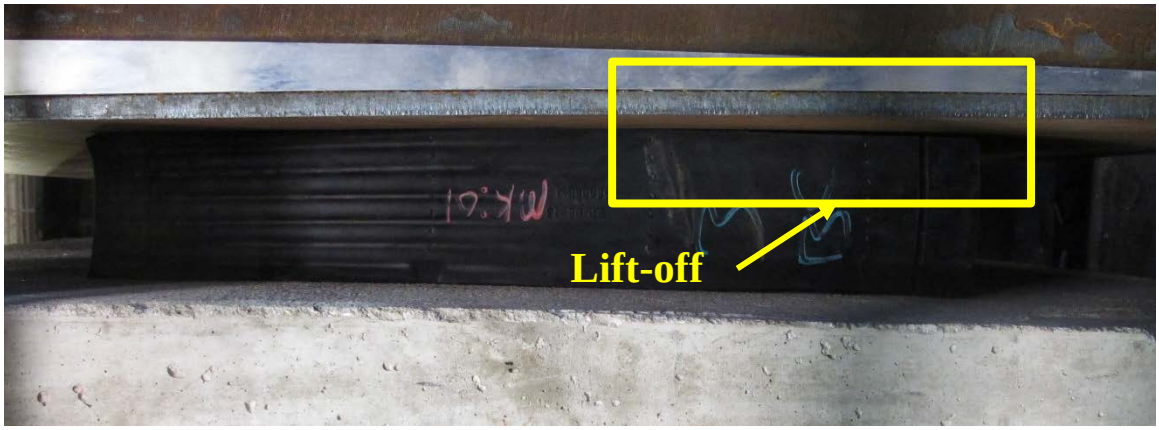

Figure 5.29: Lift-off during combined compression and rotation test

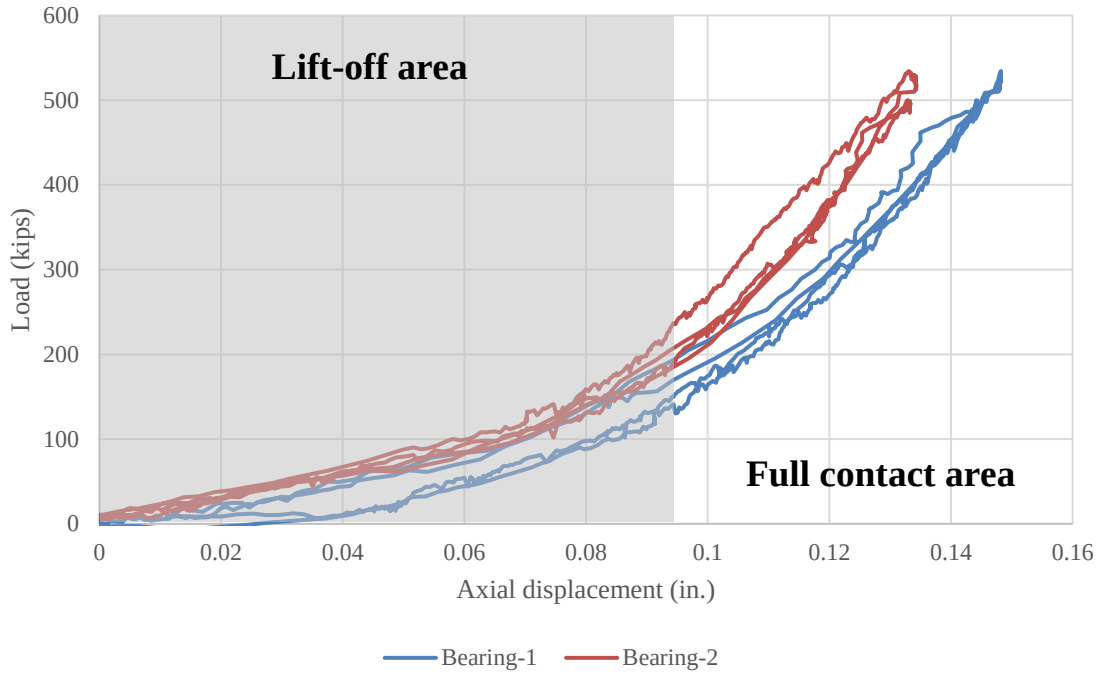

Figure 5.30: Combined compression and rotation test data (Bearing L – θ=0.5°)

In order to evaluate the strength of the bearing, combined compression and rotation tests were conducted at higher axial loads and with larger imposed rotations. According to the AASHTO code, imposing a rotation of 1.5° on Bearing L should fail as a total shear strain of 5.0 would be reached. However, as can be seen in Figure 5.31, Bearing L was able to sustain the aforementioned rotation in addition to a compressive axial load of 800 kips, leading to a total shear strain of approximately 7.0.

Figure 5.31: Bearing L under combined compression and rotation (θ=1.5°)

Finally, as one of the purposes of this portion of the study was to validate the FEA models developed for concurrent research (Han 2016), test data was compared with FEA predictions. As illustrated in Figure 5.32, FEA predicts the loading curves reasonably well. The error between tests and prediction can be attributed to inherent test setup asymmetries, leading to the compression of the one bearing slightly earlier than the other. This fact inevitably offsets the two curves, plotted here without correction. It is obvious to the reader that upon this offset correction, satisfactory correlation would be achieved.

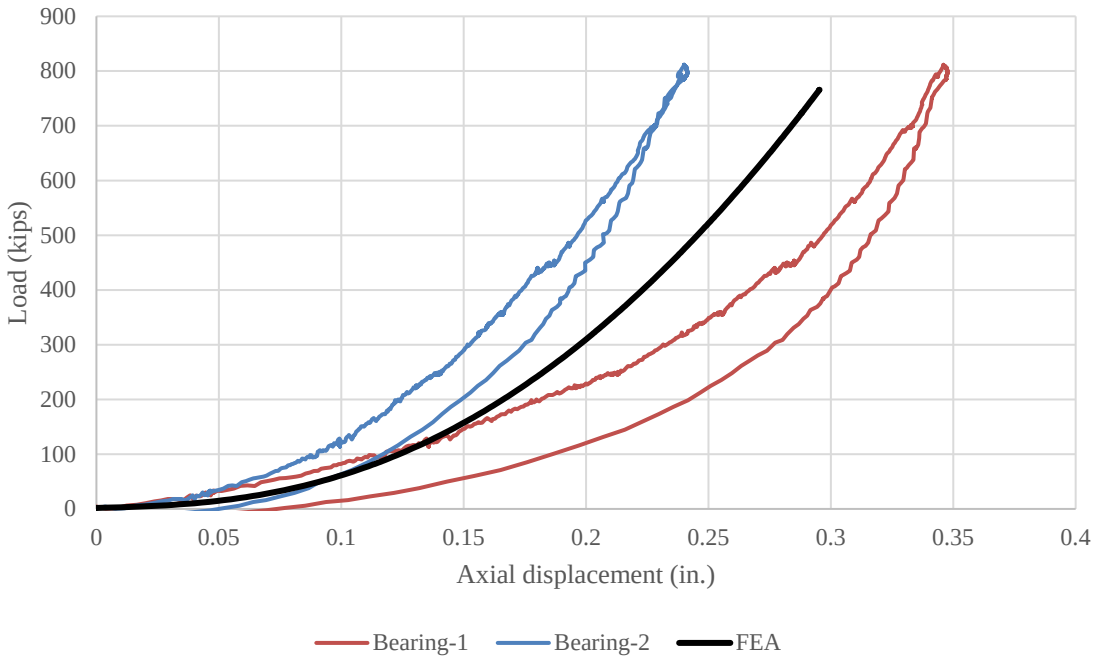

Figure 5.32: Combined compression and rotation test data and FEA prediction (Bearing L – θ=1.5°) (Han 2016)

5.5.2 TEST OBSERVATIONS

No failure was noticed after the application of the maximum service load under both rotation cases despite the large shear strains at the end of the bearing as illustrated in Figure 5.28 and Figure 5.31.

5.6 Summary

An overview of the experimental results was provided in this chapter. The findings were presented from the standpoint of the current steel-laminated bearing design approaches assessment for the use in bridges considered as higher demand applications.

From the material experiments conducted in this study and in Sun (2015), hyperelastic material model coefficients for accurately simulating Durometer 50 Neoprene material under a range of temperatures useful for civil engineering applications were developed. This can help future researchers investigate expected behavior without the need of experimental testing, or to better plan their experimental program.

From the full-scale experiments conducted in this research project there were four major outcomes.

- It has been found that equations predicting the axial deflections of bearings are not necessarily accurate for bearings qualifying for higher demand applications (high shape factors, large plan areas).
- Shear stiffness is dependent on the axial load and the shear direction. This effect was more prominent for taller bearings relative to their plan directions.
- It has been shown that AASHTO Method A and Method B design procedures (Described in Chapter 2) result in safe bearing designs for what could be considered as higher demand applications, with Method A producing larger, uneconomic bearings.

- Lift-off is a phenomenon associated with lower axial loads and thus not an issue when observed rotations are not exceeding the ones predicted.
- Buckling of elastomeric bearings for non-seismic applications can also be an issue as taller bearings are needed to accommodate large temperature bridge movements; however, this issue is successfully addressed by current AASHTO design approaches.

All findings from the experimental portion of this study were used to validate the finite element simulations for model calibration and prediction comparison purposes.

CHAPTER 6: RESULTS – NUMERICAL SIMULATIONS

6.1 Introduction

This chapter presents the results of the numerical simulations performed during this study. The methodology that was followed for these simulations was presented in Chapter 4. This chapter presents the results of approximately 1,400 models that were run to evaluate the influence of several parameters on the axial and shear stiffness of steel-laminated elastomeric bearings.

For studies on factors affecting the axial stiffness of bearings, the following parameters were evaluated:

1. the magnitude of the bending of the steel shims (0% to 75% of the layer thickness out-of-straightness),
2. the error in misalignment of the steel shims (±0 to ±50% of the steel thickness), and
3. the amount of friction (coefficient of friction of 0.2 to 0.5) between the cover layer and the superstructure or substructure.

The impact of these parameters was evaluated for layers of different shape factors (7.5 to 20) and aspect ratios (1.0 to 2.0).

For studies on factors affecting the shear stiffness of bearings, the following parameters were evaluated:

1. the direction at which the shear deformation was applied, and
2. the magnitude of the axial load.

The effect of these parameters was assessed for bearings with different combinations of aspect ratios (1.0 to 2.0) and width to total rubber height ratios (2.5 to 10).

An overview of the results is presented in the following subsections. Due to the multi-variable nature of the parametric study, the influence of each parameter is presented individually. Subsequently, the impact of several combinations of parameters is presented and discussed. Finally, general conclusions are presented.

6.2 Results of Studies on Factors Affecting Axial Stiffness

This section presents results examining how two different imperfection configurations on the steel shims of a steel-laminated elastomeric bearing affect its axial stiffness. As noted above, the two configurations considered were bending of steel shims (see Figure 4.7) and misalignment of steel shims (see Figure 4.8). The effect of simultaneous imperfections on a layer is outside of the scope of this dissertation. In addition, this section presents results examining how the bearing axial stiffness is affected by friction between the top bearing surface and the superstructure, and the bottom bearing surface and the substructure. In this portion of the numerical study, bearings with the minimum number of elastomer layers were simulated to minimize the computational effort required for the simulation to run.

6.2.1 Effect of Shim bending

This section examines the impact of bending of a steel shim on the axial stiffness of a steel-laminated elastomeric bearing. Figure 6.1 illustrates the model that was developed to simulate this mode of imperfection. Since all analyses conducted utilized three-dimensional models, it must be noted that the steel shims are straight in the direction perpendicular to the one shown in the figure.

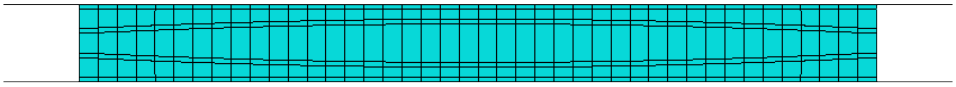

Figure 6.1: Elevation view of the finite element model of bearing with shim bending in the undeformed configuration

Figure 6.2 depicts the bearing in the deformed configuration. It can be seen that the middle layer experiences increased bulging in the center of the section as the bulging is less restrained at this location.

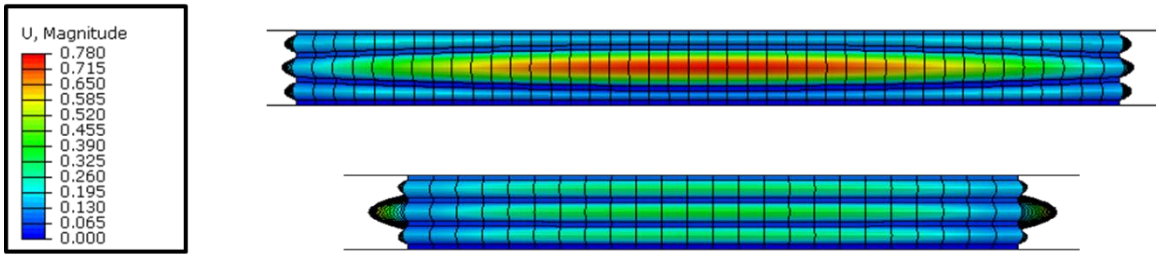

Figure 6.2: Elevation view of the finite element model of bearing with shim bending in the deformed configuration

As expected this phenomenon influences the axial stiffness of the bearing. The impact can be seen when comparing a perfect configuration against an imperfect. To better illustrate this, the axial pressure-displacement curves were plotted for several imperfection levels. It is noted that the average pressure is reported, as pressure varies over the face of the layer. Figure 6.3 illustrates the pressure variation, with pressures becoming essentially

zero at the edges. This comes as a result of the reduced restraint against deformation near the edges, where the elastomer is free to bulge.

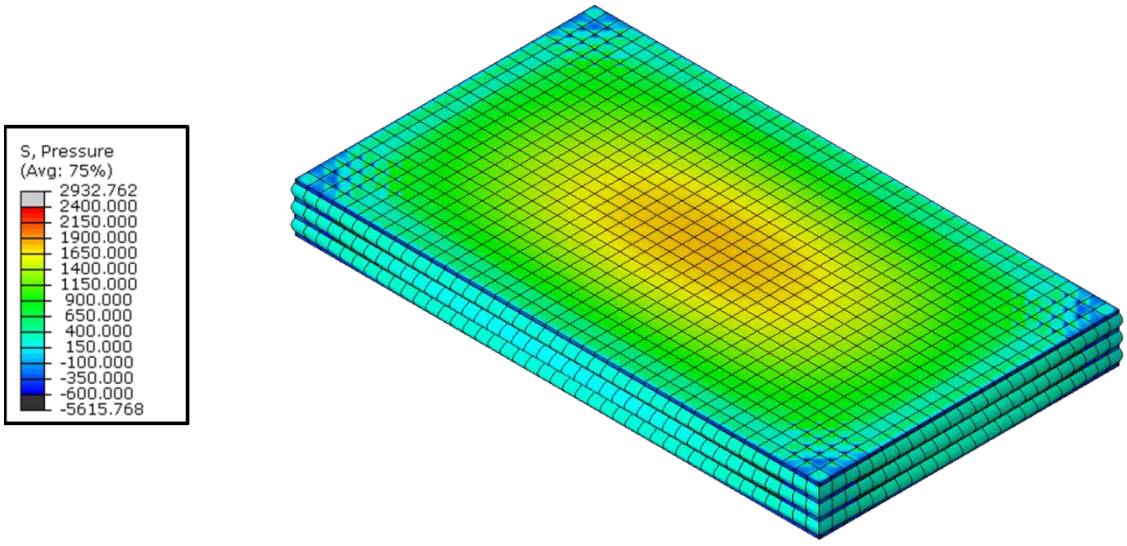

Figure 6.3: Pressure variation over the layer face (perfect configuration)

Figure 6.4(a) and (b) plot the predicted average pressure-displacement curves for several levels of imperfection. The bearings for which the results are plotted had a shape factor equal to 7.5 and 8 and aspect ratios of one and two respectively. It can be observed that after 25% of out-of-straightness imperfection, the axial stiffness losses become significant for a bearing with a plan area aspect ratio of one. A similar trend occurs for the rectangular bearing; however, the losses are more significant.

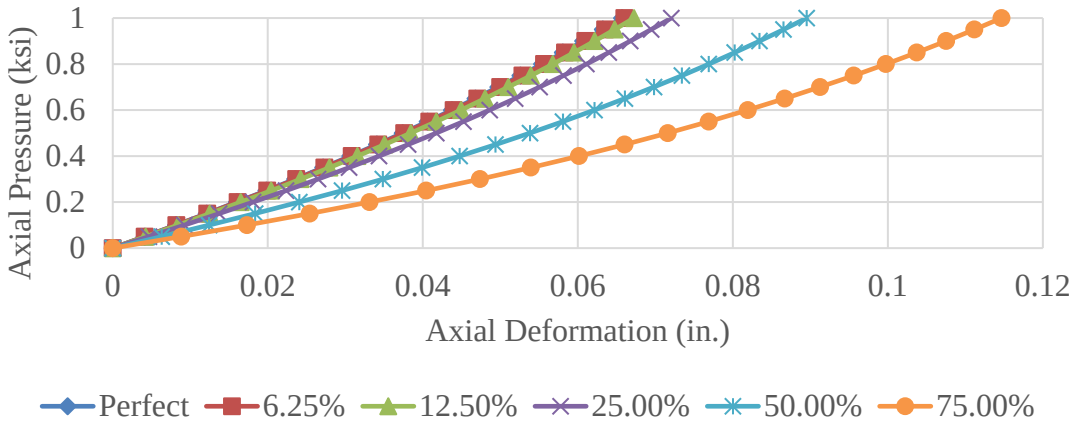

(a)

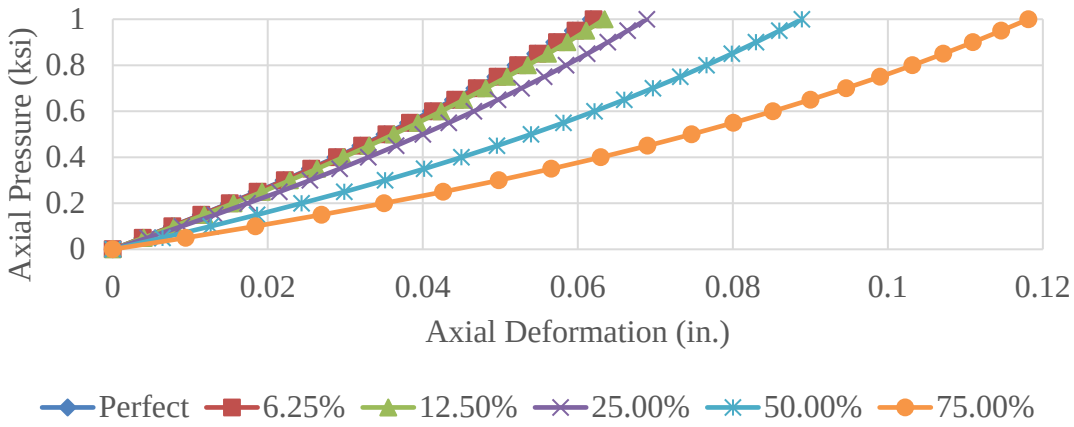

(b)

Figure 6.4: Average axial pressure-deflections curves for different imperfections (a) AR=1.0, S=7.5 (b) AR=2.0, S=8

Plots of average pressure vs. displacement for bearings with aspect ratios the same as above, but with shape factors equal to twenty are shown in Figure 6.5(a) and (b). The trend for those bearings is similar to the trend observed previously (i.e. decreasing stiffness

with increasing imperfections), however the decline in axial stiffness is less prominent compared to the perfect or near-perfect configurations. Additionally, both cases are observed to maintain their axial stiffness with imperfections on the order of 25% of the layer thickness.

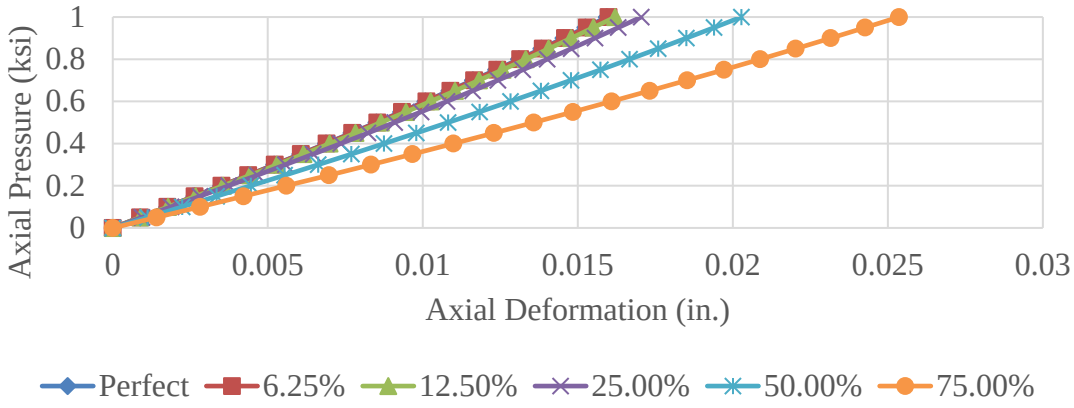

(a)

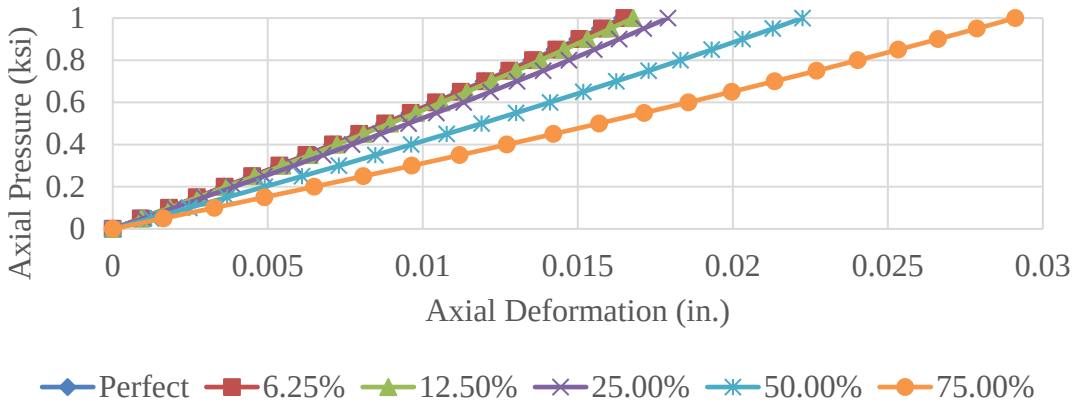

(b)

Figure 6.5: Average axial pressure-deflections curves for different imperfections (a) AR=1.0, S=20 (b) AR=2.0, S=20

Figure 6.4 and Figure 6.5 indicate the influence, although minor, of the aspect ratio and shape factor on the axial stiffness with imperfections in steel-laminated elastomeric bearings. This is attributed to the loss of restraint against bulging with increasing average axial pressure, whereas, in more restrained layers (i.e. higher shape factors), the impact is masked by the overall increased restraint.

To investigate this hypothesis, the models with a range of aspect ratios and shape factors, described in Chapter 4, were analyzed. To better visualize the impact of the aspect ratio and the shape factor for different levels of imperfections, normalized bearing axial stiffness surface graphs are plotted for each aspect ratio as seen in Figure 6.6(a) through (e). The axial stiffness values are normalized by the predicted axial stiffness for the perfect (straight and parallel) configuration.

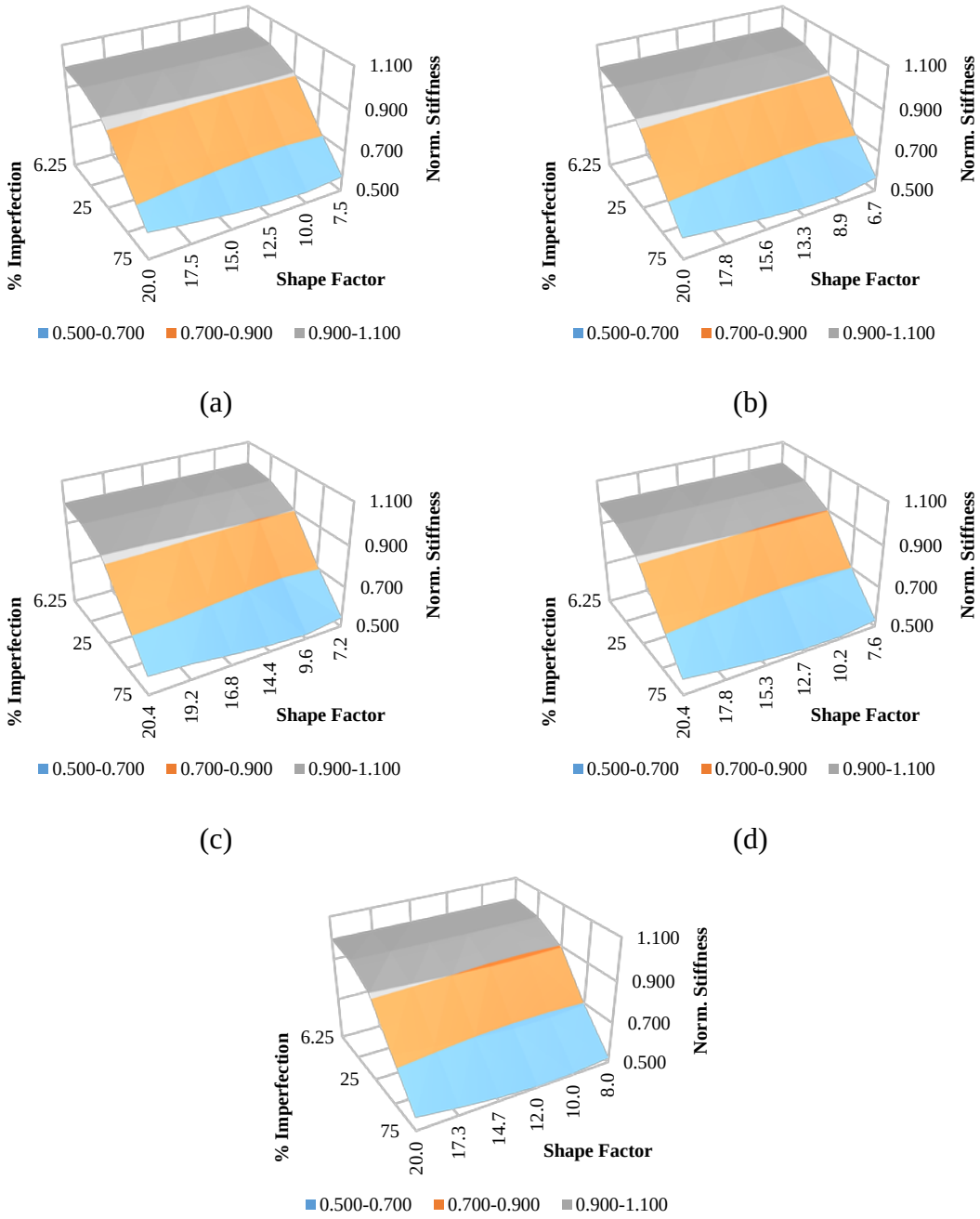

Figure 6.6: Normalized axial stiffness vs. percent imperfection and shape factor for aspect ratios of (a) 1.0, (b) 1.25, (c) 1.5, (d) 1.75, and (e) 2.0

Figure 6.6(a) to (e) confirm the hypothesis by indicating that higher aspect ratios at higher shape factors exhibit slightly more significant decrease in the axial stiffness for a given level of imperfection. Bearings with higher aspect ratios and shape factors are of particular interest for higher demand applications. The higher aspect ratios are utilized to accommodate larger rotations and increased shape factors are used to accommodate larger vertical reactions.

The results of this study also demonstrate that the “forgiving nature” of bearings to imperfections (AASHTO 2012) in not necessarily true for bearings used in higher demand applications. Although AASHTO refers to imperfections in terms of construction and placement of the bearing, these findings further indicate the need for increased quality assurance procedures for bearing intended for higher demand applications.

Moreover, although shear strain measurements were outside of the focus of this dissertation, it is expected that in addition to the decrease in the axial stiffness, the shear strains at the layer edge will be increased in the case when imperfections are present, resulting in bearings that be may prone to fail at lower-than-design loads.

Finally, it must be stressed that the reported axial stiffness values, actual and normalized, correspond to the three-layer bearing configuration. The impact of any layer imperfection affects primarily the axial stiffness of the individual layer and secondarily the axial stiffness of the bearing as a whole. In addition, the effect of the layer imperfection on the axial stiffness decreases with the increase of layers.

6.2.2 EFFECT OF SHIM MISALIGNMENT

This section presents the results of the analyses investigating the impact of misalignment imperfections for bearings with shape factors ranging between 7.5 and 20 and aspect ratios ranging from one to two. The results are expected to be comparable to the case of shim bending (Figure 6.1), described previously, however, as the bulging profile is different (i.e. the restraint is released at different locations) an evaluation of those imperfections was deemed necessary.

Herein, misalignment imperfections are defined with the following two parameters. The first describes the offset of one shim edge from the assumed position and the second describes the offset of the other shim edge. Offset is described in terms of percentage relative to the thickness of the rubber layer. The bearing with the parameters under consideration is shown in Figure 6.7.

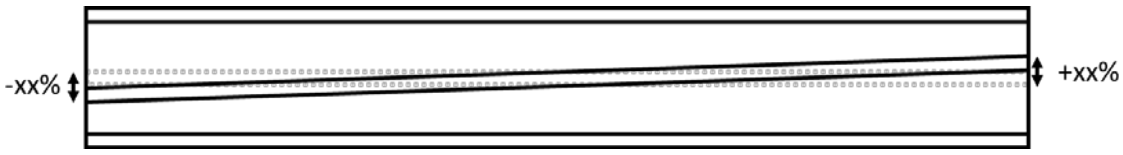

Figure 6.7: Model incorporating misalignment imperfections (-xx%/+xx%)

Figure 6.8(a) and (b) illustrates the average pressure-deformation curves for two square bearings with different shape factors, 7.5 and 20 respectively for several levels of imperfections. It can be seen that stiffness reduction becomes noticeable at total imperfection levels of approximately 40%. This trend can be also seen in Figure 6.9(a) and

(b) where the equivalent curves for bearings with the same shape factors but a higher aspect ratio are plotted.

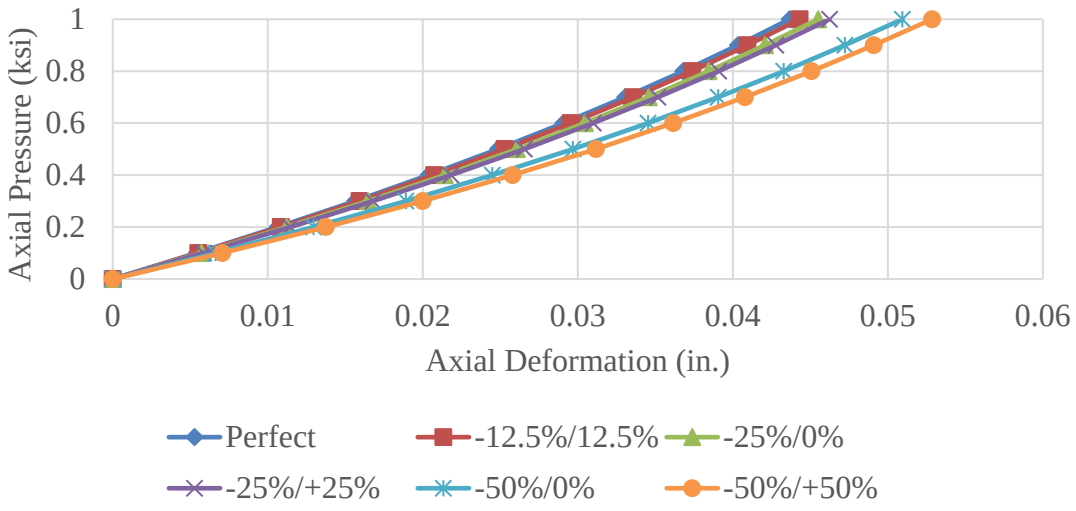

(a)

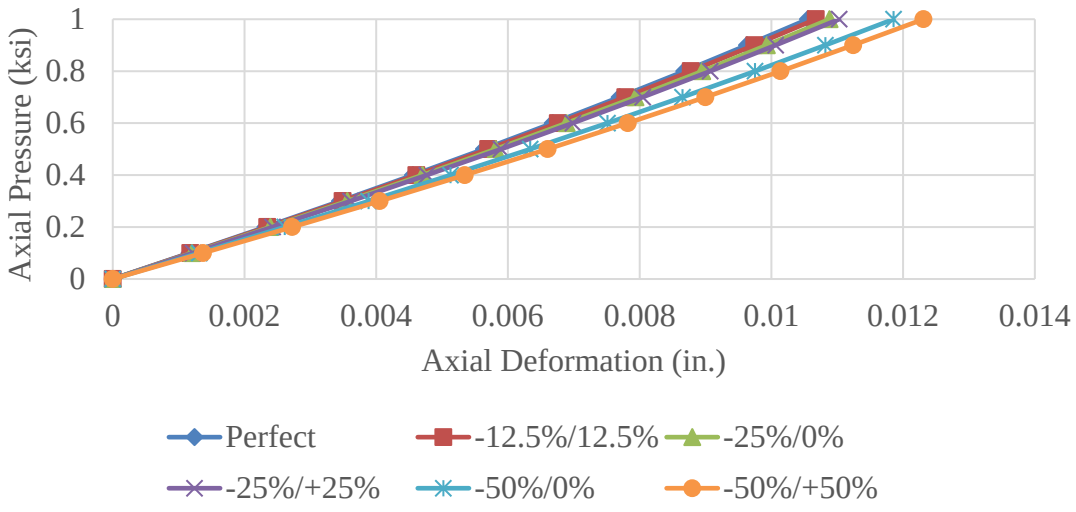

(b)

Figure 6.8: Average axial pressure-deflections curves for different imperfections (a) AR=1.0, S=7.5 (b) AR=1.0, S=20

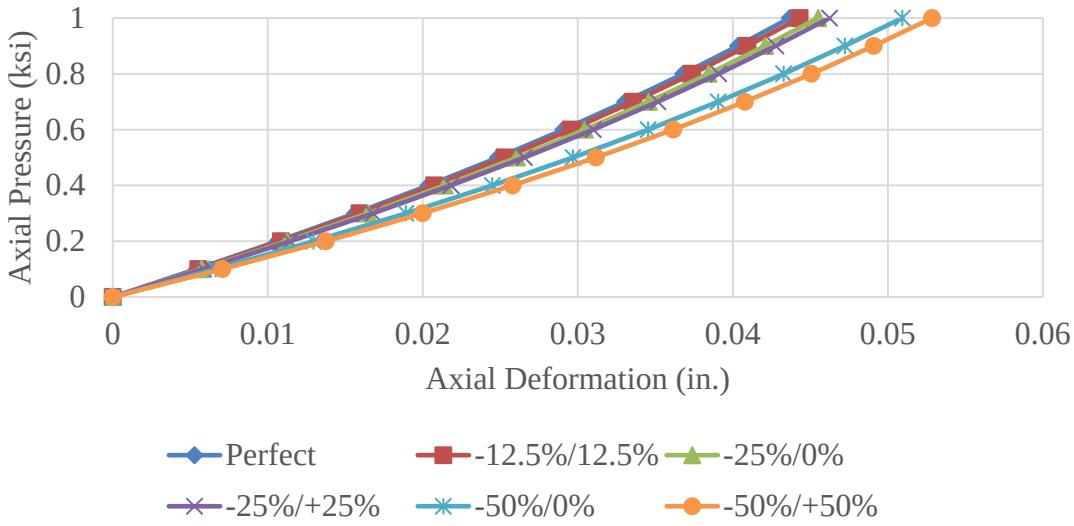

(a)

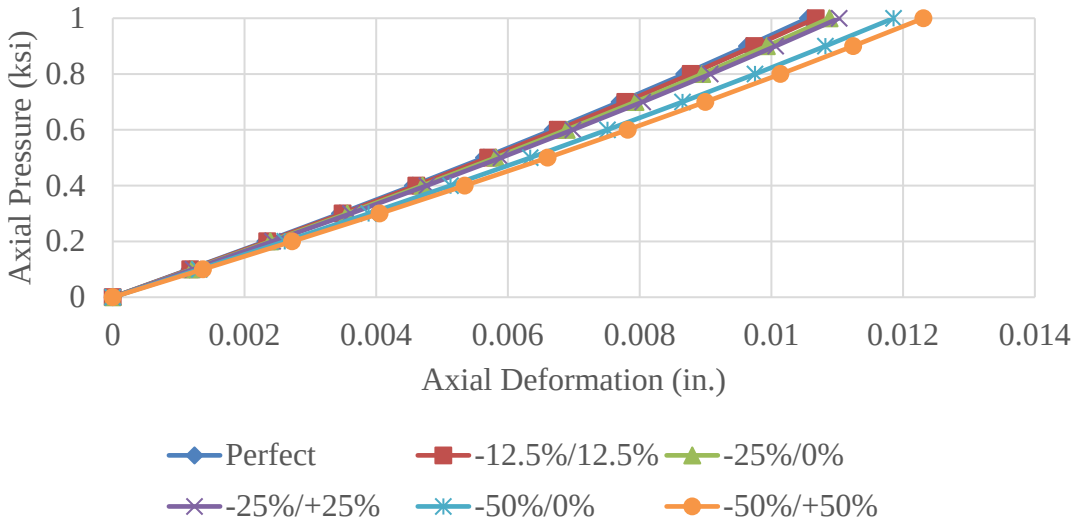

(b)

Figure 6.9: Average axial pressure-deflections curves for different imperfections (a) AR=2.0, S=8 (b) AR=2.0, S=20

These results indicate that in the case of shim misalignment, the axial stiffness significantly reduces, only when an excessive level of misalignment is applied, which would indicate a poor manufacturing process.

In an effort to evaluate the results from all the analyses conducted, and to further support the previous statement, a statistical analysis was conducted on the axial stiffness results obtained for a given absolute total imperfection level. Figure 6.10 shows the cloud of points relating the total imperfection amounts to the normalized axial stiffness, along with the average and the corresponding 95% confidence intervals. Each stiffness is normalized with respect to the perfect configuration (i.e. parallel shims and equal thickness layers).

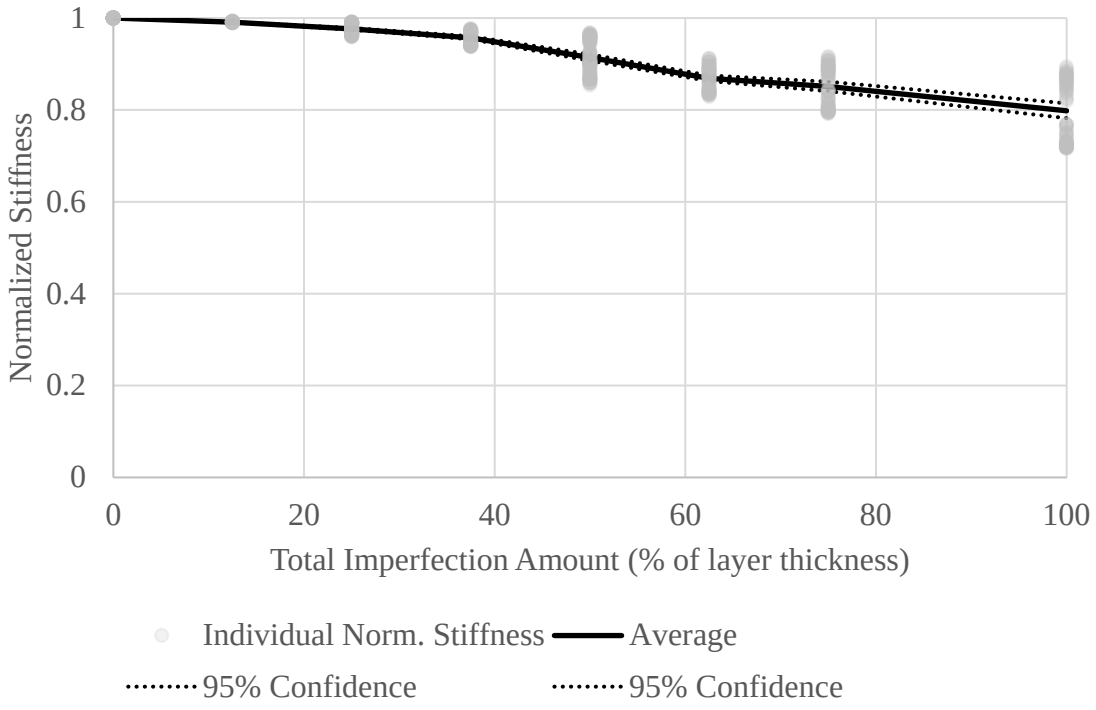

Figure 6.10: Normalized axial stiffness vs. total imperfection for all cases of misalignment imperfection considered in this study

As expected, the axial stiffness decreases with increasing imperfection levels. However, on average, only 10% of the stiffness is lost for a total misalignment imperfection of 50%. Consequently, it can be stated that misalignment imperfections are less likely to be the cause for the discrepancy between predicted and observed axial behavior of steel-laminated elastomeric bearings, as observed in Chapter 5 and in Han (2016).

6.2.3 EFFECT OF FRICTION

Cover layers of steel-laminated elastomeric bearings are usually not bonded to the superstructure or substructure, relying only on friction to transfer horizontal forces

(Bradberry, Cotham et al. 2005). However, this installation method reduces the axial stiffness of the cover layers (Kelly and Konstantinidis 2009). An attempt to address this issue in design codes was made by requiring a thinner cover layer, relative to the internal layers (AASHTO 2012). In this subsection, results are presented from the numerical studies conducted on a series of different cover layers with a wide range of aspect ratios (1.0 to 2.0) and shape factors (7.5 to 20) and for a practical range of coefficients of friction (0.2-0.5). All results are compared with their equivalent bonded case.

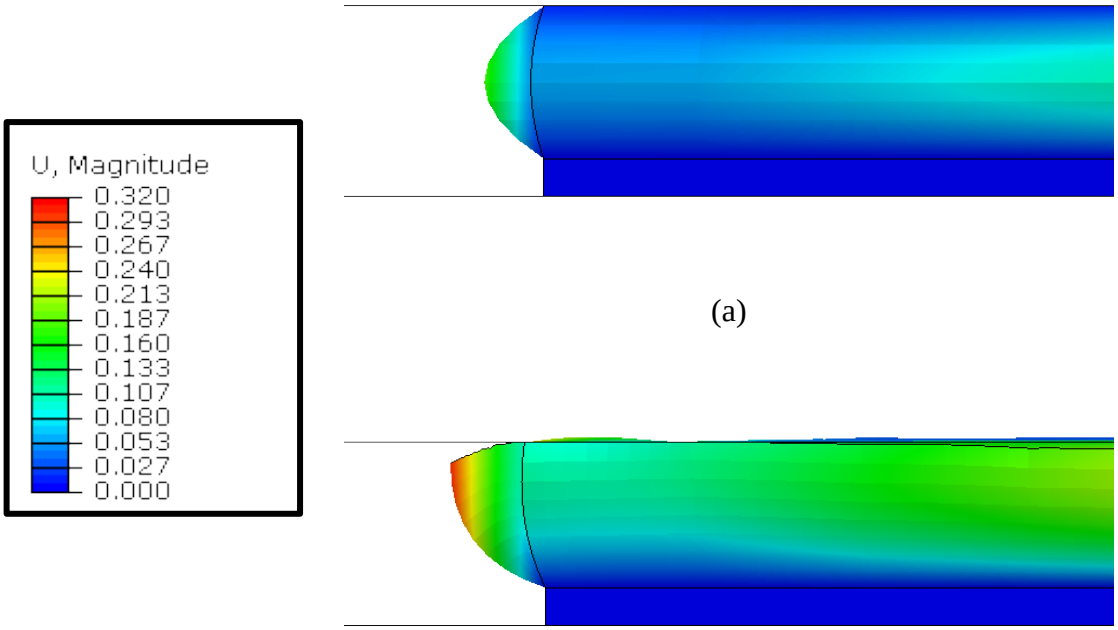

(a)

(b)

Figure 6.11: Deformed configuration of (a) bonded, and (b) friction (μ=0.3) bearing cover layer

Figure 6.11(a) and (b) illustrate the deformed shapes of two identical elastomeric bearings that are analyzed as: (a) having the top and bottom faces bonded to the sub- and superstructure, and (b) having the bottom face bonded and relying on friction (μ=0.3) for the top face. The sectional cuts shown in Figure 6.11(a) and (b) have the same geometry of rubber layer (AR=2.0, S=7.5), are at the same location, and have the same average axial pressure. As can be seen, the deformations are significantly larger for the friction case, leading to lower axial stiffness.

Average axial pressure-deformation curves for the same layers are shown in Figure 6.12. This figure shows the case of a bonded top layer, as well as unbonded top layers with various values of coefficient of friction. These results show the significant impact of the bonded vs. unbonded top face conditions on the axial stiffness. It can also be seen that axial stiffness reduces with reduced coefficient of friction, although the effects are very minor for the range of coefficients of friction considered in the analyses (0.2 to 0.4).

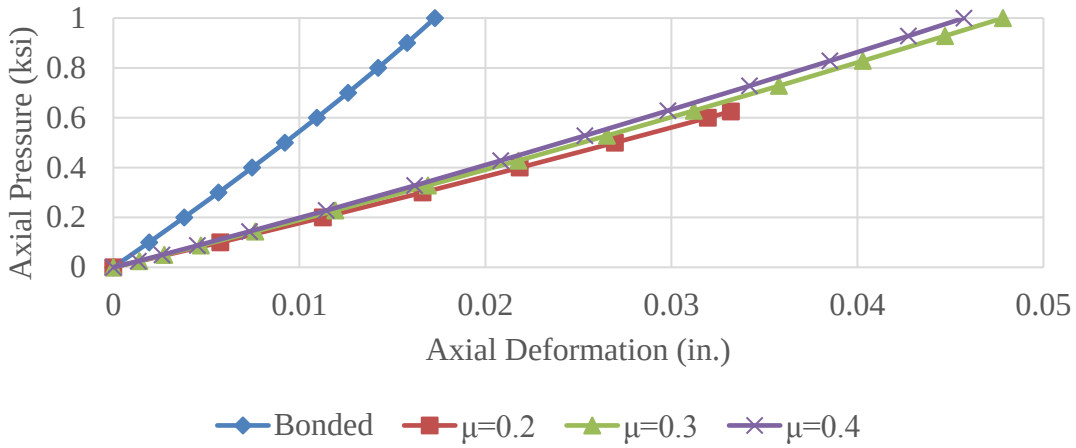

Figure 6.12: Average axial pressure-deformation for bonded top layer, and unbonded top layer with varying coefficients of friction

Figure 6.13(a) to (e) summarize the results obtained from the numerical studies on friction. These plots show how the normalized axial stiffness (with respect to the bonded case) varies with coefficient of friction, shape factor, and aspect ratio. As can be seen, varying the coefficient of friction, although insignificant when compared to the bonded case, does result in some changes in bearing axial stiffness for the range of aspect ratios, shape factors, and coefficients of friction considered. Specifically, for a given aspect ratio and shape factor, the axial stiffness decreases with decreasing coefficient of friction.

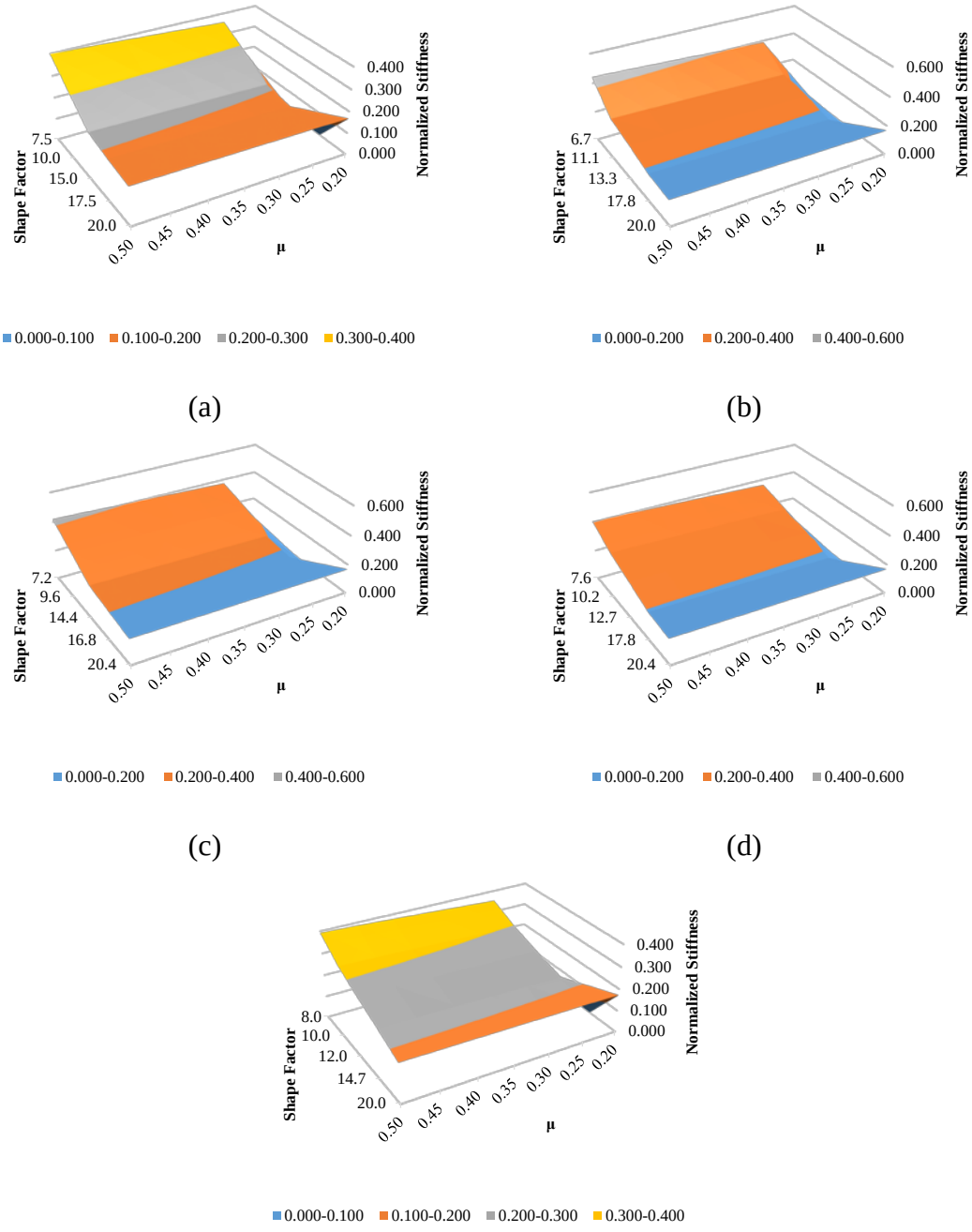

Figure 6.13: Normalized axial stiffness vs. coefficient of friction and shape factor for aspect ratios of (a) 1.0, (b) 1.25, (c) 1.5, (d) 1.75, (e) 2.0

The relationship between axial stiffness and shape factor can be a result of the increased restraint against slipping for a larger portion of the rubber face, as contact pressures are increased toward the center of the bearing (Figure 6.3). This may explain the lower variations in axial stiffness at higher shape factors, for the range of coefficients of friction investigated. Increased coefficient of friction increases the shear stress required for the unbonded surface to slip when compressed. As a result, it is reasonable that axial stiffness increases with higher coefficients of friction.

Summarizing, it has been shown that layers unbonded on one side experience more axial deformation for a given load than when they are bonded both at the top and bottom. This effect is more prominent for layers with a lower shape factor and unbonded surfaces with lower coefficients of friction.

6.3 Results of Studies on Factors Affecting Shear Stiffness

6.3.1 Effect of Shear direction

This subsection presents the results of the numerical study on the effect shear direction on the shear stiffness of bearings. The direction of he applied shear force is defined by the angle θ, as shown in Figure 4.13. Note that θ = 0 corresponds to a load applied parallel to the long side of the bearing, whereas θ = 90° corresponds to a load applied parallel to the short side. A series of numerical models were developed, capturing a wide range of the aspect ratios (1.0 to 2.0) and width to height ratios (10 to 2.5) for a constant axial pressure of 1000 psi, a typical value used in practice. The direction of the applied shear loading was varied from 0 to 90°, in 15° increments.

Figure 6.14(a) and (b) show deformed shapes of the same bearing (AR=2.0, W/hrt=2.5) when sheared in the two principal loading directions, i.e., along the short dimension (θ = 90°) and along the long dimension (θ = 0). Figure 6.15(a) and (b) show force-displacement curves for two square bearings (AR=1.0, W/hrt=2.5 and AR=1.0, W/hrt=10) for all directions of shearing considered.

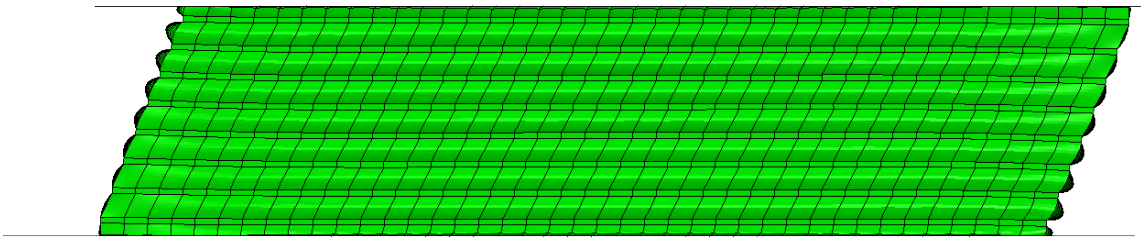

(a)

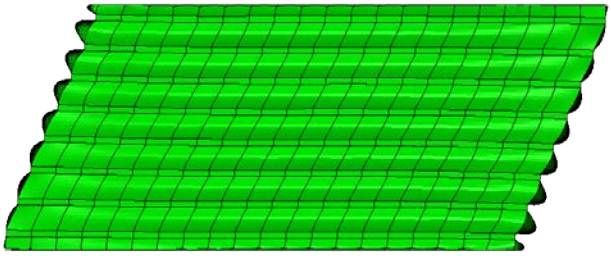

(b)

Figure 6.14: Bearings in the deformed configuration (a) AR=2.0, W/hrt=2.5, θ=0° (b) AR=2.0, W/hrt=2.5, θ=90°

As can be seen, the expected symmetry about 45° is correctly captured. The results show there is almost no direction dependency for the shortest bearing (AR=1.0, W/hrt=10), which is confirmed by experimental measurements, presented in Chapter 5, and previous numerical research (Nguyen and Tassoulas 2010). This tendency is also confirmed for taller bearings. As seen in Figure 6.15(b), the bearing exhibited equal lateral stiffness in all directions of shearing. Although this was expected for the two principal directions, the lateral stiffness of a square bearing was found to be non-sensitive to the direction of shearing, irrespective of the W/hrt ratio.

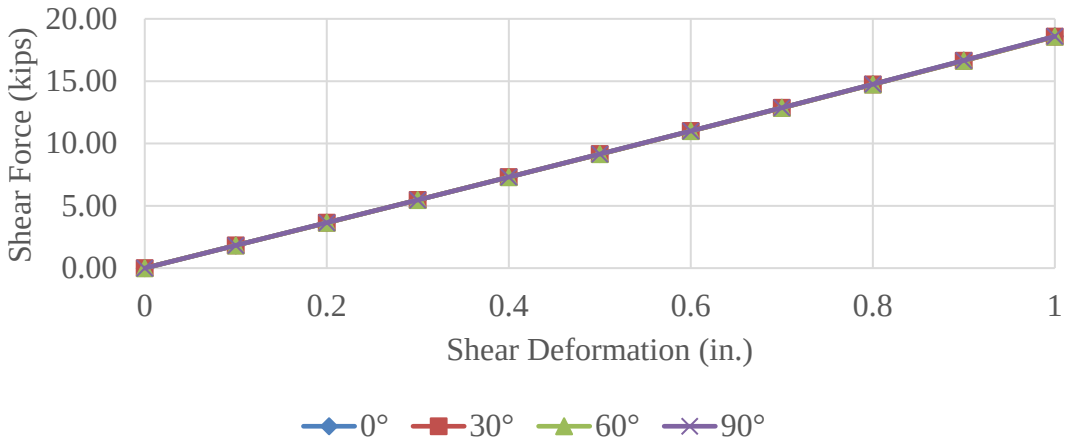

(a)

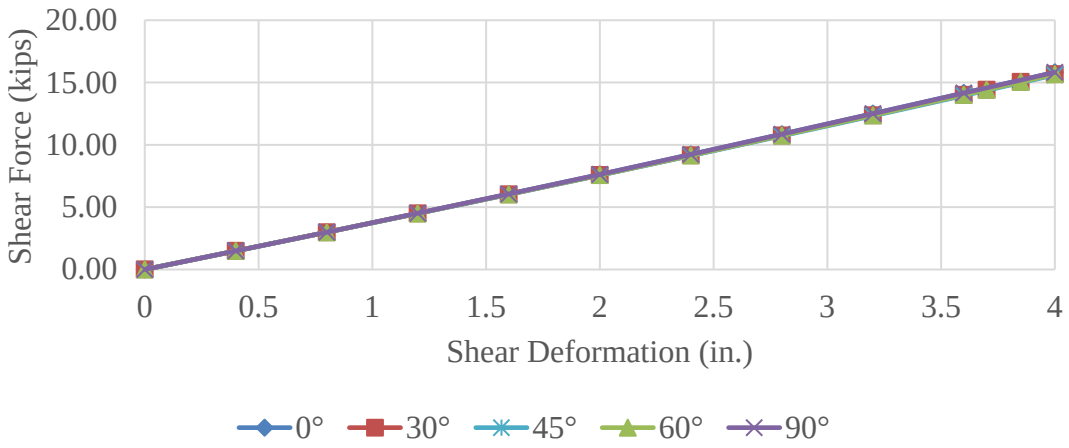

(b)

Figure 6.15: Force-displacement curves for different shear directions (a) AR=1.0, W/hrt=10 (b) AR=1.0, W/hrt=2.5

Figure 6.16(a) shows the force-deformation curves for all shearing directions for the bearing with AR=2.0, W/hrt=2.5. Figure 6.17(b) shows the variation of shear stiffness

with shearing direction. As can be seen, apart from the larger variability of the shear stiffness with the shearing direction, the shear stiffness approaches the theoretical value as θ decreases. This can be attributed to the fact that as θ decreases, a state closer to the state of simple shear is taking place. This observation is consistent with experimental results for the taller bearing presented in Chapter 5. This implies that a state of shear combined with more pronounced bending is occurring at higher values of θ. This is supported by the observation that the layers are more prone to rotate when the bearing has more layers, thus increasing the total rotation, and when sheared along the dimension where the layers have less resistance, i.e. the short direction of a rectangular bearing. In order to further support this argument, the rotation of individual layers is shown for the two extreme shearing directions ($\theta=0°$ and $\theta=90°$) in Figure 6.17. The angle of rotation of a layer is defined at the rotation of the shim layer directly above it.

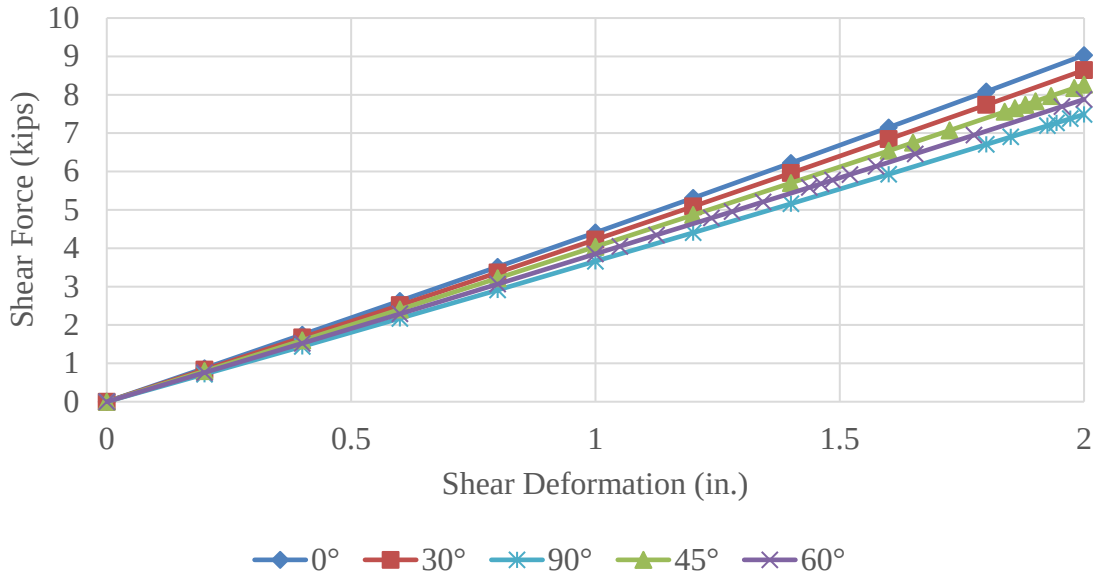

(a)

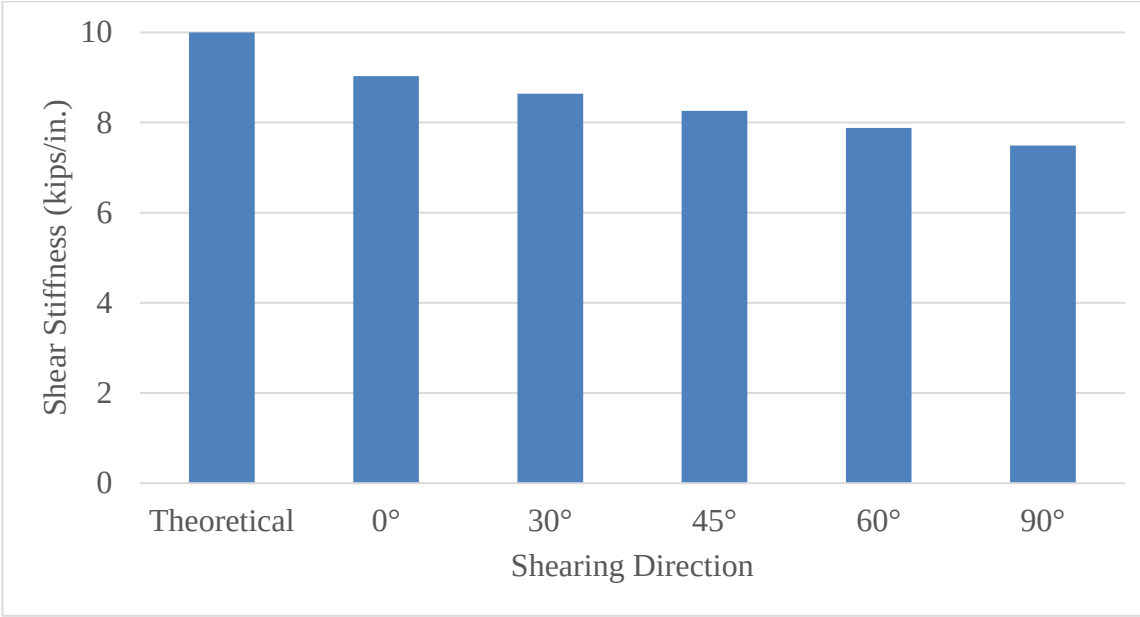

(b)

Figure 6.16: Force-deformation curves for bearing with AR=2.0, W/hrt=2.5

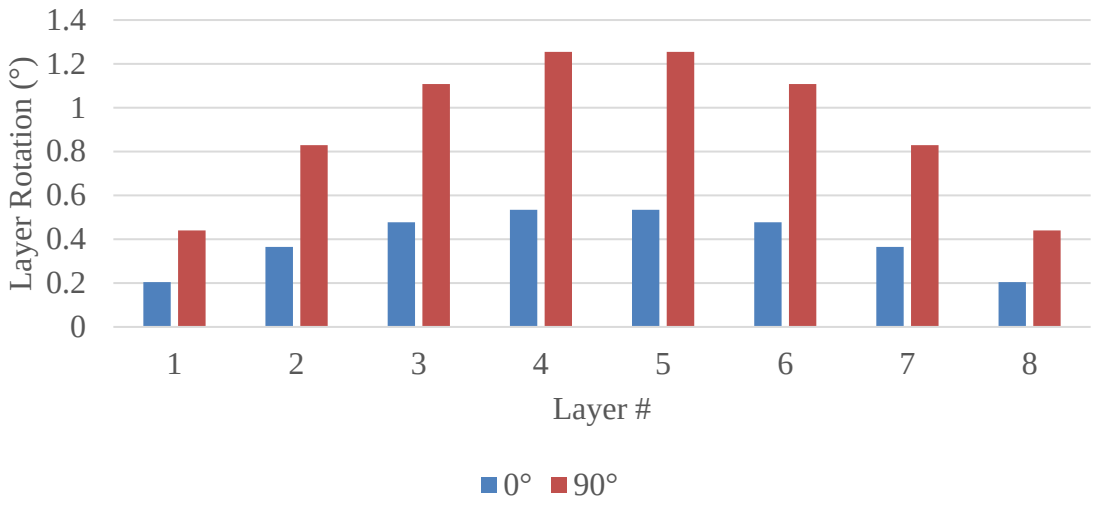

Figure 6.17: Angle of rotation of layers when sheared along long (0°) and short (90°) dimension (AR=2.0, W/hrt=2.5)

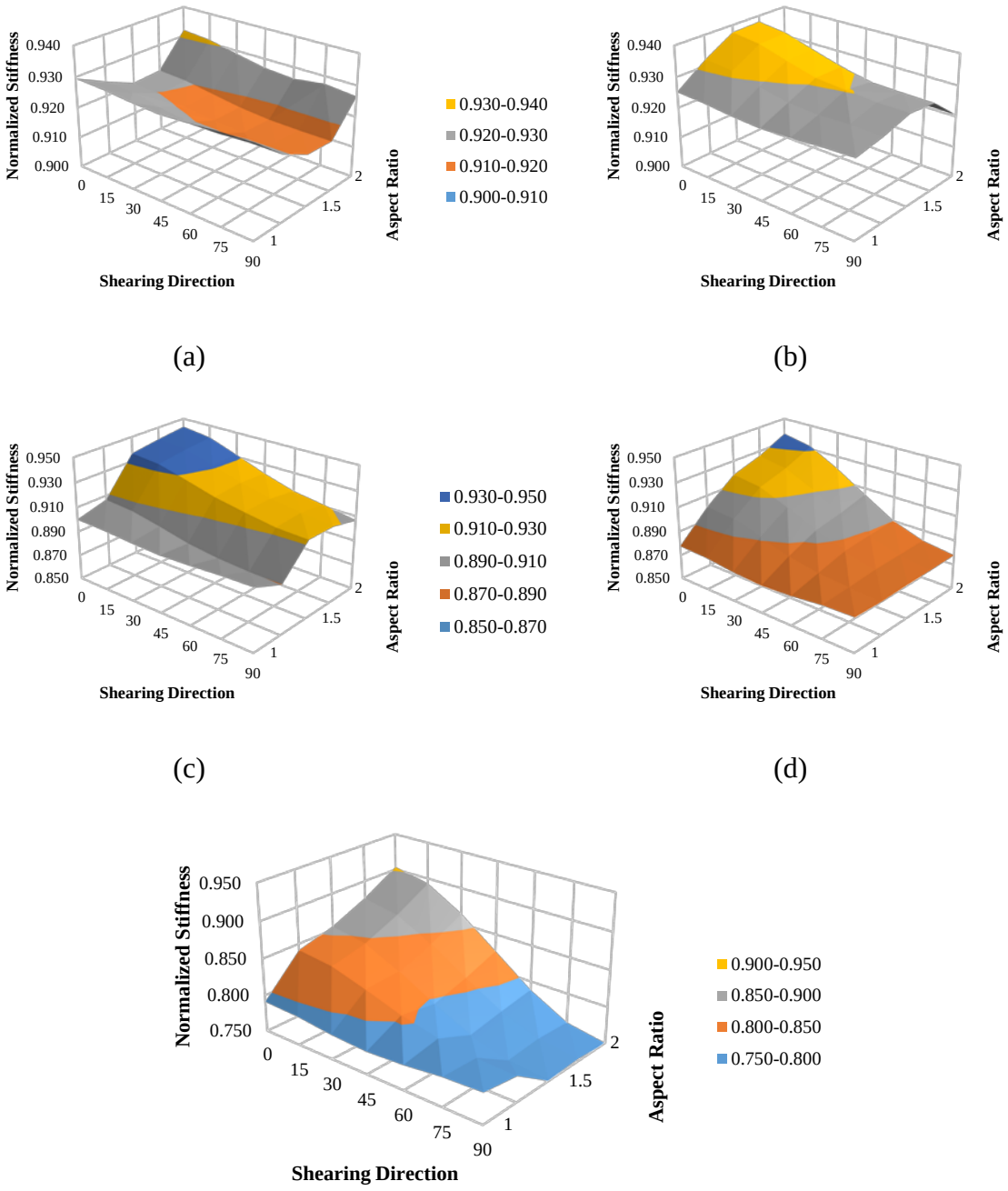

Figure 6.18: Normalized shear stiffness vs. shear directions and aspect ratios for W/hrt ratios of (a) 10, (b) 8, (c) 5, (d) 4, (e) 2.5; Axial pressure = 1000 psi

Figure 6.18 summarizes the results of the numerical studies on the effect of shear loading direction on shear stiffness. All results are for an axial pressure of 1000 psi. The shear stiffness is normalized with the theoretical prediction (GA/hrt) for each bearing under consideration. These plots show that as the shearing conditions diverge from the conditions of simple shear (i.e. increased W/hrt ratio and shear along the long bearing dimension), the shear stiffness decreases as more flexible modes of deformation participate in an increased manner in the bearing deformation. As can be seen, for all cases, the shear stiffness calculated was lower than the theoretical value GA/hrt.

6.3.2 EFFECT OF AXIAL PRESSURE

This subsection presents results of the studies on the effect of the average axial pressure on the shear stiffness of steel-laminated elastomeric bearings. The same models presented in Section 6.3.1 were analyzed with the axial pressure being a variable.

The average axial pressures under consideration were 1000, 1500, and 2000 psi. As a basis for evaluating results, the shear stiffness values obtained in this subsection were normalized with respect to the 1000 psi cases, described previously. Results are illustrated in Figure 6.19(a) to (e) and Figure 6.20(a) to (e).

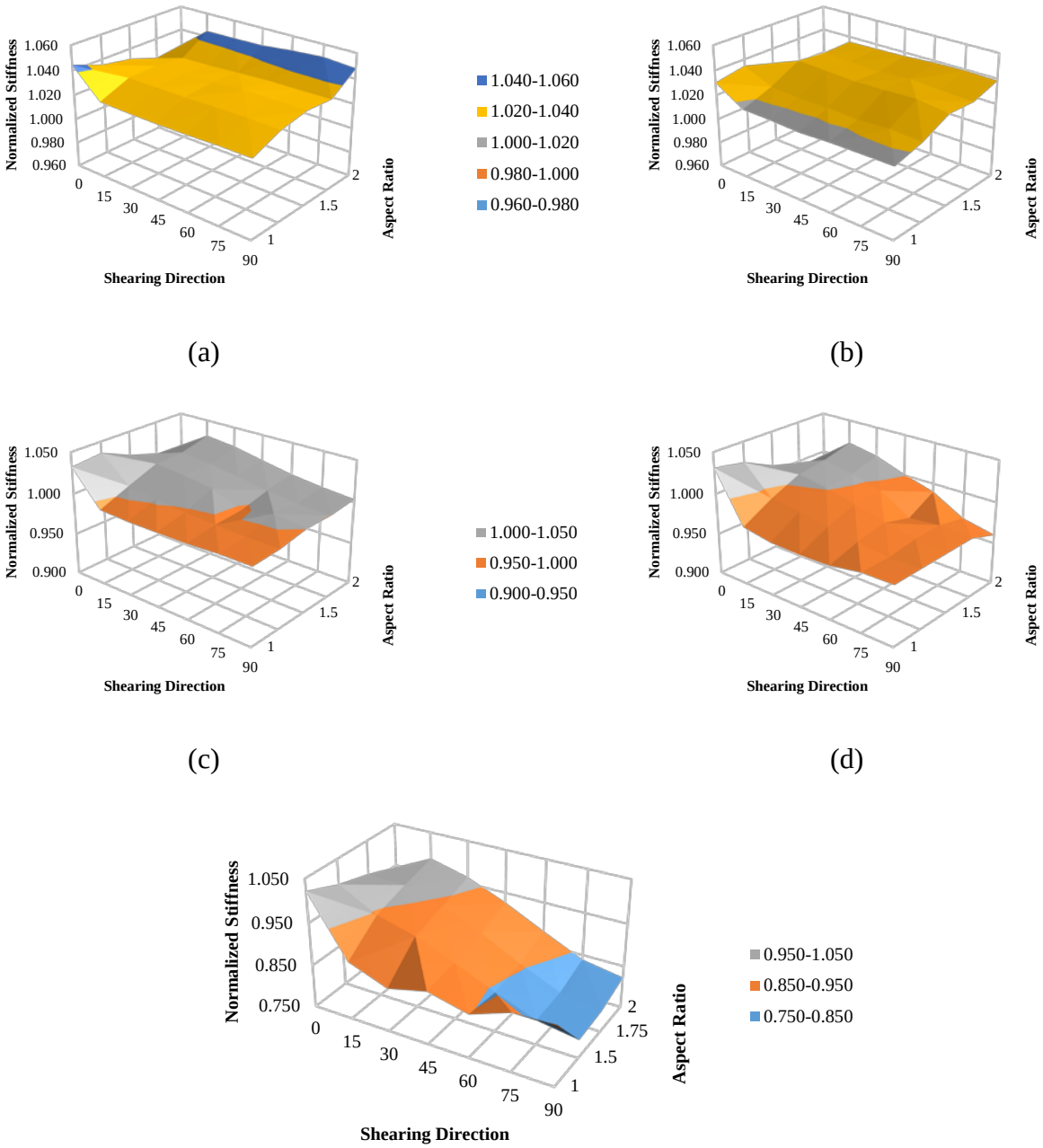

Figure 6.19: Normalized shear stiffness vs. shear directions and aspect ratios for W/hrt ratios of (a) 10, (b) 8, (c) 5, (d) 4, (e) 2.5; Axial pressure = 1500 psi

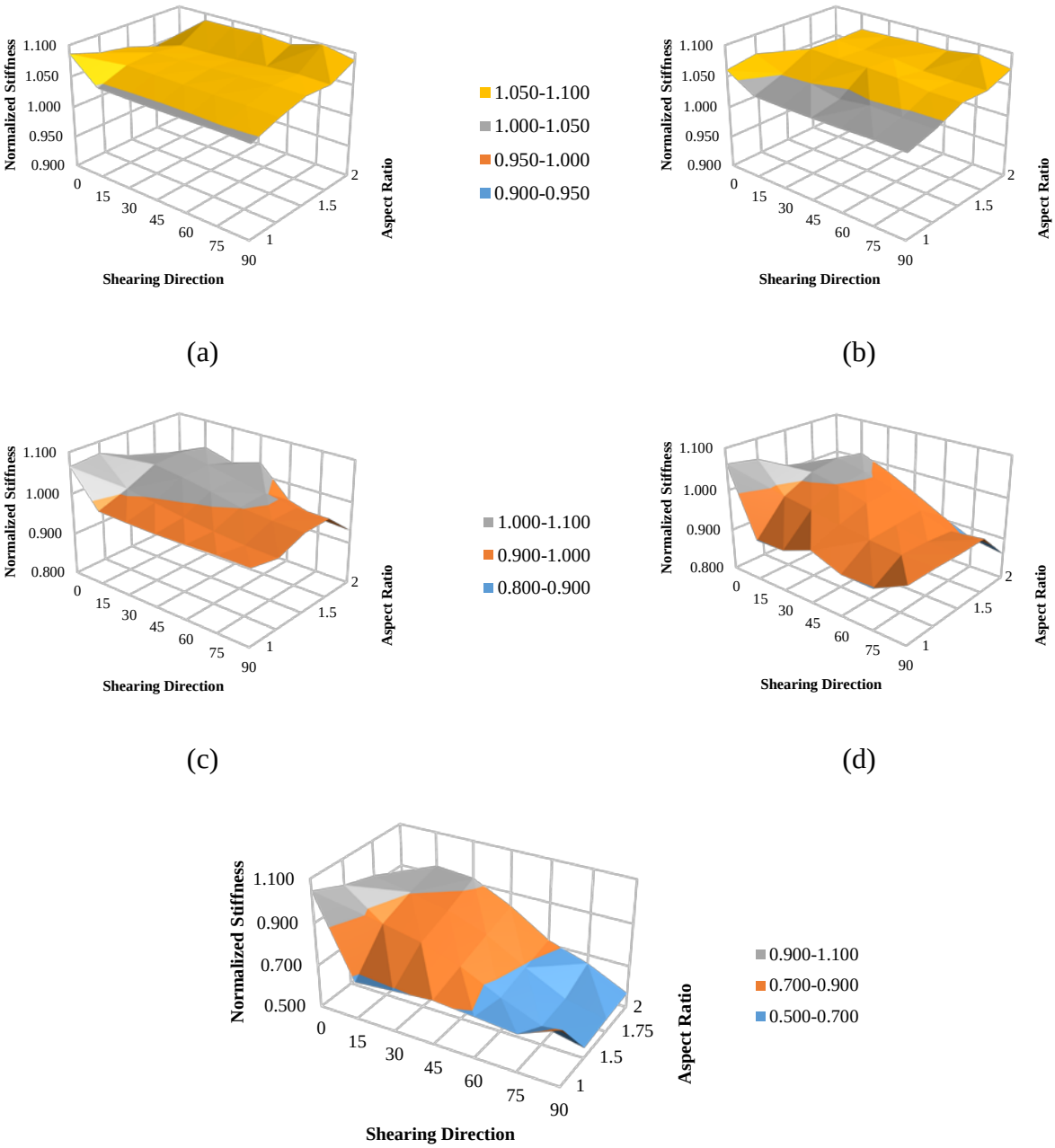

Figure 6.20: Normalized shear stiffness vs. shear directions and aspect ratios for W/hrt ratios of (a) 10, (b) 8, (c) 5, (d) 4, (e) 2.5; Axial pressure =2000 psi

As indicated by Figure 6.19(a) to (d) and Figure 6.20(a) to (c), increased axial pressure has only a minor effect on the shear stiffness of bearings with W/hrt ratios greater than 5. This is likely due to the fact that a state of pure shear is essentially maintained for all cases in that range. This trend, however, is not maintained for taller bearings (i.e. W/hrt $\leq$4), for which increased axial pressures result in lower shear stiffness. The phenomenon is more pronounced at higher aspect ratios and for shearing direction along the shorter dimension of the bearing. The reduced shear stiffness, in addition to the association with the axial pressure approaching the buckling load of the bearing (Haringx 1942), can be caused by the eccentricity induced by the axial load while shearing the bearing. As a result, the stiffness reduction is more pronounced in bearings with higher aspect ratios.

6.4 Summary

This Chapter described and illustrated the main findings of the numerical studies that were performed during this study. For the effect of imperfections and friction on axial stiffness, the results of the numerical studies supported observations made in the experimental portion of this study. These results indicate that manufacturing imperfections in addition to cover slippage lead to a decreased axial stiffness in the finished product. The numerical analyses also demonstrated that a significant amount of imperfections would be required in order to obtain axial stiffness reductions of more than 50%, a fact that should be considered in manufacturing quality control. The numerical results also showed that significantly decreased axial stiffness in the bearing cover layers occurs when the bearing is not bonded to the adjoining super- or substructure surfaces, with friction being the only means for transmitting shear forces. Further, the bearing axial stiffness decreases with decreasing coefficient of friction.

Concerning the shear stiffness of a steel-laminated elastomeric bearing, these studies showed that, contrary to previous studies, the shear stiffness can be up to 40% lower than the theoretical value, for the taller bearings considered herein. This reduction in shear stiffness may not be a critical issue in many bridge applications, as the amount of shear deformation at the bearing is controlled by thermal movement of the bridge (i.e., expansion and contraction) and is not affected by the bearing's shear stiffness. However, this finding may be more critical for cases where the shear deformation is a function of the bearing's shear stiffness, as may occur under earthquake loading. Although cylindrical bearings are

most commonly used in those types of applications, eliminating the directivity effect, the D/hrt ratios employed are low and as a result, the reduced stiffness can have a detrimental impact in the actual structural behavior.

CHAPTER 7: SUMMARY AND CONCLUSIONS

7.1 Summary

This dissertation investigated the u potential of using steel-laminated elastomeric bearings in higher demand applications for bridges. This study considers bridges with very long spans and/or complex geometry in terms of curvature and skew, that place high force and deformations on the bearings. In current practice, such bridges are normally provided with more costly bearing systems, such as pot bearings. Using steel-laminated elastomeric bearings for such bridges could result in potentially significant cost savings. Experimental tests and numerical simulations were performed in this research study to characterize the behavior of elastomeric bearings under large force and deformation demands.

This study evaluated the axial stiffness and strength of elastomeric bearings under increased axial loads. Additionally, the behavior under higher translational and rotational demands, associated with higher demand applications, was evaluated. Furthermore, the dependency of the shear stiffness on the shearing direction was assessed, reflecting the shearing behavior observed in curved bridge systems. Finally, temperature-dependent hyperelastic material coefficients for neoprene rubber were evaluated for several material models.

The dissertation includes of a literature review (Chapter 2), an experimental study involving large-scale testing of bearings qualifying for higher demand applications (Chapters 3 and 5), and a numerical study involving detailed finite element simulations (Chapters 4 and 6).

7.1.1 EXPERIMENTAL PROGRAM

The experimental program, presented in Chapters 3 and 5, involved an exhaustive experimental investigation of elastomeric bearings. To accommodate the research objectives, a test setup capable of applying four million pounds of axial force, ±8 in. of lateral displacement, and up to 2° of rotation was developed. The level of testing ranged from basic material testing to determine material properties and behavior of neoprene rubber to full scale testing of steel-laminated elastomeric bearings in an effort to explore the limitations of current design procedures. Additionally, material and large scale testing was conducted to validate and to develop numerical models being developed in associated work concurrent to this dissertation (Han 2016).

The full-scale experimental program consisted of testing of elastomeric bearings in compression, combined compression and shear, and combined compression and rotation. The bearings tested had aspect ratios ranging from approximately 1.5 to 2.0 and maximum length to height ratios ranging from approximately 2.5 to 5.5 (tall and short bearings respectively).

7.1.2 NUMERICAL SIMULATIONS

The numerical study, presented in Chapters 4 and 6, featured finite element simulations intended to fill knowledge gaps for to issues identified in the literature review and to provide insights into discrepancies found between experimental measurements and theoretical predictions. Specifically, the effect of the shape and location of imperfections in the steel laminates, as well as the magnitude of the friction coefficient, on the axial

stiffness of the bearing were investigated. Additionally, the effects of the shearing direction and axial load on the apparent shear stiffness were investigated. An array with a total of 1,400 models was produced and analyzed.

7.2 Results and design implications

The key results and design implications from this research program are summarized as follows:

1. It was found that current AASHTO elastomeric bearing design provisions applied to higher demand force and deformation applications can provide bearing designs that provide satisfactory performance. AASHTO design Method B, involving a more rigorous design calculation procedure, allows for smaller bearing configurations, as opposed to design Method A, which provides a simplified although more conservative design approach.
2. Due to the absence of data in the available literature, material coefficients were determined for common hyperelastic models to accurately capture the elastomer behavior. A standard global optimization procedure was adopted to fit the experimentally acquired data. The parameter determination space covered a range of temperatures, capturing the instantaneous stiffening characteristics of rubber material. Moreover, hyperelastic material parameters were evaluated to capture the hysteretic behavior of neoprene rubber under a range of temperatures.

   Rubber stiffness was found to increase at temperatures below freezing significantly (up to four times the stiffness at room temperature). As a result, higher shear forces

will be developed for the same shear deformation in the bearing, leading to potentially overcoming of the friction force that is preventing the substructure-bearing and the bearing-superstructure relative movements. This determination of temperature-dependent material coefficients for neoprene rubber should also be useful in applications other than bridge bearings.

3. The determination of material coefficients for the Yeoh model, incorporating hysteretic behavior, allows investigation of damping characteristics of devices incorporating neoprene rubber, such as seismic isolation bearings Although low in damping (2-3%), these damping levels have the capacity to significantly benefit the safe response of the superstructure, especially when the anticipated frequency of motion of the isolated superstructure is high.
4. Equations in the available literature for predicting the axial stiffness of steel-laminated elastomeric bearings were found to have significant limitations in accuracy. Measured results diverge from predictions more significantly for bearings with higher shape factors and for higher width to total rubber height ratios. This was attributed to imperfections in the steel laminates and the effect of friction at the cover layers. Section cuts on bearings revealed that the steel layers were not parallel and in some occasions were bent along their length. Subsequent numerical simulations supported the hypothesis that steel laminate imperfection and friction at the cover layers Are a primary source of the discrepancy between theoretical predictions and experimental measurements of axial stiffness.

5. Shear stiffness of steel-laminated elastomeric bearings was found to be dependent on the axial load level on the bearing and the shear direction. This effect was more prominent for taller bearings relative to their plan directions. Specifically, it was shown that, contrary to previous studies and common practice, the shear stiffness could be up to 40% lower than the theoretical value. As the shear loading in the bearing is mostly controlled by the deformation (i.e. bridge deck/girder temperature expansion/contraction driven shear), it is less probable that friction between the bearing and super/sub structure will be overcome. However, overestimating the bearing's shear stiffness may be more problematic for cases where the shear is imposed by forces that can occur in any direction (e.g. earthquakes), as it could lead to higher deformations than expected. Although cylindrical bearings are most commonly used in these types of applications, which eliminates the directivity effect, the D/hrt ratios employed in such bearings are typically low and as a result, the reduced stiffness can have a detrimental impact in the actual structural behavior.

7.3 Recommendations for future work

This dissertation investigated the applicability of steel-laminated elastomeric bearings for higher demand applications. The main conclusion of this study is that steel-laminated elastomeric bearings can be safely used in higher demand applications and can be an economical alternative to other bearing systems. Nonetheless, additional research would facilitate the use of steel-laminated elastomeric bearings in a wider variety of civil and mechanical engineering applications. Recommendations for future work are outlined as follows:

1. At a material level, research is needed on the increased stiffness due to crystallization. Crystallization is a time-dependent property and was outside of the scope and the time constraints of this study. However, there are cases where rubber can be exposed to lower-than-freezing temperatures for longer periods of time (longer than 6 hours), potentially resulting in further increases in stiffness. The impact of exposure and further material property characterization of this phenomenon for popular hyperelastic models merits further study.
2. Modeling steel-laminated elastomeric bearings requires advanced modeling procedures, not typically used in civil engineering practice. Additionally, full bearing finite element simulations are computationally expensive, rendering them impractical for the design of conventional bridges. As a result, effort should be spent in the development of non-linear spring models capable of further simplifying the bridge simulations, yet accurately simulating the actual bearing behavior.

3. Specifications for quality control procedures for bearing manufacturing are difficult to be implemented as the manufacturing process is mostly proprietary. Nonetheless, development of standardized quality control criteria for manufacturing of steel-laminated elastomeric bearings should be pursued to assure the bearings can achieve specified performance requirements.

REFERENCES

AASHTO (2012). Load and Resistance Factor Design Specification for Highway Bridges, 6th Edition. A. A. o. S. H. a. T. Officials. Washington, D.C.

Anderson, M., P. Mott and C. Roland (2004). "The compression of bonded rubber disks." Rubber chemistry and technology 77(2): 293-302.

ASTM (2012). "D4014–89: Standard Specification for Plain and Steel-Laminated Elastomeric Bearings of Bridges, ANNEX A1." Determination of Shear Modulus: 1-6.

Bakirzis, E. and P. B. Lindley (1970). "Slipping at Contact Surfaces of Plain Rubber Pads in Compression." Civil Eng & Public Works Review/UK/.

Bradberry, T. E., J. C. Cotham and R. D. Medlock (2005). "Elastomeric bearings for steel trapezoidal box girder bridges." Transportation Research Record: Journal of the Transportation Research Board 1928(1): 27-38.

Buckle, I., S. Nagarajaiah and K. Ferrell (2002). "Stability of Elastomeric Isolation Bearings: Experimental Study." Journal of Structural Engineering 128(1): 3-11.

Chen, Q. (2008). Effects of thermal loads on Texas steel bridges, The University of Texas at Austin.

Dassault-Systèmes (2012). "ABAQUS 6.12 Theory manual." Dassault Systèmes Simulia Corp., Providence, Rhode Island.

EN1337-3 (2005). Structural bearings - Part 3: Elastomeric bearings. The European Committee of Standardization, Berlin.

English, B., R. Klingner and J. Yura (1994). "Elastomeric Bearings: Background Information and Field Study."

Gent, A. and P. Lindley (1959). "The compression of bonded rubber blocks." Proceedings of the Institution of Mechanical Engineers 173(1): 111-122.

Gent, A. N. (1964). "Elastic stability of rubber compression springs." Journal of Mechanical Engineering Science 6(4): 318-326.

Gent, A. N. (2012). Engineering with rubber: how to design rubber components, Carl Hanser Verlag GmbH Co KG.

Gent, A. N. and E. A. Meinecke (1970). "Compression, bending, and shear of bonded rubber blocks." Polymer Engineering & Science 10(1): 48-53.

Gerhaher, U., A. Strauss and K. Bergmeister (2011). "Numerical modeling of elastomeric bearings in structural engineering."

Han, L. (2016). Elastomeric Bearings in High Demand Applications: Numerical Study and Experimental Validation, The University of Texas at Austin.

Haringx, J. (1942). "On the buckling and lateral rigidity of helical springs." Proc. Konink. Ned. Akad. Wet 45(533): 142.

Heymsfield, E., J. McDonald and R. Avent (2001). "Neoprene Bearing Pad Slippage at Louisiana Bridges." Journal of Bridge Engineering 6(1): 30-36.

Holownia, B. (1980). "Effect of different types of carbon black on elastic constants of elastomers." Plast. and Rubb.: Mats. and Applics. 5: 129-132.

Kelly, J. and D. Konstantinidis (2009). "Effect of Friction on Unbonded Elastomeric Bearings." Journal of Engineering Mechanics 135(9): 953-960.

Kelly, J. M. and D. Konstantinidis (2011). Mechanics of rubber bearings for seismic and vibration isolation, John Wiley & Sons.

McDonald, J., E. Heymsfield and R. R. Avent (2000). "Slippage of neoprene bridge bearings." Journal of Bridge Engineering 5(3): 216-223.

Mooney, M. (1940). "A theory of large elastic deformation." Journal of applied physics 11(9): 582-592.

Muhr, A. and A. Thomas (1989). "Allowing for non-linear stress-strain relationships of rubber force-deformation calculations. Pt. 1: compression stiffness of bonded rubber blocks." NR Technology 20: 8-14.

Muscarella, J. V. and J. Yura (1995). An experimental study of elastomeric bridge bearings with design recommendations, University of Texas at Austin.

Nguyen, H. and J. Tassoulas (2010). "Directional Effects of Shear Combined with Compression on Bridge Elastomeric Bearings." Journal of Bridge Engineering 15(1): 73-80.

Nims, D. K. and A. Parvin (2000). Instrumented Elastomeric Bridge Bearings, University of Toledo, Department of Civil Engineering.

Ogden, R. W. (1997). Non-linear elastic deformations, Courier Corporation.

Peng, S. H., T. Shimbori and A. Naderi (1994). "Measurement of elastomer's bulk modulus by means of a confined compression test." Rubber chemistry and technology 67(5): 871-879.

Podolny, W. and J. M. Muller (1994). Construction and design of prestressed concrete segmental bridges.

Qiao, S. and N. Lu (2014). "Closed-Form Solutions for Bonded Elastically Compressible Layers." International Journal of Solids and Structures.

Roeder, C. W. and J. F. Stanton (1996). Steel bridge bearing selection and design guide.

Roeder, C. W., J. F. Stanton and T. Feller (1989). Low temperature behavior and acceptance criteria for elastomeric bridge bearings.

Roeder, C. W., J. F. Stanton and A. W. Taylor (1987). Performance of elastomeric bearings.

Stanton, J., G. Scroggins, A. Taylor and C. Roeder (1990). "Stability of Laminated Elastomeric Bearings." Journal of Engineering Mechanics 116(6): 1351-1371.

Stanton, J. F., C. W. Roeder, P. Mackenzie-Helnwein, C. White, C. Kuester and B. Craig (2008). NCHRP Report 596 - Rotation Limits for Elastomeric Bearings. Washington, D.C., Transportation Research Board.

Sun, C. (2015). Material Study of the Steel Reinforced Elastomeric Bridge Bearings, The University of Texas at Austin.

Van Engelen, N. C. and J. M. Kelly (2014). "Correcting for the influence of bulk compressibility on the design properties of elastomeric bearings." Journal of Engineering Mechanics 141(6): 04014170.

Weisman, J. and G. Warn (2012). "Stability of Elastomeric and Lead-Rubber Seismic Isolation Bearings." Journal of Structural Engineering 138(2): 215-223.

Yeoh, O. (1993). "Some forms of the strain energy function for rubber." Rubber Chemistry and technology 66(5): 754-771.

Yeoh, O., G. Pinter and H. Banks (2002). "Compression of bonded rubber blocks." Rubber chemistry and technology 75(3): 549-562.

Yerzley, F. L. (1939). "Adhesion of neoprene to metal." Industrial & Engineering Chemistry 31(8): 950-956.

Yura, A. Y. J. A. (2002). "Parameters Influencing Performance of Elastomeric Bearings at Low Temperatures." Journal of Structural Engineering 128(8): 986-994.

Yura, J., A. Kumar, A. Yakut, C. Topkaya, E. Becker and J. Collingwood (2001). NCHRP Report 449: Elastomeric Bridge Bearings: Recommended Test Methods.